INSTIGATING CHIRAL-SELECTIVE NONLINEAR OPTICAL PHENOMENA IN METAMATERIALS

A Thesis
Presented to
The Academic Faculty

By

Sean P. Rodrigues

In Partial Fulfillment
of the Requirements for the
Doctoral Degree in the
School of Electrical and Computer Engineering

Georgia Institute of Technology
August 2018

INSTIGATING CHIRAL-SELECTIVE NONLINEAR OPTICAL PHENOMENA IN METAMATERIALS

Approved by:

Dr. Wenshan Cai, Advisor
Jointly School of Electrical & Computer Engineering
School of Materials Science & Engineering
Georgia Institute of Technology

Dr. Ali Adibi
School of Electrical & Computer Engineering
Georgia Institute of Technology

Dr. Vladimir Tsukruk
School of Materials Science & Engineering
Georgia Institute of Technology

Dr. Zhuomin Zhang
School of Mechanical Engineering
Georgia Institute of Technology

Dr. Mohan Srinivasarao
School of Materials Science & Engineering
Georgia Institute of Technology

Date Approved: May 01, 2018

To my grandparents and family,

Whose endless love and support made this work possible.

ACKNOWLEDGEMENTS

I would like to thank my advisor Prof. Wenshan Cai. His advocacy and his persistence in helping me to surpass my limits is more than I imagined in an advisor and I'm undeniably thankful. I'm indebted to the dedication of my labmates, Dr. Shoufeng Lan, Dr. Yonghao Cui, Dr. Lei Kang, Mohammad Taghinejad, and Zhaocheng Liu. I cannot speak enough to your guidance, support and vast knowledge of the field. Thank you so much for being there for me. A special thanks to our collaborators including Dr. Yongmin Liu, Jiahao Yan, and Prof. Shengxiang Wang. I wish the best of luck to the new graduate students Kyu-tae Lee, Lakshmi Raju, Andrew Kim, Muliang Zhu, and Dayu Zhu. I would also like to thank my thesis committee Dr. Ali Adibi, Dr. Mohan Srinivasarao, Dr. Vladimir Tsukruk, and Dr. Zhuomin Zhang for their support.

I wouldn't be in graduate school if it wasn't for the amazing mentorship I've had from mentors at my alma mater: Dr. Lukas Novotny (now at ETH Zürich), Dr. Matthew Yates, Dr. James Farrar and Nicholas Valentino.

Thank you to the National Science Foundation (NSF) Graduate Research Fellowship for funding me under Grant No. DGE-1148903. Thank you to the Goizueta Foundation for supporting me via the GoSTEM Fellowship for two years and Dr. Diley Hernandez for her relentless dedication to the Hispanic and Latino communities.

Thank you to Air Force Research Labs for funding me on two separate programs, Soft Materials and Data Science, and allowing me to work at their research labs during the later summers. I want to especially thank Dr. Timothy Bunning (Chief Scientist of the Materials Research Directorate), Dr. Augustine Urbas (Optoelectronics Lead), Dr. Manuel Ferdinandus, Dr. Ben Griffin, Dr. Ekaterina Poutrina, and Dr. Dean Brown.

Thank you for funding support from the Intel Foundation, the Materials Research Society, Sigma Xi, American Physical Society: Forum on Graduate Student Affairs (FGSA), IEEE Photonics.

I want to also thank SPIE Cycle Outreach Grant, for allowing me to put on my workshop titled a "Day of Light." The event was hosted in conjunction with the Hispanic and Latino College Fair 2015 and the Atlanta Day of Science (thanks to Diley Hernandez) allowing for the workshop to impact a much larger number of students than I could have reached on my own. A summary of the event can be found here: https://cos.gatech.edu/hg/item/591331

Thank you to Dr. Felicia Benton-Johnson, and Ms. Jackie Cox from CEED for making my years at GaTech so much more bearable, providing a happy and healthy environment in all the arduous days that I experienced as a graduate student.

With the outmost gratitude and love for my mother, who I thank for insisting that I pursue my dreams no matter the cost. I want to thank my family, Rianna, Justin, and Joe: I may not have been physically present while I've been pursuing my degrees, but I'm indebted for your kindness and understanding.

Finally, I want to thank all my friends for their support throughout the years. Just writing this sentence is bringing a slew of memories rushing into my

brain and with it, an enormous amount of emotion and gratitude. I feel a great deal for all of you; thank you and if I haven't it mentioned it lately, bop me.

TABLE OF CONTENTS

LIST OF FIGURES

Page

LIST OF SYMBOLS AND ABBREVIATIONS

CD	Circular Dichroism
OR	Optical Rotation
SHG	Second Harmonic Generation
SHG-CD	Second Harmonic Generation – Circular Dichroism
TPL	Two Photon Luminescence
TPL-CD	Two Photon Luminescence – Circular Dichroism
NIR	Near Infrared

SUMMARY

As naturally occurring chiral materials demonstrate limited circularly dichroic contrast, enhancement of these polarization dependent signals has been the focus of chiral metamaterial research. By manipulating the geometric chirality of resonant plasmonic nanostructures and utilizing the state of the art in metamaterial design, we are capable of creating sophisticated chiral structures with enormous optical activity and chiral-selective light confining ability. Here, a set of chiral nanoarcs demonstrates a transmission contrast of 0.5 between left and right circular polarizations and a 20× contrast between second harmonic responses from the two incident polarizations; nonlinear and linear imaging is provided. In a later set of experiments, these chiral nanoarcs are opened up to place emitters in the most light-confining and chirally sensitive regions of the meta-structure. Tested with an ultra-fast laser, the resulting two-photon emission profiles under circularly polarized excitation display mirrored symmetry for the two enantiomeric, nanoarcs. The profile of the nonlinear signal correlates to the chiral resonance in the linear regime. The nonlinear emission signal is enhanced by 40× that of the emitters not embedded in the metamaterial and displays a 3× contrast for the opposite circular

polarization. These results expose new methods for the enhancement of chiral signal contrast and extraction.

Chiral metamaterials, in particular, offer immediate distinction between left and right circular polarizations, prompting an ideal starting place for active switching efforts – a central thrust of active metamaterial research. By exposing a chiral metamaterial to a change in 15 mW of power beyond the structure's linear optical regime, the two absorptive resonances belonging to the chiral meta-structure are spectrally shifted by 10 nm. These results demonstrate the strongest nonlinear optical rotation to date, a value 10^6 stronger than the most recent studies. The research presented herein, leverages the higher order components of the electric susceptibility tensor to yield large optically active responses and nonlinear phenomena. The last project of this thesis designs a chiral metamaterial mirror, which has the unique property of maintaining the spin state of a circularly polarized wave upon reflection from its surface. Chiral meta-mirrors, exhibiting large chiroptical responses and spin-selective near field enhancement, promise applications in polarization sensitive electro-optical information processing and biosensing.

.

Foreword

Optics has undergone many progressions. In their earliest forms lenses were utilized by the ancient Egyptians as decorative ornaments, magnifying glasses and for telescopy, to zoom into the distance to see their enemies at war and the stars beyond the clouds. In time optics took on more sophisticated shapes in order to zoom into our proximity to see microorganisms, cells, smaller. Optics in all these cases is a tool for detection, when we turn on a light, a source, it is ignited that illuminates a space through which we can detect that light. In its most basic sense light is a tool through which we gain information via illumination and detection. Eventually, light became a tool for information processing. In this transition, we learned to manufacture photonic crystals – a method to manipulate light with structures that have dimensions on the same order of magnitude of the wavelength of the light. In order, to bend light even further into directions not predicted by classical optics, light had to be manipulated with unit cells not so small that they were individually undetectable to a single wavelength, like an atom, but not so large that they would be limited by classical geometric optics. The space in-between

is left to a field called metamaterials, a class of material that hybridizes metal and dielectric components in an architectural manner to manipulate the propagation of light in methods beyond what was perceived in the realm of classical optics. The recent birth of optical metamaterials has paved the way for technologies such as negative refraction, ultrafast optical data processing and even the possibility of invisibility. The exotic features of these materials have enticed researchers to steer their focus into the domain of metamaterials. An all-encompassing resource on metamaterials was published by Dr. Wenshan Cai & Dr. Vladimir Shalaev and is capable of bringing scientists up to par with the field.[1]

A few years back a perspective piece was released by another one of the prominent researchers in the field, Dr. Nikolay Zheludev.[2] The article provided a broad genre of research topics that had been and needed to be studied within the field of metamaterials. The article was a great guide for young metamaterial scientists, but as Dr. Zheludev described was only a small subset of the vast research left to accomplish within the field. While Dr. Zheludev's guide remains an outstanding resource to return to when trying to piece the future of the field together, the outline still remains only a poster board for the hot topics of the field. However, the true potential that lies within metamaterial structures can only be extracted upon the integration of many of these fields.

Just as metamaterials intertwine two types of fundamentally different materials, the future of research relies on the entanglement of unexpected fields. In this thesis, theoretical and experimental results are presented on the intersection of chiral and nonlinear metamaterials. Chirality is a property that can be structurally engineered to affect a material's electromagnetic parameters. In the context of this research, the subject of nonlinearity utilizes a fundamental high intensity beam and a material's nonlinear refractive index or portion of its susceptibility tensor. The intersection of these two fields seeks to enhance the chiral features presented by these materials and to access new properties, enhance and extract existing properties, and analyze physical properties of the material. The second chapter of this thesis utilizes the chiral parameters of a twisted arc metamaterial structure in conjunction with a high powered nonlinear laser to produce a second harmonic signal. The emitted second harmonic signal demonstrates dependence on the type of circular irradiation, with spectroscopic characteristics nearly identical to that of its linear counterpart. The nonlinear response shows magnified contrast between the two opposing circular polarizations. A great deal of the information presented in chapter two can be found in the "Nonlinear imaging and spectroscopy of chiral metamaterials" as published in *Advanced Materials*.[3] The third chapter utilities circularly dependent hotspots

within a similar metamaterial structure to demonstrate enhanced luminescent properties. The extraction of this chiral property with such an intense enhancement will be crucial to the development of hybrid active-metamaterial structures. A large portion of the information presented in chapter three can be found in the journal article "Metamaterials enable chiral-selective two-photon luminescence from quantum emitters," as published in *Advanced Materials*.[4] The information presented in chapters 3 and 4 were reproduced with permission from Wiley Publishing Group. The information presented in chapter 5 was originally published under a creative commons license with Nature Publishing Group.[5] The information presented in chapter 6 was reproduced with permission from the American Chemical Society.[6]

A great deal of my time at the Georgia Institute of Technology went beyond the lab and often into the classroom. I highly value education. I also believe that the diversification of leadership is essential to a healthy and prosperous nation that succeeds without stratification and oppression of a certain people. As such, I dedicated a great deal of my time working to locally address these challenges in the community surrounding Georgia Tech and the broader Atlanta area. This led me to work with the GoSTEM foundation at Georgia Tech, which has now become part of the broader CEISMC and CETL (Center for Teaching and Learning)

departments at Georgia Tech. I was awarded the GoSTEM fellowship to teach and run an engineering club once a week at a high school in Norcross, GA. Later I went on to teach for a 3-week program through the Center for Engineering Education and Diversity. My efforts at the school as well as my efforts on campus in a variety of domains landed me the "Outstanding service to Georgia's Community Award." I later applied to a grant to one of the international optical societies known as SPIE, to put on an optics outreach grant known as "Day of Light" workshop. A press release of the event can be found here (https://www.cos.gatech.edu/hg/item/591331).

CHAPTER I.

Chirality

Symmetry is a property which describes a state in which the transpose of an object is equal to itself. When the composition of the object and its connectedness is equivalent, but the system still lacks this symmetric quality, the material is known to be chiral. The property of chirality can be used to delineate the parity of left and right handedness, though it is not synonymous with handedness. A chiral structure can be identified by acknowledging that its mirror image can never be superposed onto itself.[7] The structures look visually similar, but they are unique and complementary to each other. The original unit structure and its non-superposable are said to be enantiomers. Another term for enantiomers is optical isomers and falls under the more general term known as stereoisomers. Just like our hands are chiral structures, organic compounds on the molecular level often exhibit the property of chirality if their structure lacks a point of inversion symmetry (a stereocenter), though this is not a necessary criterion.[8] In the realm of optics, if the structure harbors a subunit that is of a light absorbing nature, the incident light will be transmitted in an asymmetric manner. More specifically, if

the absorbing groups within the molecule or structure are arranged in a geometrically chiral manner, the far-field transmission when subjected to either circular polarization of opposite handedness will demonstrate chiroptical properties known as circular dichroism, CD, and if subjected to a linear polarization, optical rotatory dispersion, ORD.[7, 9] While CD describes the asymmetric absorption of left (LCP) and right (RCP) circularly polarized waves, ORD describes the polarization rotating ability of a material both over a range of wavelengths.

$$CD = T_{RCP} - T_{LCP}$$

ORD can be converted to CD through the Kramers-Kronig relations. The direction of rotation is known as either a dextro- or levo- rotation and identifies whether the enantiomer is dextrorotatory, thereby creating right circularly polarized light, or levorotatory, thereby creating left circularly polarized light when viewed from the detector. Because the chiral object responds differently to the two opposite circular polarizations, which is seen in the different transmission spectra, refractive indices associated with the two polarizations can be used to describe their individual responses. This was first demonstrated by Fresnel in 1825.[7] The classic, optical definition for the orientation of circular polarizations is utilized in this thesis. Here, right circular polarization is seen as clockwise as it propagates towards and is viewed from the detector. Respectively, left circular polarization is seen as rotating counterclockwise as it is viewed from the detector.

Chirality is a useful tool for identification and quantification of chemical species. The manipulation of light by a chiral structure as described above provides an identifier through which to classify that material. By measuring the amount or type of rotation experienced by the light, values of enantiomer concentration can be reached, making chirality a useful tool in industrial and biological applications to identify compounds or measure concentrations.[7] In the past, optical rotation was the go-to measurement for describing the chiral-strength of a molecule, however as technology progressed the photo-elastic modulator has consumed the modern market, allowing measurements of ellipticity and circular dichroism to become more common. There are a few reasons behind this, but a common issue is that rotational measurements of linearly polarized light can overlap, for instance if the material provides greater than a 180° rotation of polarization it is difficult to distinguish if the rotation is α or $\alpha + n \times 180$, where n is an integer. While in natural organic molecules, optical rotation which is typically measured via ellipticity provides values on the level of millidegrees [10] at the sodium D-line (λ=588, 589 nm), chiral metamaterials can provide values that exceed organic media by 100×.[11] The chirality of an organic molecule is often described by its specific optical rotatory power also known as specific rotation $[\alpha]_{\lambda}^{t^0}$ at the sodium D-line.

1.2 Measuring Chirality

CD measures the electronic transitions that absorb light differently in molecules. Circular dichroism at its base is the difference in absorption of left and right circularly polarized waves as they pass through a chiral material. In terms of molecules, the absorption, which is related to the electronic transition of electrons from one state to another, is hard to detect in a mostly transparent solutions of molecules. For the purpose of this these, the scattering and reflection of the chiral metamaterial structures will be rather small and thus the circular dichroism can be regulated to the difference in transmission of left and right circularly polarized waves through the materials. Classically, we can define the changes in circular dichroism for weak responses in terms of the Eulerian absorption. More on this can be found in the book chapter "Measurement of circular dichroism of electronic transitions."[12] First we must write intensities for circularly polarized waves passing through a medium.

$$I_L = I_0 e^{-a_L}, I_R = I_0 e^{-a_R}, I_{avg} = \frac{I_L + I_R}{2}, \Delta I_{CD} = I_R - I_L \tag{1.1}$$

Here, I_L and I_R which are the intensities of a left and right circularly polarized wave transmitted through a material. We can now define CD in terms of the Eulerian CD. CD. The definition of the Eulerian CD is then.

$$\Delta a_{CD} \equiv a_R - a_L,\ \overline{a} = \frac{a_L + a_R}{2} \tag{1.2}$$

here the formal conditions through which chiral molecules are measured will be discussed. In these cases CD is often reported in terms of ellipticity.

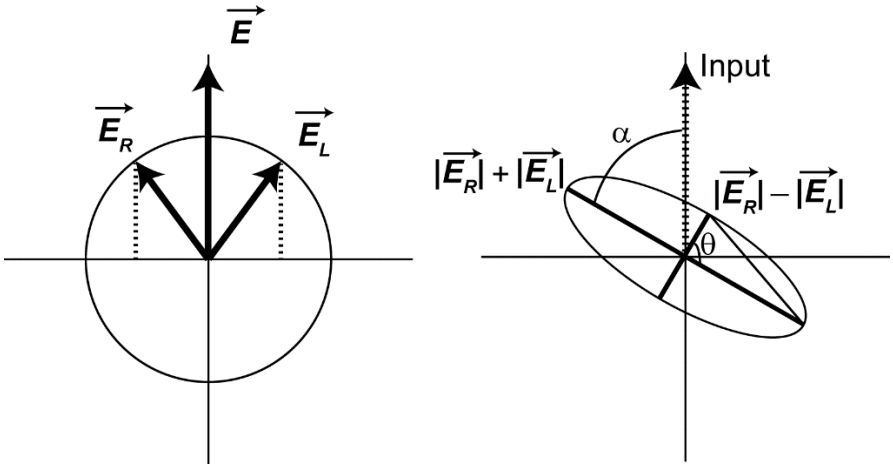

Figure 1.1: [Left] Superposition of a left and right circularly polarized wave to form a vertically polarized wave. [Right]. Depiction of an elliptically polarized electric field. α is the optical rotation dispersion, θ is the ellipticity.

Ellipticity, depicted as θ in Figure 1.1, is defined as the angle that is retrieved from the tangent of the ratio of the semi-major and semi-minor axes of the electric field of a wave. As previously noted, circular dichroism is the difference

in transmission between left and right circularly polarized waves. We can then consider a linearly polarized wave as the superposition of both a left and right circularly polarized wave. As such, the polarization of a linearly polarized wave transmitted through a chiral medium will then become partially elliptical at wavelengths where the structure is chiral, due to the differential in absorption between the two circularly polarized waves. The reduction in the magnitude of the electric field vectors is also witnessed. The orientation of the ellipse in terms of the angle from the input polarization is known as optical rotatory dispersion (ORD). The elliptical shape of the wave can be measured using a polarizer, however this is recoded in terms of intensity. The relation between the electric field and the intensity of the measured beam can be roughly approximated as $I \sim |E|^2$, but can be more directly calculated from the Poynting vector. With this in mind we can write

$$\tan\theta = \frac{\sqrt{I_R} - \sqrt{I_L}}{\sqrt{I_R} + \sqrt{I_L}}$$

$$= \frac{e^{-\frac{a_R}{2}} - e^{-\frac{a_L}{2}}}{e^{-\frac{a_R}{2}} + e^{-\frac{a_L}{2}}} = \frac{e^{\frac{\Delta a_{CD}}{4} + \frac{\bar{a}}{2}} - e^{-\frac{\Delta a_{CD}}{4} + \frac{\bar{a}}{2}}}{e^{-\frac{a_{CD}}{4} + \frac{\bar{a}}{2}} + e^{\frac{a_{CD}}{4} + \frac{\bar{a}}{2}}} = \tanh\left(\frac{\Delta a_{CD}}{4}\right) \quad (1.3)$$

Here θ can be approximated as $\tan(\theta) = \theta$ for small angles, which is typically common for chiral organic molecules.

Note Eulerian units are used here in contrast to decadic units:

$$I = I_0 10^{-A} \; vs \; I = I_0 e^{-a} \tag{1.4}$$

$$A = \log \frac{I_0}{I} \; vs \; a = \ln \frac{I_0}{I} \tag{1.5}$$

Thus to convert

$$a = A \ln 10 = A \, 2.303 \tag{1.6}$$

1.3 Chirality in Nature

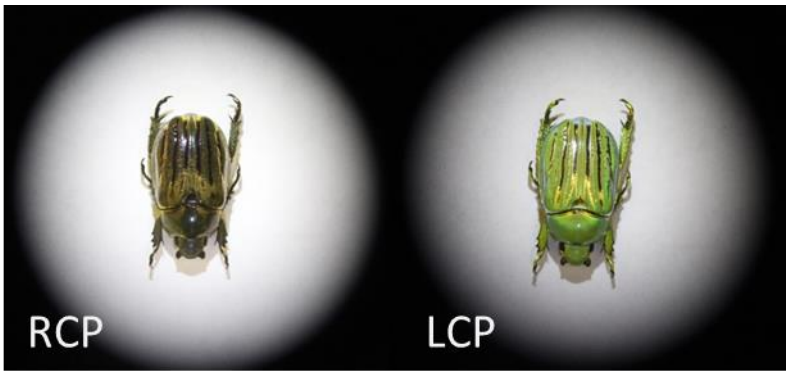

Figure 1.2: Chrysina Gloriousa On the left under an LCP analyzer and on the right under an RCP analyzer.

As previously discussed, chirality is found at the basis of organic structures and nature utilizes it to great lengths in biochemistry in order to achieve a wide variety of effects. In some cases the rotation of a single bond can lead to configurational isomerism, meaning that the chemical composition is identical, however its configuration is slightly shifted to form a different molecule. In

biochemistry this can have huge effects, for instance the rotation of a single bond can change l-glucose to d-glucose. The l-isomer can only be synthesized in a laboratory, and cannot be use an energy source for living organisms. Simple enantiomers have enough dissimilarity such that their difference propagates in the overall structure of the complex macromolecule, potentially achieving a massive net effect simply due to the handedness of the molecule. This feature of chirality on the molecular level provides optical fingerprints. When passing light through these chiral objects we are capable of identifying the difference between the two possible structures. However, in nature chiroptical properties are extremely weak. For instance, chirality manifested in the form of optical rotatory dispersion is often used to measure the concentration of a sugar solution. However to accurately quantify this type of rotation from organic molecules, either a large concentration is required in a small cuvette or if you are measuring concentration a large cuvette length of 10 cm is required.

Few organisms are thought to demonstrate circularly polarized dependence however the list is consistently growing. For example, the mantis shrimp can produce circular polarizations with its tail and detect the circular polarizations with certain segments of its compound eye. Meanwhile other organisms are currently only known to 'generate' circular polarizations such as the Chrysina

genus of beetles that reflects one circular polarization, but not the other.[13] Figure 1.2 presents this organism's unique feature. The broadband circular reflectance produced by some beetles like the Chrysina aurigans[14] is much like that of a liquid crystal, with the planes of the crystal oriented in a helical fashion. The portion of the exoskeleton that provides the green and brown contrast when analyzed for the two opposite polarizations is said to be cholesteric in nature.[15]

However, the application of chirality in biochemical studies is not limited to the conventional, linear regime. In fact, the realm of biological characterization employs the second-order susceptibility tensor of some biotic matter such as collagen and striated tissues to investigate their structure, shape, deformation and orientation.[16-18] The chiral selectivity of a biological sample's second harmonic response is typically orders of magnitude larger than its counterpart in the linear regime; however the nonlinear response can only be activated in materials that are chiral or non-centrosymmetric. Thus, chiral materials are naturally suited for second-order nonlinear interactions because all chiral structures are intrinsically non-centrosymmetric and therefore possess non-vanishing values of the second order susceptibility $\chi^{(2)}$. For this reason, chiral second harmonic generation (SHG) has been utilized as a powerful tool for probing the structure of interfaces, organic tissues, and biochemical agents.[11, 19-22]

1.4 Chirality in Metamaterials

Despite the aforementioned applications, chiral responses from naturally occurring materials are generally very weak, thereby prompting the development of artificially structured optical media with unusually strong chirality. [9] The past few years have witnessed an explosive development of chiral optical metamaterials that exhibit circular dichroism and optical rotation orders of magnitude larger than conventional materials.[23-32] Figure 1.3 shows a series of chiral structures that have contributed to the realm of chiral metamaterials. A sufficiently strong chiral effect in metamaterials can also lead to intriguing phenomena such as negative refraction[33, 34] as well as important applications including circular polarizers,[35] beam splitters,[36] and biochemical sensors.[10] A couple good review papers can be found here for chiral metamaterials.[29, 37]

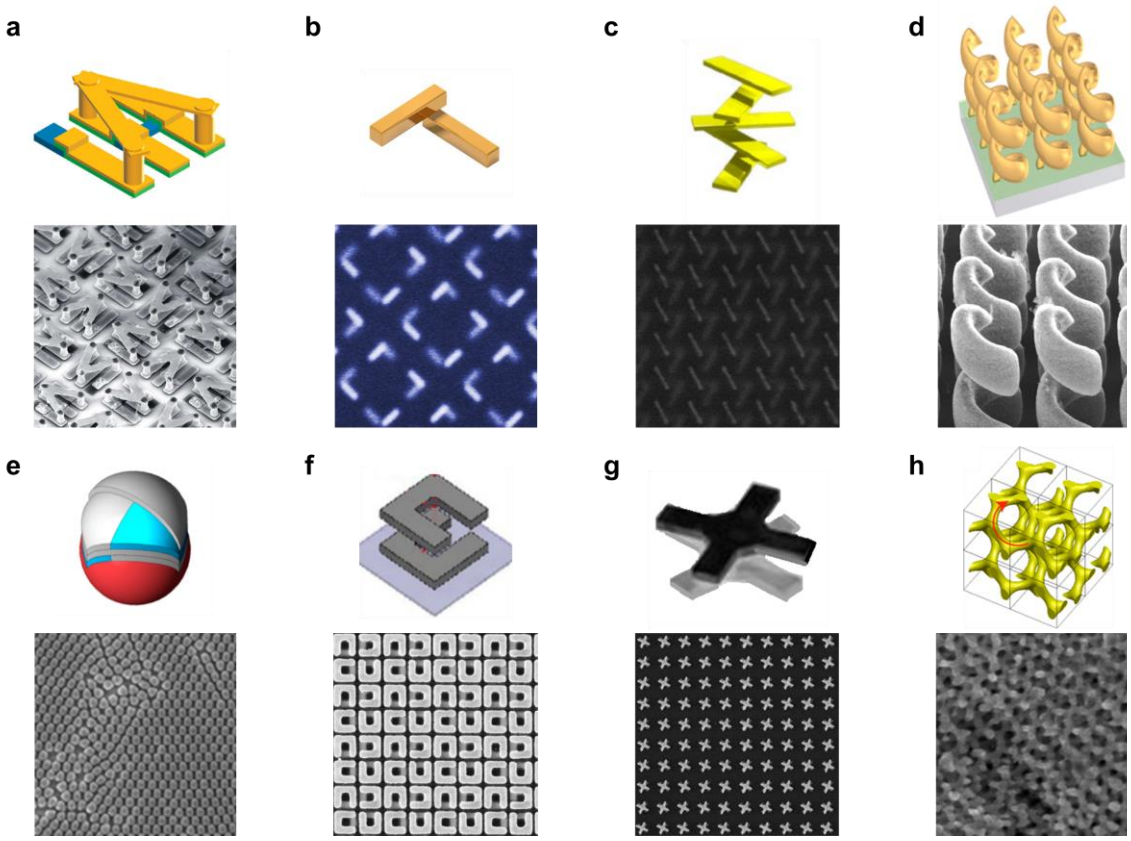

Figure 1.3: Chiral metamaterial structures from the literature. a) Structure used for chiral switching [38] b) Simple bar structure for theoretical modeling [24] c) Stacked chiral bars for a broadband effect[28] d) Helical meta-atoms for continuous modification of the circular polarization as the wave passes through the material [35] e) Self-assembled monolayers for industrial grade chiral responses[39] f) Split ring resonator used as one of the first chiral demonstrations [40] g) twisted cross was used to create heightened chiral, nonlinear responses [41] h) Self assembled coblock polymers filled with metal to create a 3D mesh[42]

It should be noted that it is the spatial distribution of the excited states of the species or structure that causes circular dichroism. As the light passes through

the structure, the unit must contain absorbing components along the direction of propagation of the incident light. At first many metamaterial papers relied on angular incidence of flat two dimensional structures in order to generate chiral responses.[43-45] These resonances were achieved by sculpting the 3D electric field by using the 2D metamaterial at an angled incidence. Over time, the field recognized that overlapping structures along the propagation direction of light was truly necessary, thus creating structures that could manipulate the light as the light passed through the structure at normal incidence.[24, 25, 28, 46] Applying light at normal incidence, also helps to remove potential artifacts in measurements such as anisotropy.[29]

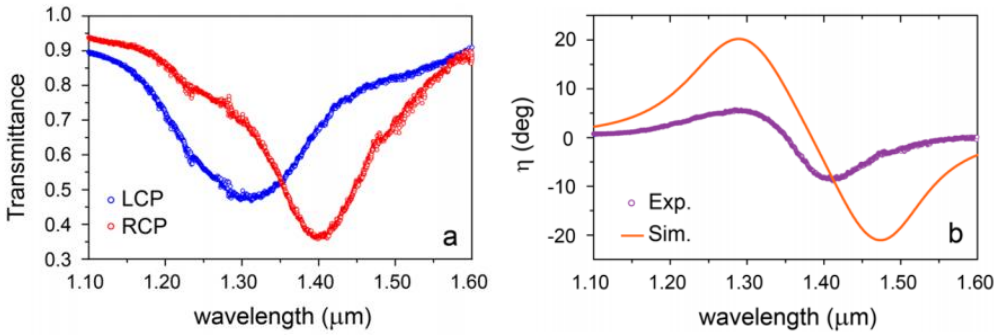

Figure 1.4: Chiral properties of a twisted nanoarc pair in the infrared. (a) Measured transmission spectra of LCP (blue) and RCP (red) light waves at normal incidence. (b) Ellipticity η of transmitted light obtained from experiments (purple) and simulations (orange). The twisted arc metamaterial structure at

longer wavelengths displays the cotton effect.[47] Reproduced with permission from Nano Letters.

Utilizing these concepts, our group designed its first chiral metamaterial. The published research describes a pair of arcs twisted in the z-direction that demonstrates large circular dichroism and optical rotation in the infrared regime.[18] Figure 1.4 provides some of the crucial findings of the papers and illustrates for us the twisted arc structure. The 3D structure of the chiral metal arcs are capable of producing a chiral response at normal incidence. The chiral nature of the structure is demonstrated by the cotton effect, which describes the coincidence of optical rotatory dispersion and the circular dichroism at the same spectral location.[7] This effect is witnessed in Figure 1.4 where the elliptical maximum, circular dichroism maximum and the optical rotatory dispersion inflection point occur at roughly the same wavelength of 1.35μm. The results from this twisted arc structure become a crucial starting point for my own research, which is presented in Chapter 2.

Chirality has opportunities to pour its properties into a wide range of optical methodologies, techniques and applications. The next subsection will discuss the origin of chirality in metamaterials. The following subsections will describe how chiral metamaterials are being used to achieve unexpected optical phenomena, or

achieve optical traits of structures using chiral materials. The future of chirality in artificial structures will require the manipulation of the chiral signals, whether it's with reconfigurable materials, voltage biasing, or optical pump-probe techniques.

1.4.1 Origin of Chirality in Metamaterials

With regards to chemical species, the origin of the circular dichroic behavior can be traced back to a section of the chiral molecule known as a chromophore, which absorbs the impinging light. The chromophore or chromophores within the molecule absorb the light and stabilize the excited state along the rest of the structure. This same property can also explain how chiral metamaterials achieve their circular dichroic properties. In this case, however, the absorption of light is typically due to a resonance feature within the material. The theoretical understanding behind the absorptive resonance of these metamaterial structures can be described by the Born-Kuhn model. This model, as an offshoot to the Drude-Lorentz model, utilizes two charged particles that are coupled to each other. Depending on the resonance of the coupled particles, one can imagine how a linearly polarized beam passing through these charged particles, might rotate the incident wave.[24, 48] As described by Rogacheva and Yin, the coupling of the particles leads to two excited states, one called the bonding and the other the antibonding

state, each with their own distinct energy levels. The excited state corresponds to the increased absorption witnessed during a circular dichroism measurement.

1.4.2 Negative Refraction

What first brought chiral structures their spotlight in the metamaterial research field was their ability to create negative refraction. Achieving a negative refractive index implies that both the electric permittivity and the magnetic permeability of a given material must both be negative. This was one of the first goals of metamaterials, as negative refractive materials are not found in nature. Although 2D split ring resonators were the primary structure to enable and demonstrate this property[49], it was later realized that chiral structures could provide an alternative route to generating negative refraction. To date, this subset of chiral metamaterials has been prolifically researched and chiral metamaterials with negative refraction have been demonstrated in the optical[50], terahertz[34] and microwave regimes[48, 51].

1.4.3 Giant Chiral Signals

It was quickly realized that the effects of chiral metamaterials could be significantly enhanced and used to create giant chiral properties. The two

quantities measured that distinguish the highly chiral effects of metamaterials are circular dichroism and optical rotation. The progression from planar structures with large unit cells to bilayered structures with slight twists in the two layers to using fully isotropic materials has made an enormous increase in the effect of the signals. To achieve high circular dichroic responses it is essential to manipulate the unit cell structure in the direction relative to the propagation of incident light. This k-direction manipulation provides the light absorbing necessary as the circularly polarized wave passes through the material. Knowing the pitch of the impinging wave, the spacing between bi-layered or multi-layered structures and the angle of twist induced in each plane of the structure is absolutely essential to creating the ideal chiral metamaterial. If a chiral metamaterial structure is not 3D, it is highly likely that the chiroptical signal will experience significant phase anisotropy. One method to measure such anisotropy is discussed here,[52] but can also be calculated through the ellipticity of the structure as described here.[47]

Fabrication of such chiral structures can be achieved in a multitude of ways, many of these methods can be seen in Figure 1.3. For instance, Figure 1.3h uses polymer scaffolding to create 3D metamaterial structures. In addition, Figure 1.3d utilized laser ablation to create helical metamaterials in the infrared. In an attempt to produce these large chiral effects on an industrial level one group has used self-

assembled micron-sized spheres in conjunction with glanced angle deposition to create a 3D chiral effect, as seen in Figure 1.3e. Chiral photonic metamaterials, nanoscale-engineered metal-dielectric materials, provide distinctions of optical chiral responses that surpass naturally occurring materials by many orders of magnitude.[23, 25, 28, 29, 31, 35, 41, 47, 53-56] Their applications offer potential for enhanced enantioselectivity in the biological[10], industrial[57] and photonic industries.[33, 58]

1.4.4 Extreme Signal Properties

Chiral metamaterials have been utilized to achieve several other properties that are limited to that of meta-structured materials. For instance, metamaterials are capable of obtaining strong resonances. When the materials are engineered in a certain fashion, they can create perfect absorption over a certain wavelength range.[59] This perfect absorption technique shows strong promise for future radar technologies.

Chiral mirrors are an interesting topic that has surfaced earlier this year (2015). To understand chiral mirrors first we must understand how a normal mirror interacts with circularly polarized light. For instance, when light is incident on the surface of a silver mirror, which is highly reflective for both TE & TM polarization in the visible regime, the electromagnetic waves simply inverts its propagation direction, thereby inverting LCP light to RCP light. This can be further

understood by looking at Jones calculus for a normally incident circular polarized wave on a perfect mirror. With the use of chiral metamaterials however, LCP light incident on the chiral surface can be maintained as LCP light as it is reflected at normal incidence. Other potential features of chiral mirrors include perfect absorption. For instance, these structures could near perfectly reflect one of the two circular polarizations while absorbing the other. Similar features can be achieved in cholesteric liquid crystals[60] or with oriented thin polymer films. A typical property of chiral mirrors is to either absorb at a specific wavelength for one circular polarization while reflecting a broadband spectrum for the other. However, it has been show that it is possible to reflect one spectrum over a broadband spectrum while absorbing the other.

The last extreme property to be mentioned here is that of super chiral fields in chiral plasmonic structures. The helical pitch of the circularly polarized illumination can be compressed such that its pitch matches that of a material's twist, thusly creating a superchiral field.[61]

1.4.5 Chirality for Biosensing

Perhaps the holy grail of chiral metamaterials at one point was to achieve the ability to place a chiral molecule in the presence of a metamaterial structure and enhance the field to such a degree that any molecule could be detected with its own chiral footprint. While one paper has shown progress towards this goal [10], the ability to sense chiral signals with chiral metamaterials appears to be a feat

still left to accomplish. A great deal of research regarding single atom sensing was immediately published at the surge of nano-plasmonic materials in the early 2000's, however the majority of these works don't focus on enhancing chiral signals[62-64] and the one's that do, struggle with extracting the pertinent chiral sensitive information. In addition, chiral nanoparticles on the level of <5nm also show chiral features themselves as they cannot obtain their full bulk properties, thus complicating the distinction between the two.[29]

1.4.6 Nonlinear Optical Activity

In a similar vein to switchable chirality, nonlinear optical activity is a process by which nonlinear dampening in the sample either through thermal or electrical sources, causes the chiral distinction provided by the material to fade. To achieve this degradation of the chiral response, a high intensity beam is incident on the sample. The appearance of this effect was first observed in 1965, in a piece of uranium doped glass, which then lead to a series of very meticulous research papers. The most recent contribution to the field was released within the past 4 years, but nearly 20 since any previous research. The most recent task utilized a 2D metamaterial at angled incidence to generate decreased absorption at higher pump intensities, utilizing a single shot experiment as to not mix their thermal and electrical responses.[65]

1.4.7 Filing the Gap

In order to push the ability of chiral metamaterials further, this thesis investigates how chiral metamaterials will react under nonlinear excitation conditions. An initial focus on enhancing signals from chiral media was determined. By first modifying the design provided by Cui et.al in the infrared regime a chiral metamaterial in the visible regime was created. The material composed of two bilayered, nano-arcs showed outstanding visible responses.

To further the contrast between the chiral responses, nonlinear enhancement of the signals was targeted. As mentioned earlier, a small set of research has been demonstrated on nonlinear signal generation or wave mixing in chiral metamaterials. Of the existing sources, many showed extreme hot spots or low nonlinear circular dichroic results. For this reason, experimental research was provided by utilizing the same nanoarcs mentioned to enhance the linear response in the visible regime.

A second initiative was to find a way to extract this enhanced nonlinear effect. As will be seen, simulations of the chiral arc in the linear regime demonstrate hot spots within the dielectric material surrounding the silver nano-arcs. As these hot spots appear at resonantly circular dichroic locations, there exists potential to

extract this enhanced contrast. The initiative of this work was to utilize quantum emitters, or quantum dots, to absorb this intensified signal and extract it through an emission signal. This method goes beyond the typical reflection, transmission, absorption measurements used in chiral metamaterial research. The extracted results showed outstanding enhancement of the linear regimes chiral contrast.

CHAPTER II.

Pertinent Nonlinear Optics

The intent of this chapter is to start a discussion surveying a collective knowledge across fields on the nonlinear optical responses induced by chiral asymmetry. Through this we can investigate not only how to build artificial media with stronger nonlinear optical responses, but to better utilize the properties of naturally occurring media to our advantages. This chapter while it remains in infant stage, a future article will be released that looks to expand upon these topics. Here, the sections of this chapter will be segregated by nonlinear response, rather than the rational division by material. While this may cause for inherent redundancy, the goal of this chapter is to promote interdisciplinary study.

To further explore this territory, a brief but generalized explanation of the equation of higher order waves will be given, but first we must start with the linear optical constants. The induced polarization of a beam incident on a material can be attributed to the linear susceptibility

$$\boldsymbol{P} = \epsilon_0 \boldsymbol{\chi}^{(1)} \cdot \boldsymbol{E}. \tag{2.1}$$

The macroscopic polarization induced by light propagating through a medium is written as (1). Here ϵ_0 is the permittivity of free space, $\boldsymbol{\chi}$ is the electric susceptibility tensor, and E is the electric field in tensor form. We note that (2.1) holds for the propagation of light in a linear manner, where the macroscopic polarization is proportional to the electric field. Where $\boldsymbol{\chi_1}$ is a tensor of rank 2 containing 9 elements, all of which depend on the properties of the material. The direction of the incident electric field then interacts or activates dipoles within in the medium that can be then described by the susceptibility tensor. In terms of an isotropic medium, the direction of the incident wave is unimportant, as all incident directions will have the same response; thusly (2.1) can be substantially simplified. In the case of anisotropic medium, like a crystal or much like many (but not all) metamaterial structures, the direction of orientation of the wave and the medium is critical. Some basic tensors are:

$$\boldsymbol{\chi}^{(1)} = \begin{bmatrix} \chi_{xx}(\omega) & \chi_{yx}(\omega) & \chi_{zx}(\omega) \\ \chi_{xy}(\omega) & \chi_{yy}(\omega) & \chi_{zy}(\omega) \\ \chi_{xz}(\omega) & \chi_{yz}(\omega) & \chi_{zz}(\omega) \end{bmatrix} \tag{2.2}$$

Optical Symmetry	Crystallographic System	Dielectric Tensor	
		Optical System	Crystallographic system
Isotropic	Cubic	$\begin{bmatrix} \chi_{xx}(\omega) & 0 & 0 \\ 0 & \chi_{xx}(\omega) & 0 \\ 0 & 0 & \chi_{xx}(\omega) \end{bmatrix}$	$\begin{bmatrix} \chi_{xx}(\omega) & 0 & 0 \\ 0 & \chi_{xx}(\omega) & 0 \\ 0 & 0 & \chi_{xx}(\omega) \end{bmatrix}$
Uniaxial	Hexagonal Tetragonal Trigonal	$\begin{bmatrix} \chi_{xx}(\omega) & 0 & 0 \\ 0 & \chi_{xx}(\omega) & 0 \\ 0 & 0 & \chi_{zz}(\omega) \end{bmatrix}$	$\begin{bmatrix} \chi_{xx}(\omega) & 0 & 0 \\ 0 & \chi_{xx}(\omega) & 0 \\ 0 & 0 & \chi_{zz}(\omega) \end{bmatrix}$
Biaxial	Orthorhombic	$\begin{bmatrix} \chi_{xx}(\omega) & 0 & 0 \\ 0 & \chi_{yy}(\omega) & 0 \\ 0 & 0 & \chi_{zz}(\omega) \end{bmatrix}$	$\begin{bmatrix} \chi_{xx}(\omega) & 0 & 0 \\ 0 & \chi_{yy}(\omega) & 0 \\ 0 & 0 & \chi_{zz}(\omega) \end{bmatrix}$
	Monoclinic		$\begin{bmatrix} \chi_{xx}(\omega) & \chi_{yx}(\omega) & 0 \\ \chi_{xy}(\omega) & \chi_{yy}(\omega) & 0 \\ 0 & 0 & \chi_{zz}(\omega) \end{bmatrix}$
	Triclinic		$\begin{bmatrix} \chi_{xx}(\omega) & \chi_{yx}(\omega) & \chi_{zx}(\omega) \\ \chi_{xy}(\omega) & \chi_{yy}(\omega) & \chi_{zy}(\omega) \\ \chi_{xz}(\omega) & \chi_{yz}(\omega) & \chi_{zz}(\omega) \end{bmatrix}$

2.1 Expansion of the Taylor Series

Conditions: In the event that the field strength supersedes ~100 KV/m, the electric susceptibility manifests into a Taylor expansion, taking on second and third order forms.

$$\boldsymbol{\chi(E)} = \boldsymbol{\chi^{(1)}} + \boldsymbol{\chi^{(2)}} \cdot \boldsymbol{E} + \boldsymbol{\chi^{(3)}} : \boldsymbol{EE} \tag{2.3}$$

Substituting the new description of the electric susceptibility, which now shows dependence on the electric field, into equation (2.1), we now have a description of the polarization for the newly generated waves. Achieving powers upwards of ~100 KV/m is more easily achievable today using femtosecond pulsed lasers. The pulsed laser system utilized in the Cai lab currently operates at an 80 GHz repetition rate, and a 100 fs pulse duration. The induced polarization of these higher order fields is characterized by the nonlinear susceptibility tensors $\chi^{(2)}$ and $\chi^{(3)}$ and is described by[66]:

$$\boldsymbol{P} = \epsilon_0(\boldsymbol{\chi}^{(1)} \cdot \boldsymbol{E} + \boldsymbol{\chi}^{(2)} : \boldsymbol{EE} + \boldsymbol{\chi}^{(3)} \vdots \boldsymbol{EEE} + \cdots) \tag{2.4}$$

If we assume all the quantities in equation (2.4) are real, we are forcing both the electric field and the induced polarization to be in phase with each other, essentially for them to be coherent. Moreover, assuming that the susceptibility is real, also causes the polarization to respond instantaneously on the electric field strength, thereby not being dependent on its past history. This assumption holds for many nonlinear processes in many materials, though every situation should be considered individually. Typical processes that respond on a sub-fs timescale include second harmonic generation (SHG), difference frequency generation (DFG), and sum frequency generation (SFG). In such a situation, where the field responds instantaneous, by definition, we must assume that the material is also

dispersionless my means of causality. Moreover, by virtue of Kleinman symmetry, the medium is often considered lossless. Unfortunately, as the results presented herein will show, these assumptions may not hold for the presented demonstrations, specifically that of the apparent dispersion of the nonlinear susceptibility. Finally, in order to produce second harmonic generation, there should generally be phase matching in crystals, which requires a significant propagation distance. As should be noted, our metamaterial structures are often no larger than 200 nm in the z-direction. In such structures, it has been predicted that the main contribution is from effects known as surface-SHG. The second order nonlinear susceptibility is a third rank tensor.[67] A general description of the second order susceptibility tensor:

$$\chi^{(2)}(\omega) = \begin{bmatrix} \chi_{xxx}(\omega) & \chi_{xyy}(\omega) & \chi_{xzz}(\omega) & \chi_{xyz}(\omega) & \chi_{xzy}(\omega) & \chi_{xzx}(\omega) & \chi_{xxz}(\omega) & \chi_{xxy}(\omega) & \chi_{xyz}(\omega) \\ \chi_{yxx}(\omega) & \chi_{yyy}(\omega) & \chi_{yzz}(\omega) & \chi_{yyz}(\omega) & \chi_{yzy}(\omega) & \chi_{yzx}(\omega) & \chi_{yxz}(\omega) & \chi_{yxy}(\omega) & \chi_{yyz}(\omega) \\ \chi_{zxx}(\omega) & \chi_{zyy}(\omega) & \chi_{zzz}(\omega) & \chi_{zyz}(\omega) & \chi_{zzy}(\omega) & \chi_{zzx}(\omega) & \chi_{zxz}(\omega) & \chi_{zxy}(\omega) & \chi_{zyz}(\omega) \end{bmatrix} \quad (2.5)$$

Since, we're specifically interested in second harmonic generation for much of the demonstrations in this thesis, a brief summary of the description of the nonlinear signal will be provided for an exemplary crystal. Similar to equation (5) we can write

$$P_i = E_0 \chi_{ij} E_j + 2d_{ijk} E_j E_k + 4\chi_{ijkl} E_j E_k E_l \quad (2.6)$$

where χ_{ij} first order or linear susceptibility, d_{ijk} is the second order nonlinear susceptibility, and χ_{ijkl} is the third order nonlinear susceptibility. Note that the two electric fields can be in different directions, j and k, or collinear. The second term in the nonlinear polarization equation will provide us with the equation for the second harmonic wave.

$$P_i = 2d_{ijk}E_jE_k \tag{2.7}$$

If we take

$$E = \frac{1}{2}\left\{E_0\, e^{i\omega t} + E_0\, e^{-i\omega t}\right\} \tag{2.8}$$

Then we can write

$$P_{0i}^{2\omega} = d_{ijk}\, E_{0j}^{\omega}\, E_{0k}^{\omega} \text{ or } P_{0i}^{\omega_1+\omega_2} = d_{ijk}\, E_{0j}^{\omega_1}\, E_{0k}^{\omega_2} \tag{2.9}$$

Where the first equation of (2.9) represents the sum of two frequencies that are identical and the second where the sum of the two frequencies are different. The first is second harmonic generation, while the second is sum frequency generation. The equation of the nonlinear frequency can then be written in tensor form. The nonlinear tensor is simplified to a 3x6 tensor, which comes from the three rectangular coordinate directions and the 6 the combinations of electric fields that are paired off.

$$\begin{bmatrix} P_{0x}^{2\omega} \\ P_{0y}^{2\omega} \\ P_{0z}^{2\omega} \end{bmatrix} = \begin{bmatrix} d_{11} & d_{12} & d_{13} & d_{14} & d_{15} & d_{16} \\ d_{21} & d_{22} & d_{23} & d_{24} & d_{25} & d_{26} \\ d_{31} & d_{32} & d_{33} & d_{34} & d_{35} & d_{36} \end{bmatrix} \begin{bmatrix} E_{0x}E_{0x} \\ E_{0y}E_{0y} \\ E_{0z}E_{0z} \\ 2E_{0y}E_{0z} \\ 2E_{0z}E_{0x} \\ 2E_{0x}E_{0y} \end{bmatrix} \tag{2.10}$$

For example, KDP, KH2DPO4, is a common nonlinear crystal with a $\bar{4}2m$ symmetry, leaving only d_{14} and d_{36}. This gives us second harmonic frequencies generated by

$$P_x^{2\omega} = 2\, d_{14} E_{0y}^{\omega}\, E_{0z}^{\omega} \text{ and } P_z^{2\omega} = 2\, d_{36} E_{0x}^{\omega}\, E_{0y}^{\omega} \tag{2.11}$$

Here the second harmonic wave is emitted in the z-direction, while the incident electric field is $E_z = 0$. To achieve efficient SHG, the angle of incidence of the incident wave relative to the crystal axes must be selected for phase matching between ω and 2ω. [Military Laser Technology for Defense, McAulay]

While three-wave mixing is the most standard method to produce a second harmonic signal, a four wave mixing process also exists. If an external field is applied to a crystal the $\chi^{(3)}$ can be used to generate electric field induced second harmonic generation (EFISH). I refer the reader to the Conclusion chapter, where some resources are cited.

2.2 Chirality implies a lack of centrosymmetry

The nonlinear counterparts of circular dichroism and optical rotation exhibit heightened responses compared to their linear versions. The more pronounced responses are due to the nature of chiral metamaterials. That is, chirality and second order responses share a similar trait: a lack of symmetry. Spatial symmetry or a lack there of can have an impact not only on linear electromagnetic effects, but also on their nonlinear counterparts. Centrosymmetry is a term that describes a point group. For instance, chiral point groups 1, 2, 3, 4, 6, 222, 422, 622, 32, 23, 432 are also noncentrosymmetric point groups. A centrosymmetric material is one that holds a center of symmetry, this center of symmetry nullifies the second order susceptibility terms.[67] Therefore when a material is noncentrosymmetric, it can give rise to second order optical nonlinearities, if the required phase matching and pump energies are met. However, chirality and handedness should not be confused. Specifically, chirality refers a dissymmetry within a structure of which the structure cannot be superposed onto its mirror image. There are structures, both 2D and 3D that can demonstrate optical activity, yet retain a sense of mirror symmetry.[68] These structures are handed, but not chiral. Such structures are typically centrosymmetric and cannot easily achieve the nonlinear responses observed later in this thesis.

Axial chirality in molecules is much like the development of chirality in metamaterial structures. In this case, the molecule does not possess a stereocenter, but instead an axis of chirality. Here the molecules, much like the metamaterial structures retain an axis about which a set of substituents is held in a spatial arrangement that is not superposable on its mirror image.

Within the second-order electric susceptibility tensor there is a possibility for chiral materials to have a term $\chi_{xyz} = -\chi_{yxz}$. This term is in part responsible for the intensified chiral responses seen in second harmonic generation-circular dichroism (SHG-CD).

However, the nonlinear behavior of chiral metamaterials with intensity-sensitive optical properties or wave mixing characteristics has, thus far, received rather scant attention. Of the previous nonlinear, chiral studies, the topics have focused on single meta-atom imaging and refinement of minor structural deformations that contribute to extreme hot spots.[46, 53, 69, 70] In addition, these studies apply SHG imaging to further understand metamaterial resonances and field enhancements in the chiral structures. The limited but essential research in this field demonstrates that nonlinear, chiral metamaterials offer significant potential for three major reasons. First, just as SHG requires the disruption of symmetry in order to produce a non-centrosymmetric $\chi^{(2)}$ electromagnetic tensor,

a unit cell must not have a point of inversion symmetry in order to produce chirality. By disrupting the typical symmetry for the susceptibility tensor, the harmonic response is forced to rely on the handedness of the structure, thereby allowing for disambiguation of the two enantiomers in the nonlinear regime. Secondly, metamaterials consisting of metallic particles of subwavelength dimensions have pronounced optical resonances which magnify their SHG response. These optical responses spawn from the properties of the metallic nanoparticles, including localized surface plasmon resonances, lightning rod effects, and their high surface to volume ratio. A third reason to explore nonlinear responses for chiral metamaterials is that metals offer the perfect platform by which to induce surface-second harmonic generation. This type of SHG is most strongly witnessed at interfaces where the symmetry of a material's electromagnetic tensor $\chi^{(2)}$ is disrupted due to the juxtaposition of another material at that interface. For these reasons, nonlinear responses in chiral metamaterials show enhanced contrast between oppositely circularly polarized waves. The study of nonlinear phenomena in chiral metamaterials is also in-line with the emerging field of nonlinear metamaterials, which promises exciting opportunities to create customized nonlinear media with artificial, molecular arrangements and tailored geometries.[71-74]

The addition of these advanced techniques has provided enhanced enantiomer selective microscopy and strengthened the identification of optically active structures, however the overall chiral distinctive properties of naturally occurring materials remain weak and are mostly limited to the ultraviolet spectrum. In this way, the realm of metamaterials provides the opportunity to build upon the existing platform of chiral handedness that nature has offered.

2.3 Chiral, molecular, nonlinear optics

Just as in crystals and metamaterials, the elicited dipoles in a material that is irradiated from a strong laser source will no longer behave linearly if pump powers exceed certain electronic behaviors in the material. In the case of a molecule, nonlinear optics occurs when the optical field strength becomes comparable to the field that binds the valence electrons to the nucleus of a molecule. For a general description of where molecular optical activity arises, see Fischer and Hache (2005).[22, 75-77] Briefly, the macroscopic optical activity is defined by the linear optical susceptibility, which is obtained from a combination of the electric dipole, magnetic dipole, and electric-quadrupole moments.

The assumption for chiral second order processes is that the frequency conversion processes are coherent. As discussed earlier in this chapter, this

assumption allows us to simplify the nonlinear optical polarization to rely primarily on the instantaneous electric field. For the case of second-order nonlinear signal generation, we must only consider the quadratic term $\chi^{(2)}\boldsymbol{EE}$, while the first and third order terms can be eliminated as shown previously. Chiral sum-frequency generation is the only second order nonlinear optical process that can occur in a bulk liquid. In contrast, both second harmonic generation and sum-frequency generation can occur at a surface or interface. The reason behind this is that a bulk liquid of chiral molecules has a random, or isotropic, distribution of molecules throughout. This isotropic distribution destroys the macroscopic opportunity to produce second harmonic generation in such a medium. However, chiral monolayers have provided values of SHG-CD that reach 0.7.[21] SHG-CD is defined as Second Harmonic Generation Circular Dichroism and will be discussed at greater lengths in Chapter 3. This value is defined as $SHG - CD = \frac{I_{RCP}^{2\omega} - I_{LCP}^{2\omega}}{(I_{RCP}^{2\omega} + I_{LCP}^{2\omega})}$.

2.4 Chiral Sum-Frequency Generation

In a simplistic view, sum-frequency generation is achievable due to the added asymmetry of the incident fields, in comparison to that of waves at the same frequency. As described previously, in order to resolve chirality, we must provide

a chiral medium to do so. We can then describe the polarization for a sum-frequency generated signal as

$$\boldsymbol{P}(\omega_1 + \omega_2) = \epsilon_0 \chi^{(2)}(\omega_1 + \omega_2)\boldsymbol{E}(\omega_1)\boldsymbol{E}(\omega_2) \tag{2.12}$$

Given that the system at hand is a liquid with molecules isotropically distributed, the average of this equation yields

$$\boldsymbol{P}(\omega_1 + \omega_2) = \epsilon_0 \chi^{(2)}(\omega_1 + \omega_2)\big(\boldsymbol{E}(\omega_1) \times \boldsymbol{E}(\omega_2)\big) \tag{2.13}$$

Such that susceptibility of the chiral solution is given by

$$\chi^{(2)} = \frac{1}{\epsilon_0}\frac{N}{6}\left(\chi^{(2)}_{xyz} - \chi^{(2)}_{xzy} + \chi^{(2)}_{yzx} - \chi^{(2)}_{yxz} + \chi^{(2)}_{zxy} - \chi^{(2)}_{zyx}\right) = \frac{N}{\epsilon_0}\bar{\beta} \tag{2.14}$$

Here $\bar{\beta}$ is the average of the rotationally invariant and nonvanishing tensor components.[22, 78] In such an isotropic medium, the second order susceptibility $\chi^{(2)}$ exists as a bulk physical property tensor, which is independent of the frame of reference. In this case, the tensor components that are rotationally invariant and non-vanishing are:

$$\chi^{(2)}_{xyz} = -\chi^{(2)}_{xzy} = \chi^{(2)}_{yzx} = -\chi^{(2)}_{yxz} = \chi^{(2)}_{zxy} = -\chi^{(2)}_{zyx} \equiv \chi^{(2)}_{chiral} \tag{2.15}$$

The value $\bar{\beta}$ is only nonzero for a chiral molecule and is of opposite sign for its enantiomer molecule. A pseudoscalar is a scalar that changes sign under parity. Here $\bar{\beta}$, along with other chiral observables such as G', g_0 and g_2 are all pseudoscalars. In comparison, to linear and nonlinear optical activity and as will be explored later, the second order averaged susceptibility, $\bar{\beta}$, is dependent on the

electric-dipole approximation as assumed earlier under the assumption of coherence. For molecular species, the assumption is that there is no magnetic or electric-quadrupolar contributions.

The nonlinear susceptibility $\chi^{(2)}_{chiral}$ is resonalty enhanced if any one of the three frequencies of the ω_1, ω_2 and ω_s is resonant with a molecular transition, thus generating a chiral spectrum.

For single resonances $\chi^{(2)}_{chiral}$ can be written as

$$\chi^{(2)}_{chiral} = \sum_n \frac{A_n}{\omega - \omega_n + i\Gamma_n} + \chi^{(2)}_{chiral,NR} \tag{2.16}$$

$A_n, \omega_n,$ and Γ_n represent amplitude, resonant frequency and damping constant at the nth transition, where $\chi^{(2)}_{chiral,NR}$ describes the nonresonant contribution. Chiral electronic and Chiral Vibration spectra can be obtained for chiral liquids with Sum frequency spectroscopic measurements.[79]

An isotropic collection of left or right handed molecules does not possess a center of inversion symmetry (noncentrosymmetric). For this reason, chiral media possess a second order nonlinear optical response.

Let's compare equation of nonlinear responses with that of chiral responses. Given a beam with electric field strength represented as:

$$\tilde{E}(t) = E\, e^{i\omega t} + c.c. \tag{2.17}$$

X2 being nonzero, A second harmonic response is written

$$\tilde{P}^2(t) = \epsilon_0 \chi^{(2)} \tilde{E}^2(t) = 2\epsilon_0 \chi^{(2)} E E^* + (\epsilon_0 \chi^{(2)} E^2 e^{-i\omega t} + c.c.) \quad (2.18)$$

We can't generate a second harmonic response, because it's isotropic. But we can create a SFG or DFG. So we get the following equation.

$$P_i(\omega_\sigma) = 2\epsilon_0 \sum_{jk} \chi^{(2)}_{ijk}(\omega_\sigma = \omega_1 + \omega_2) E_j \, F_k \quad (2.19)$$

Where E_j represents a field at ω_1 and F_k a field at omega2.

2.5 Intensity Dependent Refractive Index

This section looks to briefly consider the fundamental aspects of how the refractive index can be modified by input intensity. For a more complete description and phenomena that result from this interaction, such as self-focusing, optical phase conjugation, optical bistability, optical switching, pulse propagation and more see Boyd 2008, Chapters 4 and 7.[67]

In order to nonlinearly affect a wave and still maintain a frequency ω, we must realize that the equation of such a wave interacts with its nonlinear susceptibility such that $P^{NL}(\omega) = P^{NL}(\omega = \omega + \omega - \omega)$, thereby implying that the interaction is a third order effect and we can write the polarization as

$$P^{NL}(\omega) = 3\epsilon_0 \chi^{(3)}(\omega) \, |E(\omega)|^2 \, E(\omega) \quad (2.20)$$

This holds under the condition that the incident light is linearly polarized. In addition, we are concerned with the total emitted polarized wave. For the purpose

of a later chapter in this thesis, we will first look at the case for a single input beam that is inflicting self-action and modifying the outgoing wave. For the case of a pump probe experiment, see Boyd 2008, Chapter 4. [67]

For the case of self-action, we consider that the total equation of the wave is given by

$$P^{TOT}(\omega) = \epsilon_0\chi^{(1)}E(\omega) + 3\epsilon_0\chi^{(3)}|E(\omega)|^2E(\omega) \equiv \epsilon_0\chi_{eff}E(\omega) \tag{2.21}$$

Here we introduce a new term, in an effort to maintain experimental convention, but often provide an oversimplified understanding of the physics at hand. Here,

$$\chi_{eff} = \chi^{(1)} + 3\chi^{(3)}|E(\omega)|^2 \tag{2.22}$$

In order to provide experimental relevance to this study a relationship must be built between these third order effects the experienced refractive index. For this reason, a general description of the change in the refractive index in relation to the electric field must be understood. A generalization is then written such that

$$n = n_0 + 2n_2\langle E^2\rangle \tag{2.23}$$

Where, the bracket notation is standard to represent time average. We can then quickly draw that

$$n = n_0 + 2n_2|E(\omega)|^2 \tag{2.24}$$

if we take to be a linearly polarized beam $E(t) = E(\omega)e^{-i\omega t} + c.c.$ and then $\langle E(t)^2\rangle = 2E(\omega)E(\omega)^* = 2|E(\omega)|^2$. This of use to the experimentalist who can then

draw an n_2 relation to that of an effective χ_{eff}. Here we begin with the general notation that

$$n^2 = 1 + \chi_{eff} \tag{2.25}$$

By substitution, we obtain

$$[n_0 + 2n_2|E(\omega)|^2]^2 = 1 + \chi^{(1)} + 3\chi^{(3)}|E(\omega)|^2 \tag{2.26}$$

If we neglect 4^{th} order terms, which are presumed to have minimal impact experimentally, then

$$n_0^2 + 4n_0n_2|E(\omega)|^2 = 1 + \chi^{(1)} + 3\chi^{(3)}|E(\omega)|^2 \tag{2.27}$$

We can then simplify these to the often incorrectly used and overly generalized equations of the form

$$n_0 = \left(1 + \chi^{(1)}\right)^{1/2} \text{ and } n_2 = \frac{3\chi^{(3)}}{4n_0} \tag{2.28}$$

Nonlinear optical activity has been demonstrated to a wide range of materials including chiral molecules, [22], crystals with chiral point groups, and planar metamaterial structures at angled incidence.

CHAPTER III.

Nonlinear Imaging and Spectroscopy of Chiral Metamaterials

Chirality is most commonly identified with linear optical characterization techniques, however opposing circularly polarized waves can also display the same parity as a property of higher order optics. Here, a chiral metamaterial is presented that produces both distinguishable linear and nonlinear resonant features when probed with left and right circularly polarized incident beams in the visible to near-infrared regime. The material demonstrates a linear transmission contrast of 0.5 between left and right circular polarizations and a 20× contrast between second harmonic responses from the two incident polarizations. Nonlinear and linear response images probed with circularly polarized lights show strongly defined contrast.

3.1 Design & Simulation

This effort presents a number of noticeable features that favor a comprehensive study of chiral-selective nonlinear processes in metamaterials. Our sample possesses engineered structural variation along the propagation direction, which enables strong chiral responses for transmitted light at normal incidence. The size of the unit cell is substantially smaller than the wavelength of light under consideration, which allows us to treat the chiral periodic structure as a metamaterial and describe its properties using homogenized parameters. Spectral-resolved circular dichroism of both linear and harmonic signals are analyzed, compared, and utilized for imaging of a chiral pattern consisting of both enantiomers.

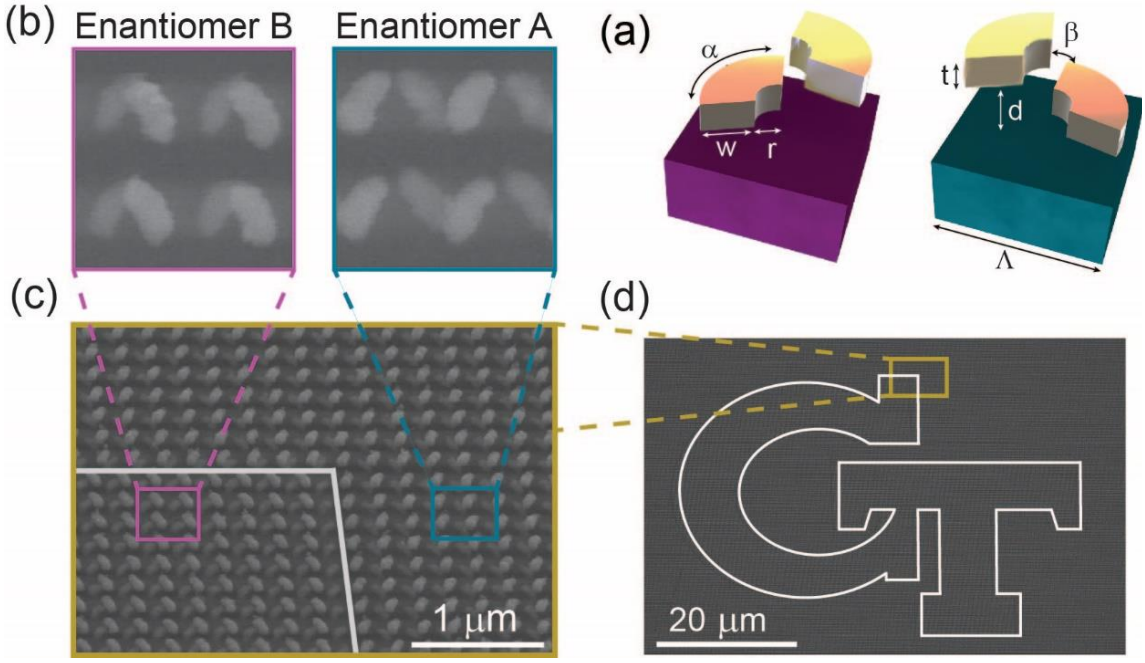

Figure 3.1: Design and simulation of the metamaterial pattern consisting of twisted arcs of both enantiomers. (a) Schematic of chiral enantiomer A (right) and B (left). Structural parameters were optimized via rigorous full-wave simulations: d=72 nm, t=42 nm, w=70 nm, r=32 nm, Λ=225 nm, α=90°, β=15°. (b) An SEM image of the enantiomers A and B, where the upper chiral arc is more visible and thus has a lighter color in the image. (c) A tilted view of a corner of the patterned 'GT' logo, where a white line is shown to distinguish where the two enantiomer structures meet. (d) An SEM image of the patterned 'GT' logo. Here, the inner region of the logo hosts the B enantiomer and the outer region hosts the A enantiomer.

The chiral metamaterial in this research is based on a twisted-arc structure, which has been employed previously to realize artificial chirality in the microwave

and infrared frequency ranges.[47, 80] Using optimized parameters along with a multilevel aligned lithography technique, we are able to downscale the previous design and obtain a giant chiral response near the red end of the visible spectrum. The metamaterial pattern, 100 × 100 μm^2 in size with roughly 10^5 arc pairs, implemented both enantiomers A and B (see Figure 3.1a) into a pattern to create the Georgia Tech "GT" logo. Figure 3.1,b-d shows the scanning electron microscope images of the sample at a series of magnifications, from the single meta-atom level to the entire pattern. Due to limitations produced by our lithography alignment system a 15 nm longitudinal shift occurred between our upper and lower chiral arc pairs, however the lateral alignment remained ideal.

3.2 Fabrication process

Fabrication: Electron beam lithography was used to create a bi-layered metamaterial with parameters specified in Figure 3.1a. To create this multi-staged material, a series of steps involving PMMA coverage, lithography, etching and silver layer deposition were applied. The full fabrication workflow can be seen in Figure 3.2.

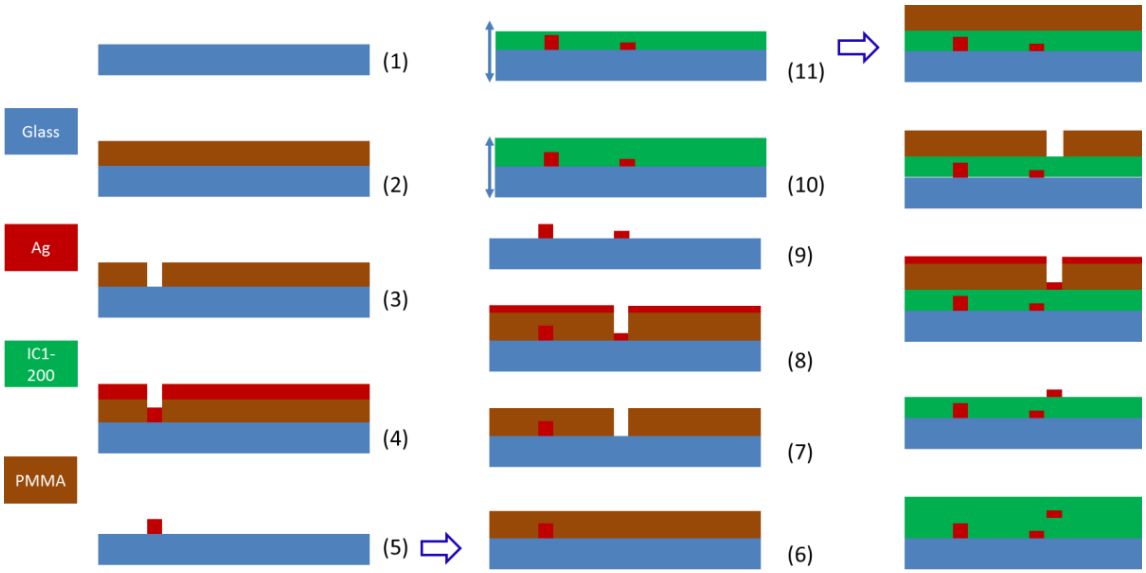

Figure 3.2. Fabrication flowchart of the twisted-arc photonic metamaterial.

The fabrication listed here is similar to that of a previous paper demonstrated in our research group, with a critical extra step of plasma etching of the first layer of spin on glass.[47] The fabrication of the twisted-arc photonic metamaterial primarily includes three runs of aligned electron beam lithography. The fabrication flowchart is illustrated in Figure 3.2, with numbers indicating the sequential steps taken. The metamaterial was fabricated on a 1×1 inch^2 clean glass substrate (1). The first run of electron beam lithography was to define the alignment marks necessary for the later steps. Electron beam resist polymethyl methacrylate (PMMA) A7 of 800 nm in thickness was spin coated at 1000 rpm with 2 seconds of ramping time for 60 seconds (2). The PMMA resist was prebaked at 180 °C for 90 seconds. After that, to eliminate the charging effect on the

dielectric substrate during the electron beam patterning, another layer of water soluble conductive polymer Espacer 300z was spin coated at 2000 rpm with 1 second ramping time for 30 seconds. Next, electron beam lithography (JEOL JBX-9300FS EBL) was carried out to define the alignment marks. After rinsing the Espacer 300z with deionized (DI) water, the PMMA resist was developed in the mixture of isopropyl alcohol (IPA) and Methyl Isobutyl Ketone (MiBK) with a volume ratio of 1:1 for 2 minutes (3). Afterwards, 10 nm thick titanium and 200 nm silver were deposited by electron-beam evaporation (4). Subsequently, a lift-off process using acetone solution was carried out to finish the patterning of alignment marks (5). The second run of the aligned electron beam lithography was carried out based on the predefined alignment marks. PMMA A4 was spin coated with 4000 rpm and 2 seconds ramping time for 60 seconds (6). After pre-baking the PMMA resist at 180 °C for 90 seconds, the Espacer 300z was coated in the same procedure as step (3). After that, aligned electron beam lithography was used to define the pattern of the bottom layer of the arc array, followed by the removal of the Espacer 300 and the development of the PMMA (7). The bottom layer of the silver arcs was then formed by electron beam evaporation of 50 nm thick silver (8) and a lift-off process (9). On the top of this silver structural layer, a transparent dielectric IC1-200 (Futurrex Inc.) was spin coated at 5000 rpm with 2 seconds

ramping time for 60 seconds (10), and then heated at 200 °C for 60 seconds to remove the solvents. Afterwards, the dielectric was then plasma etched to form a flat dielectric platform of 70 nm just above the substrate, for the subsequent patterning of the upper metallic layer. Finally, for the third run of aligned electron beam lithography, exactly the same procedures (12- 15) were repeated to form the top silver arc array of the metamaterial. After that, to reach the targeted performance and protect the sample from degradation, additional spin coating of the IC1-200 followed by baking were performed to form a transparent top cladding of 1.1 μm in thickness (16), and the fabrication of the twisted-arc chiral metamaterial was accomplished.

3.3 Linear Response

The twisted-arcs are expected to interact differently to circularly polarized lights of opposite handedness, as indicated by the simulated transmission spectra of enantiomer A in Figure 1e.

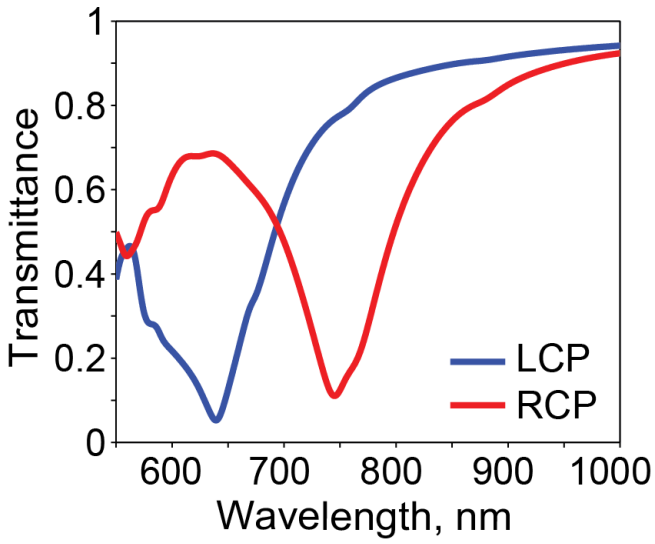

Figure 3.3: Simulated transmission spectra of enantiomer A under LCP illumination and RCP illumination with dips at 640 and 750 nm respectively.

The chiral response of a material is typically measured by the parameter of circular dichroism (CD), which is most commonly treated as the difference in extinction of left-circularly polarized (LCP) and right-circularly polarized (RCP) waves: $CD = T(\omega)_{RCP} - T(\omega)_{LCP}$. The phenomenon of absorbing different polarizations of light is conventionally due to a chiral chromophore, or light absorbing group that is found in organic substances. In contrast, our metamaterial provides its light absorbing to create its chirality by forming a resonance, between two metallic structures, that is sensitive to the angular momentum of impinging photons.

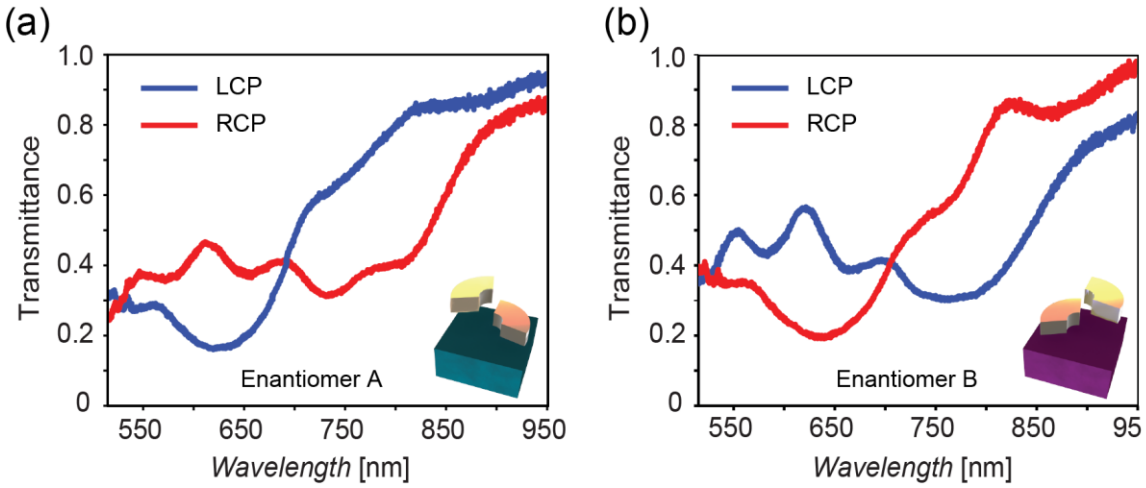

Figure 3.4: Linear spectroscopy (a) Transmission spectra of enantiomer A for circularly polarized lights. The spectral location of the resonance is sensitive to the handedness of the incident states of circular polarization. A contrast of ~ 3dB in transmission is observed around the resonance frequencies. (b) Transmission spectra of enantiomer B, which are completely complementary to those of enantiomer A.

Figure 3.4,a-b shows the transmission spectra of the two enantiomers excited with both LCP and RCP waves, which were obtained using broadband circularly polarized light at normal incidence. Defined resonance dips for enantiomer A are seen at wavelengths of 625 nm and 740 nm for LCP and RCP waves respectively. These spectra are completely complementary to those for enantiomer B with corresponding dips at similar wavelengths. These measurements correlate well with the numerical results shown in Figure 3.3, although the measured resonances

appear broader and shallower than the simulated ones due to fabrication uncertainties and size distribution in the actual sample. Around these defined resonance dips, our chiral arc pairs demonstrate strong chiral, optical activity in the visible and near-infrared regime. The difference in spectral location of resonance under circularly polarized illumination of opposite handedness can be further explained by the Born –Kuhn model.[24] In general, our meta-atomic structure undergoes an interaction that causes the two chiral arcs to resonate reciprocally at wavelengths of 625 nm and 740 nm for the two enantiomers. The circularly polarized, incident beams are intensity-reduced by the resonances of the specific enantiomer, thereby creating circular dichroism. Figure 3.5 demonstrates the circular dichroism of the enantiomer pair, which was obtained by taking the difference of the transmission curves in Figure 3.4,a-b respectively. The CD effect is maximized near resonance dips in the transmission spectra, producing a maximal magnitude of approximately 0.5. The CD curves of the two enantiomers are again complementary, thereby appearing as mirror images of each other with respect to the horizontal axis of CD = 0.

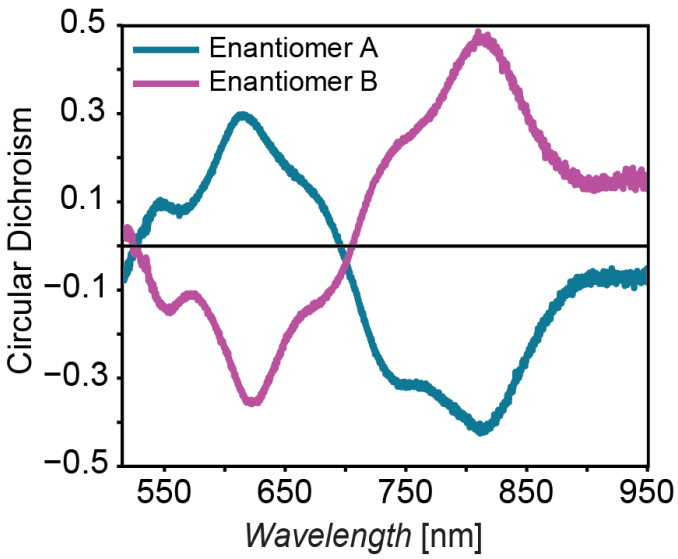

Figure 3.5: Circular dichroic response from the enantiomer pair, CD = $T_{\mathrm{RCP}} - T_{\mathrm{LCP}}$. The CD effect is maximized near resonance dips in the transmission spectra.

3.4 Linear Optical Characterization

LCP and RCP waves are produced from a broadband source followed by a series of optics that create circular polarization. The circularly polarized waves are then incident upon our sample and recorded on a silicon detector. Nonlinear spectroscopy was performed using a Mai Tai laser and a set of appropriately positioned objectives to transmit and collect the incident radiation on the sample. In order to determine the polarization of the nonlinear light emitted from the sample, a series of optics were used to determine the Stokes vectors. Detailed

information regarding the full optical characterization setup and the Stokes polarimetry analysis can be found in the supporting information of the original paper.[3]

A schematic of the linear optical characterization setup is shown in Figure 3.6 to illuminate the sample a broadband tungsten halogen source (B&W Tek BPS120, spectral range 350-2600 nm) is passed through a coupled fiber that illuminates the rest of the optical path. The light passes through a linear polarizer then a quarter wave plate to create the left and right circularly polarized light. The light is then transformed with a lens, L1 (f = 100mm), and is incident upon the sample. The objective (Mitutoyo, 20× Plan Apo NIR infinity-corrected) then magnifies the region of interest and an iris samples the location of the target sample in the transmitted image. Another lens is again used to transmit the image to the detector. A flip mirror (M1) is shown after the lens. When the mirror is engaged it can redirect the light to help us select which target sample we are looking for via the preceding lens and camera. When the mirror is disengaged the image is sent to a second linear polarizer and a set of 2 filters that cut off wavelengths at 550 and 1000nm. The linear polarizer was used to decompose the circularly polarized light into both a horizontal and vertical polarization with respect to the

grating within the spectrometer. From this data, the transmission was calculated by normalizing with respect to the transmission from the substrate.

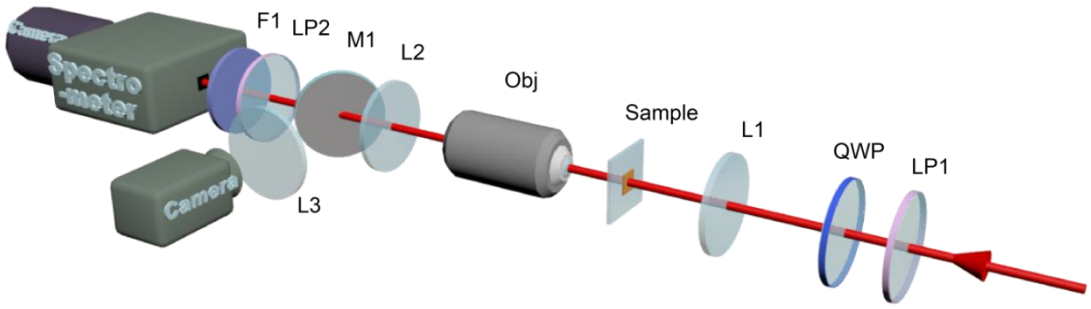

Figure 3.6: Linear transmission optical setup. Abbreviations for optical components: LP – linear polarizer; QWP – quarter waveplate; L – lens; Obj – objective lens; M – mirror; F – filter.

Next, we investigate the nonlinear spectroscopic properties of a chiral metamaterial, and exploit the resonance-enhanced and chiral-selective nonlinear signals for high-contrast second-harmonic optical imaging.

3.5 Second Harmonic Response

While our metamaterial exhibits significant first order chiral selective responsivity, its expected nonlinear optical activity from its second harmonic response will be factors of magnitude larger. For this reason, second harmonic

imaging and spectroscopy with chiroptical illumination was performed. All nonlinear measurements in this study were implemented under normal incidence, below the perceived damage threshold of the sample. We also confirmed that no detectable nonlinear signal emerged from the glass and polymer coating or unpatterned metal films under a similar excitation condition. We first carried out nonlinear spectroscopy measurements on enantiomer A with circularly polarized excitation of constant intensity, as illustrated in Figure 3.7,a-b.

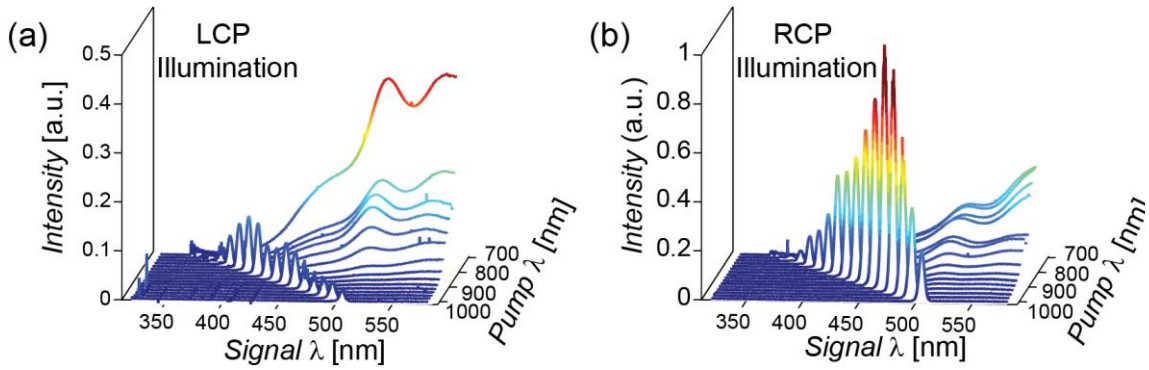

Figure 3.7: Nonlinear spectral measurements of enantiomer A. (a-b) Nonlinear signals from enantiomer A excited by (a) LCP and (b) RCP pump lights. Second harmonic peaks at half fundamental wavelength of the incident light are shown. The LCP induced second harmonic signals are roughly 15% of the maximum RCP induced second harmonic signals. Two photon luminescence tails are shown trailing off at shorter wavelengths of both LCP and RCP induced beams.

Each of the spectral curves features a frequency-doubled peak at half the excitation wavelength, situated on a broadband-background of two photon luminescence (TPL) trailing off at lower energy wavelengths. The TPL tails are minimized as we near higher excitation wavelengths because less interaction exists between impinging photons and the interband transition of silver. The level of SHG is clearly sensitive to the handedness of the circularly polarized pump light. Specifically, LCP incident light demonstrates a weaker second harmonic signal, less than 10% of the RCP induced response. In contrast, spectroscopy of enantiomer B will exhibit (not shown) a large second harmonic peak upon LCP illumination in contrast with the RCP induced signal. We also note that the spectral peak of the nonlinear responses were heavily red shifted compared to the linear resonance frequencies. The nonlinear resonance peak can be influenced by the local field enhancement and energy dissipation in the metal, but the SHG signal relies on more complicated factors including the local symmetry-breaking, the vector components of fields, and the outcoupling efficiency at the frequency of the generated wave.

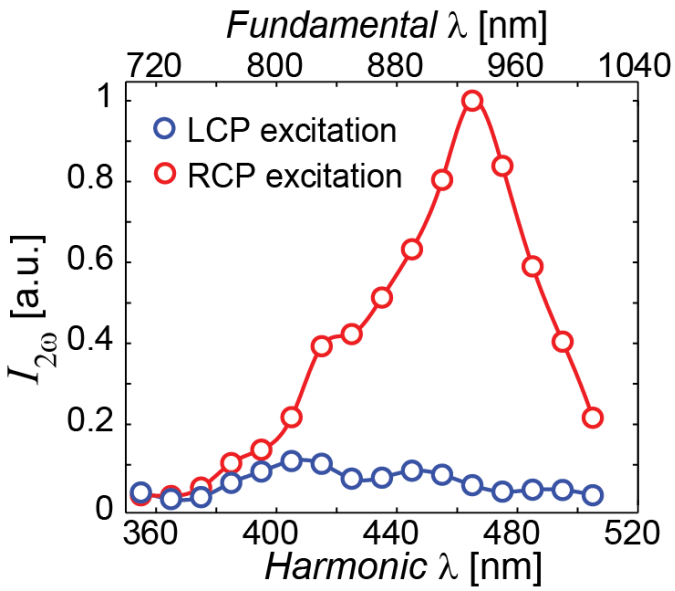

Figure 3.8: Second harmonic response from enantiomer A under circularly polarized pump lights. The peak SHG contrast occurs at $\lambda_\omega = 940$ nm, at which the conversion efficiency of SHG with RCP excitation is over 20 times higher than that of LCP excitation.

Based on the integration of photon counts for the SHG peaks in Figure 3.7 a-b, we obtain the SHG excitation spectra of both enantiomers under circularly polarized pumped beams, as shown in Figure 3.8. A contrast of ~20× in the SHG signal was observed at $\lambda_\omega \approx 930$ nm between LCP and RCP beams incident on enantiomer A. This unusually strong contrast, between the two circular polarizations, in the second harmonic spectroscopy in comparison to the linear spectroscopy makes nonlinear measurements an ideal candidate for the detection and imaging of chiral nanostructures.

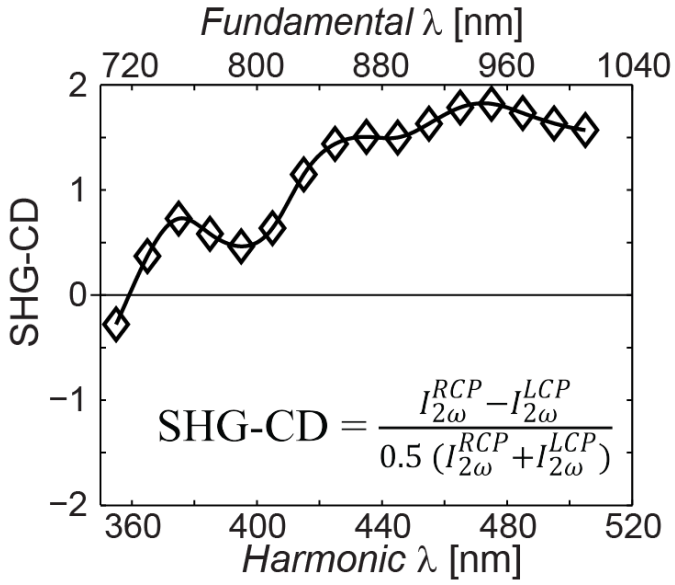

Figure 3.9: Second harmonic circular dichroism of enantiomer A. According to the definition, the maximum possible range of SHG-CD is between the values of −2 and 2.

The harmonic optical activity can be quantified using the SHG circular dichroism, defined as SHG-CD $= \frac{I_{2\omega}^{RCP} - I_{2\omega}^{LCP}}{0.5\,(I_{2\omega}^{RCP} + I_{2\omega}^{LCP})}$. From this definition, the SHG-CD is limited within the range between −2 and +2, and a magnitude of 2 represents an infinitely large contrast in the SHG conversion efficiency between the two incident circular polarizations. Based on the data found in Figure 3.8, we plot in Figure 3.9 the SHG-CD of the chiral-arc pair metamaterial, which indicated an

incredibly strong second harmonic circular dichroism of –1.85 at the wavelength of peak contrast.

Based on these measurements, we then probe the patterned 'GT' logo at a fundamental wavelength of 950 nm, at which the peak SHG-CD was obtained as seen in Figure 3.8 and 3.9.

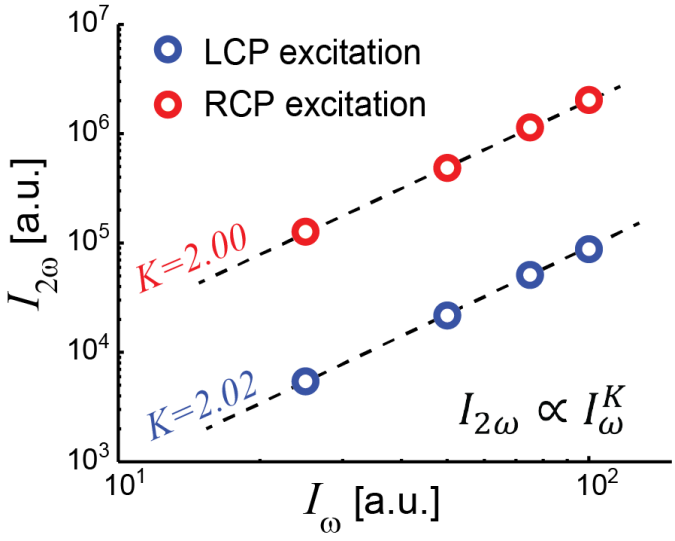

Figure 3.10: The SHG generation dependence on pump intensity, with blue and red markers representing SHG levels under LCP and RCP illumination, respectively. The dashed lines represent fitted curves that display a near-perfect quadratic relation relative to the incident intensity.

We also measured the dependence of SHG signals on the intensity of the circularly polarized pump lights, as shown in the log-log plot in Figure 3.10. As

expected, both the LCP and RCP illuminated samples demonstrated a quadratic dependency of $I_{2\omega} \propto I_{\omega}^{K}$, where the exponential factors K_{LCP}=2.02 and K_{RCP}=2.00 are obtained from the least square fitting.

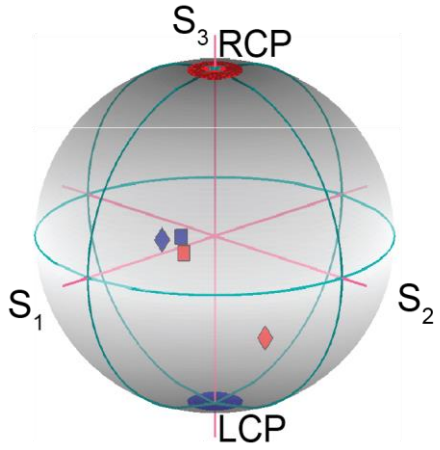

Figure 3.11: Stokes parameters of the outgoing nonlinear waves are plotted on a Poincare sphere from enantiomer A. The diamonds represent induced beams at the peak SHG wavelength of 950 nm, while the squares represent 810 nm where the chiral selective response is less distinguishable. The blue and red marker-fills follow the theme of the paper in representing LCP or RCP induced illumination.

To gain a better understanding of the properties of the second harmonic signal, Stokes polarimetry measurements for enantiomer A were performed at excitation wavelengths of 810 nm and 950 nm for both LCP and RCP waves, and are plotted on a Poincare sphere in Figure 4d. The interpretation of the Stokes

polarimetry measurements assessed can be furthered by calculating the degree of polarization (DOP), the degree of linear polarization (DOLP), and the degree of circular polarization (DOCP) of each second harmonic response which are all normalized to a value of 1. The nonlinear response induced via the RCP beam at 950 nm, where the SHG efficiency peaks, was mostly linearly polarized with a DOLP of 0.90, while all nonlinear responses showed roughly 0.5 for their DOLP. A consistent microscopic theory of the nonlinear response of this chiral metamaterial would be desirable, but is beyond the scope of this work.

3.6 Imaging

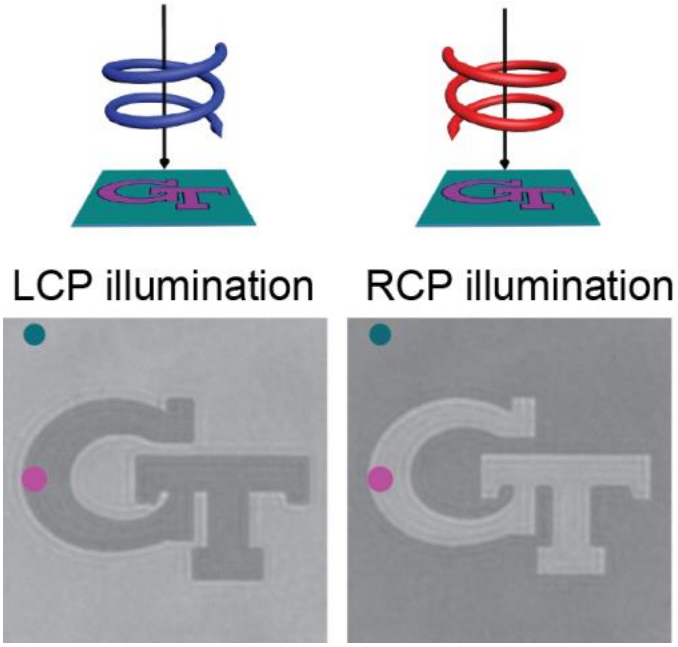

Figure 3.12: The transmission images of the GT sample illuminated with LCP and RCP waves, respectively. The cyan and magenta colored dots placed within the optical images of the sample demonstrate where enantiomers A and B are located.

Figure 3.12 depicts two linear images of the 'GT' patterned logo with different incident, circular polarizations. The images were taken in transmission mode with broadband illumination at a wavelength above 715 nm. The contrast between the two enantiomers is roughly 0.5. As mentioned in Figure 3.1d, the 'GT' pattern is composed of enantiomer A on the exterior of the logo and enantiomer B on the interior of the logo. The transmission spectra observed in Figure 3.4,a-b elucidates why the interior of the image is dark and the exterior is bright when illuminated with LCP light, as the transmission is higher for enantiomer A than it is for enantiomer B. The same reasoning explains why an inverted image is produced when RCP illumination is shown on the GT patterned sample.

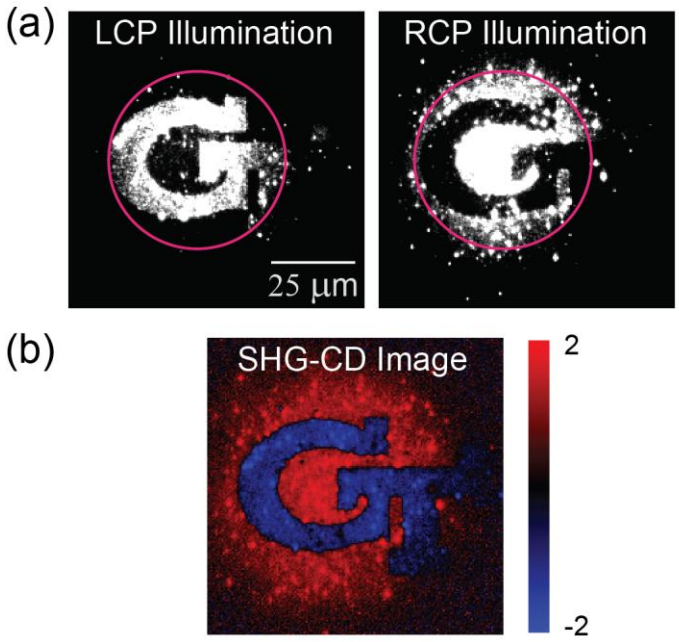

Figure 3.13: Nonlinear imaging. (a) Two nonlinear images of the 'GT' patterned logo are created via high intensity, excitation of RCP and LCP circularly polarized beams. (b) A point by point calculation of the SHG-CD was applied to create the image of the metamaterial pattern shown. Counts recovered from both RCP and LCP illumination displayed in Figure 3.13a were used to create this image.

The second harmonic images of the sample under circularly polarized excitation lights are depicted in Figure 3.13a. The two enantiomers exhibit opposite SHG conversion efficiency, which corresponds to their chiral selective nature as evidenced from the inverted image polarity in Figure 3.13a. The hotspots in these images, which represent the local variation in the nonlinear responses of individual

meta-atoms, are likely to result from the local defects, such as random surface roughness and coupling of these metallic grain, that occasionally favor the generation of harmonic waves under specific excitation conditions.[46] Random features in nanoscale metallic structures, such as irregularly-shaped metal particles and fractal aggregates, are known to enable localized, enhanced nonlinear optical processes.[81] Despite the local hotspots in the SHG images resulting from the local defects of the sample, the micrometer-scale features of the GT logo, including the sharp corners and the boundary between the two enantiomer zones, are very well resolved within the excited region of the pattern. The contrast of the SHG images is an order of magnitude stronger than that of the linear images shown in Figure 3.12, thanks to the extraordinary large SHG-CD in our chiral metamaterial. To further illustrate the contrast produced by the enantiomers, a SHG-CD image (Figure 3.13b) was created by applying the formula mentioned above to the SHG images in Figure 3.13a in a pixel-by-pixel manner. The equation that governs SHG-CD is extremely useful in differentiating between two chiral enantiomers in Figure 3.13b because it removes hot spots within our image. The defined contrast in this image provides an incredible ability in visualizing the chirality of metamaterial nanostructures.

3.7 Conclusions & Outlook

In this chapter, we built on the realm of chiroptics by using nonlinear imaging and spectroscopy to study the two artificial enantiomers of a twisted-arc metamaterial. As the significance of chiral plasmonic structures plays a larger role in the future of optoelectronic platforms, the greater the need will be for characterization, analysis, and maintenance techniques of these platforms. Nonlinear spectroscopy and imaging of chiral metamaterials offers a unique look into the functionality and deployability of these structures, and serves as a readily accessible and intensely accurate tool for the study of chirally sensitive materials. Chiral metamaterials offer a strong platform to induce SHG via their plasmonic resonances and by naturally interfering with the $\chi^{(2)}$ susceptibility tensor, making these artificial structures the perfect tool to initiate a study of chiral-selective nonlinear interactions. Future projects will seek to use chirality and its more distinguishable nonlinear response to image not only metamaterials, but also chiral biological samples on metamaterials. In addition, these high-intensity probed chiral materials could also act as selective, nanoscale reactors by inducing position based, enantiomer selective reactions via resonance heating.

CHAPTER IV.

Metamaterials Enable Chiral-Selective Enhancement of Two-Photon Luminescence from Quantum Emitters

As natural chiral materials demonstrate limited circularly dichroic contrasts, enhancement of these polarization dependent signals has long been the focus of chiral metamaterial research. By manipulating the geometric chirality of resonant plasmonic nanostructures, we are capable of enhancing light confinement to amplify chiral modified, nonlinear signals from quantum emitters. The chiral center of the metamaterial is opened for direct access, where emitters occupy the most light-confining and chirally sensitive regions. The resulting two-photon emission profiles from circularly polarized excitations display mirrored symmetry for two enantiomer structures. The efficiency of the nonlinear signal directly correlates to the chiral resonance of the linear regime. The nonlinear emission signal is enhanced by 40× that of the emitters not embedded in the metamaterial and displays a 3× contrast for the opposite circular polarization. Such manipulations of nonlinear signals with metamaterials open pathways for diverse applications

where chiral selective signals are monitored, processed, and analyzed. In order to realize novel methods to enhance these effects, traditional near-field studies[82-84] which probe the surface of a structure with an achiral emitter have been attempted to gain further insight.[85-87]

In this paper, we build on the realm of optical chirality that organic chemists have traversed by studying chiral metamaterials infused with achiral quantum emitters in order to probe the nonlinear, near-field interaction of engineered chiral structures. While the near-field of chiral, plasmonic structures has previously been numerically [24, 88, 89] and experimentally [90, 91] studied, the study of the nonlinear, near-field interactions remains sparse. In particular, very limited insights have been provided in the literature on how to access, probe and exploit the chiral selective hot spots generated in chiral engineered nanostructures. In this regard, further investigation is necessary as chiral metamaterials have demonstrated enhanced chiral responses orders of magnitude higher for their nonlinear counterparts due to symmetry breaking of the electrooptic tensor.[46, 53, 92] Specifically, this research focuses on selective enhancement of achiral quantum dot emitters within close proximity of our bi-layered, chiral metamaterial structure, which has tuned resonance and strong circular dichroism. In particular, exposing the chiral center of the three-dimensional structure allows for probing and

modification of the nonlinear signal at the heart of the metamaterial's structural chirality. Quantum dots (QD) are useful in studying this metal nanostructure because they offer tiny unit volumes for close structural proximity, large intensities, narrow band emission and a wide absorption range. However, placing semiconductor nanocrystals nearby metal structures breeds concern as quenching of the photonic energy by the metal structure is possible. For example, placing QDs in the vicinity of rough films enhances excitation, while placing them near smooth films causes quenching via Ohmic losses.[93-95] The enhancement recognized in the rough films can be attributed to the lightning rod effect, where rough surfaces lead to stronger confinement and larger mode volumes.[96] In order to achieve emission enhancement from this metallic yet luminescent complex, the current generated radiative enhancement outside the metallic structure must over power the non-radiative Ohmic losses inside the metallic structure.[95, 97] In general, the observed enhancement is associated with the existence of resonant features produced by the nearby chiral nanostructures.

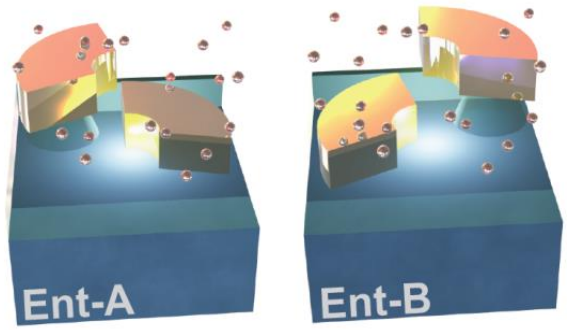

Figure 4.1: Schematic of enantiomer A (top) and enantiomer B (bottom) of the chiral metamaterial. QDs fill the volume mostly surrounding the region around the upper arc.

This project exhibits chiral manipulation of a locally emitted source and asymmetric enhancement of the nonlinear signal generated from two-photon excitation (TPE) of a nanocrystal emitter. The chiral contrast of the output nonlinear signal, two-photon luminescence (TPL), is witnessed when a circularly polarized input is incident on the near-field emitters embedded in the chiral arc structure. The subwavelength confinement and intense resonance provided by the silver arcs promotes selective enhancement and leads to pronounced nonlinear circular dichroism of the complex. The nonlinear signal offers a more distinguishable enhancement between circular polarizations than an input low intensity signal because TPE is a third-order nonlinear process, which enables the asymmetrically enhanced, chiral-selective behavior correlated to the meta-structure's spectral resonance in the linear regime. By employing geometrically

chiral structures to selectively enhance nonlinear optical effects a new brand of metamaterial is developed.

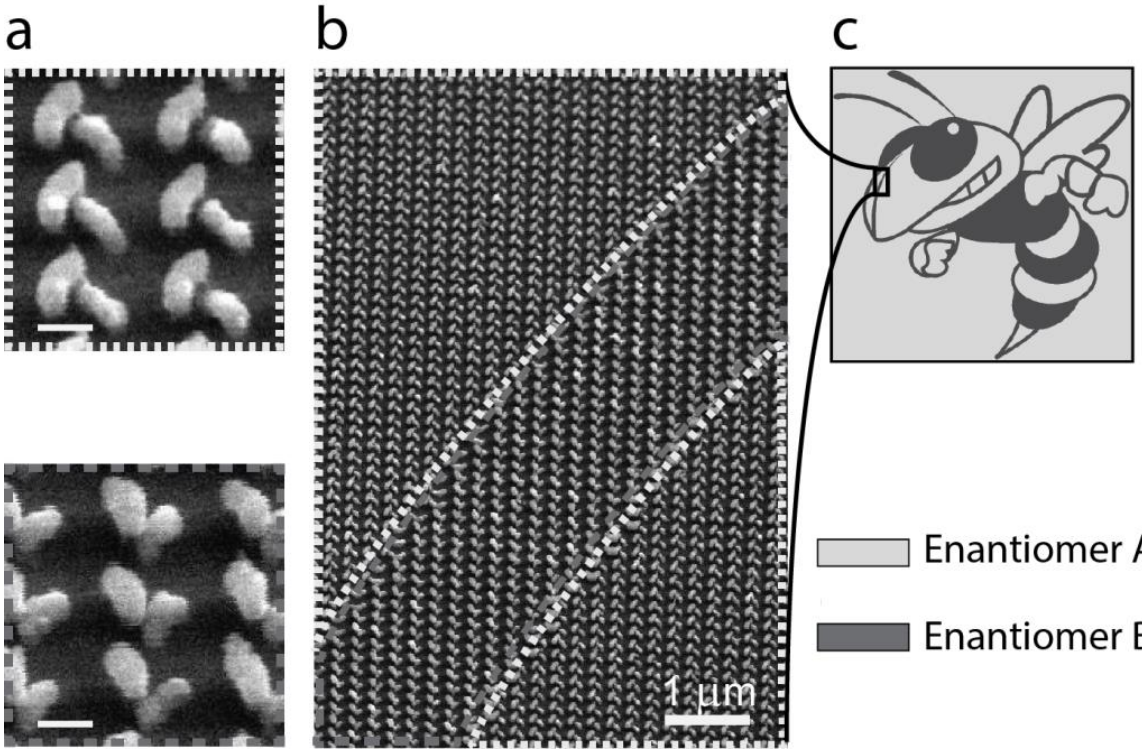

Figure 4.2: SEM images and nanoarc patterning (a) SEM images of the silver bi-layered structure of enantiomer A (top) and enantiomer B (bottom) before embedding the QDs. The scale bar in the figure represents 100 nm. Added roughness of the structure is due to plasma etching. (b) An SEM image of a patterned region involving both enantiomers. Here enantiomer B forms the inner portion of the line and enantiomer A the exterior portion. (c) A pattern of the GT mascot, 'Buzz,' that employs both enantiomers to provide the outline and

color. Enantiomer A fills the light gray space outside and inside the pattern and Enantiomer B fills the darker regions.

4.1 Fabrication

The helicity of the chiral arc pair leverages the structural simplicity necessary to create augmented chiroptical properties. The silver, chiral metamaterial and its enantiomer pair are depicted in the schematic of Figure 4.1. The graphic illustrates that the QD-polymer coating occupies the entire space around the upper chiral arc and only a slight portion of the lower arc. Scanning electron microscopy images, seen in Figure 4.2a, illustrate the bi-layered structure prior to encapsulating the arcs in the QD-polymer solution. A slight, lateral shift of 30 nm affects the entire patterned region, but later shows little effect on the overall chiral properties of the material. The SEM image in Figure 4.2b captures a small segment of a pattern utilizing enantiomer A and B before QD embedment. The two enantiomers provide the internal coloring of the Georgia Tech, yellow jacket mascot pattern as seen in Figure 4.3c. The embedded CdTe/ZnS core-shell quantum dots have a range of absorption that extends from the ultraviolet up until their emission peak at 640 nm, which is identified by the dashed line in the first two plots of Figure 4.2. The quantum emitters were chosen such that their emission

peak corresponds with one of the two chiral resonances of the twisted arc metamaterial.

A 1 inch^2 piece of glass was coated with an 800 nm polymethyl methacrylate (PMMA) layer as an electron beam resist. The resist was spun at 1000 rpm for 60 seconds with 2 seconds of ramping time and baked for 90 seconds at 180 °C. A subsequent layer of water soluble conductive polymer, Espacer 300z, was spun on at 2000 rpm for 30 seconds and 1 second of ramping time. The layers were then patterned with alignment marks via an electron beam lithography system (JEOL JBX-9300FS EBL). The conductive layer is then removed with DI water. The resist was developed in a mixture of isopropyl alcohol, and methyl isobutyl ketone in a 1:1 volume ratio for 2 minutes. The alignment marks were then deposited. Electron beam deposition amassed a 10 nm later of titanium as an adhesion layer and a 200 nm layer of silver. Acetone solution lifted-off the residual PMMA structure to complete the patterning of the alignment marks. In order to pattern the bottom layer of the chiral arc metamaterial, a second run of electron beam lithography employing the alignment markers was accomplished by reiterating the above steps. Once lift-off was completed, spin on glass (IC1-200, Futurrex Inc.) was coated with a spin speed of 5000 rpm for 60 seconds with a 2 second ramping time. The solvents

from the transparent dielectric were evaporated by heating the sample at 200 °C for 60 seconds. Plasma etching was performed to reduce the spacing between the bottom of the upper arc and the substrate to 72 nm. From here another round of electron beam lithography was applied to define the second chiral arc.

After lift-off of the PMMA for the third time, the sample was then partially plasma etched furthering the surface area of the structure exposed to air. This etching removes another portion of the spin-on glass and is reduced by roughly 50 nm, thereby exposing part of the first chiral arc and leaving the upper chiral arc standing only via a pillar. A layer of polylauryl methacrylate (PLMA) doped with quantum dots was spin coated on the surface of this exposed chiral arc structure. The coating solution consisted of CdTe/ZnS core-shell quantum dots in a 1:6 ratio of QDs to 4% solution of PLMA in toluene. The volume concentration of QDs surrounding the metamaterial structure is approximately 1/40 nm^3.

The completed chiral arc structure has the following parameters. The thickness of each arc is 42 nm and the width (from inner radius to outer radius) is 70 nm. The top of the lower arc is separated from the bottom of the upper chiral arc by roughly 30 nm. In enantiomer A, the upper arc is a quarter of a circle and has both of its horizontal faces aligned parallel to the walls of the unit cell. The

lower arc is adjusted 15 degrees clockwise from the parallel face. The periodicity of the unit cell is 225 nm. The enantiomer B is a mirror image of this structure.

4.2 Linear Response and Simulation

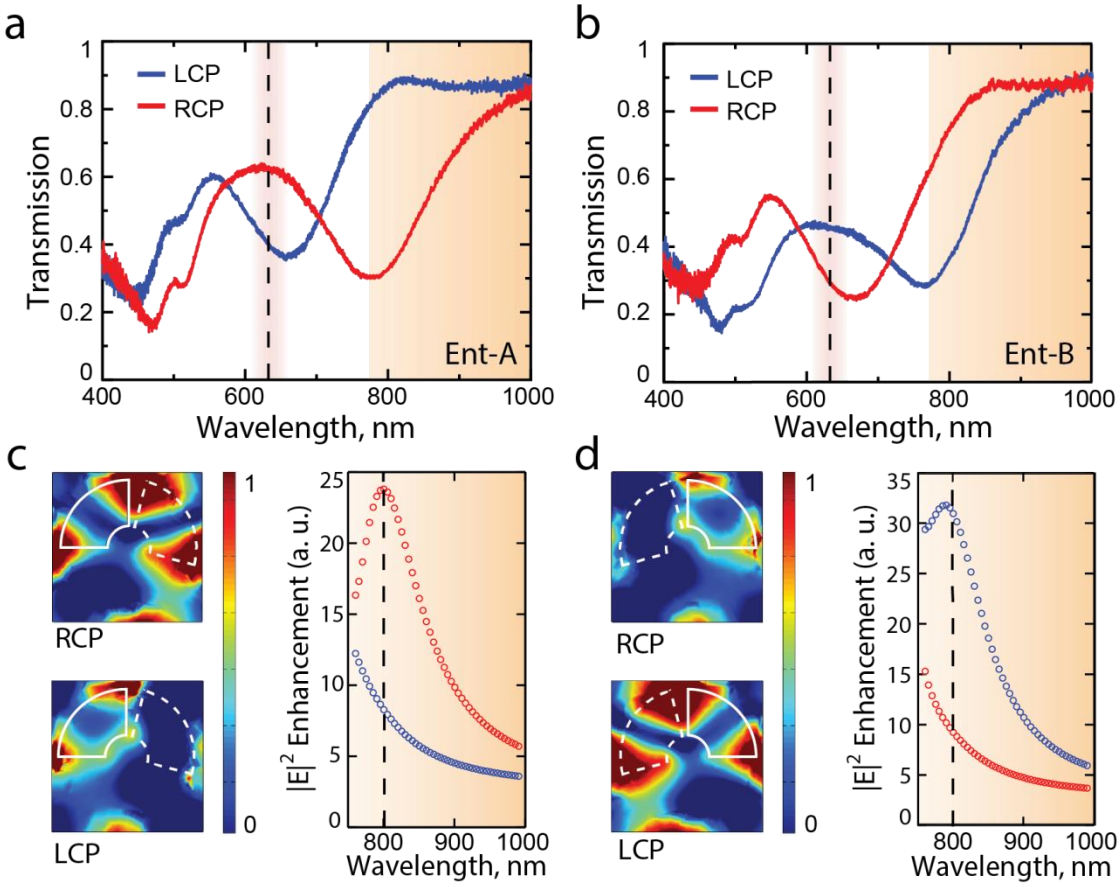

Figure 4.3: Chiral spectral resonances for selective enhancement. a) Transmission of LCP and RCP light incident on enantiomer A. An absorption resonance occurs at 640 nm for LCP incidence and another dip at 780 nm for RCP incidence. The dashed line accentuates the location of the QD emission wavelength and the grayed region displays the wavelengths that will be pumped

to produce TPE. b) Similarly in enantiomer B, resonances occur at 640 and 780 nm; however, for opposite circular polarizations. c) $|E|^2$ field enhancement of enantiomer A under left and right circular polarizations. A cross sectional cut, half way between the upper and lower arc, visualizes the log-scaled and normalized intensity of enantiomer A at 800 nm for RCP (top) and LCP (bottom). Simulation data for enantiomer A shows substantial enhancement of the intensity within the surrounding region of the chiral arc structure at a wavelength of 800 nm under RCP illumination. The simulation range (right) covers the pump wavelengths for the nonlinear excitation later performed. The dashed line corresponds to the spectral location where the $|E|^2$ maps are simulated. d) Chiral-selective field enhancement of enantiomer B. Cross sectional distributions of the $|E|^2$ are mirror images of the two enantiomers.

These chirally related, resonant dips in the arc's transmission profile, which can be seen in Figures 4.3a and 4.3b, occur at roughly 640 nm and 780 nm when probed with left and right circularly polarized beams respectively. The circular dichroism, which describes the transmission contrast between the two circular polarizations of opposite handedness, can reach as large as 50% at the wavelength of the chiral resonance. The transmission dips at these locations provide resonance based light confinement, which is mapped in Figures. 4.3c and 4.3d for both enantiomers respectively at λ=800 nm. This figure demonstrates the square of the

magnitude of the electric field under both circular polarizations at a cross sectional cut, half way between the upper and lower arc. The cross sectional graphics provide a logarithmic scale in order to reduce the visual amplification of the intensity located at the edges of the chiral arcs, due to lightning rod effects. Higher squared, magnitudes of the electric field are observed for the circularly polarized illumination that corresponds to the transmission dip experienced for a specified enantiomer. For example, enantiomer A shows a transmission dip at 800 nm for right circularly polarized light as seen in Figure 4.3a and thus a higher electric field magnitude squared as seen in Figure 4.3c (top). In comparison, the other circular polarization, Figure 4.3c (bottom) produces little intensity enhancement in the $|E|^2$ field map. Additional simulations were provided for the near-infrared regime, where the localized intensities were integrated within the surrounding region that the QDs were injected into. These simulations, plotted in the right of Figures 4.3c and 4.3d, demonstrate the strongest enhancement at a wavelength of 800 nm. A slight shift in the spectral, resonance location of enantiomer A in comparison to enantiomer B is shown and can be attributed to the asymmetry of the integration area, which corresponds to the location of the QDs hosted in the metamaterial structure. The spatially-averaged enhancement in $|E|^2$ reaches a factor of

approximately 30 near the resonance peak, which in turn implies a substantial, chiral-selective enhancement in nonlinear light-matter interactions.

4.3 Linear Optical characterization.

Linear transmission measurements of the metamaterial structure were performed by impinging circular polarized light onto the sample. A tungsten halogen light source was circularly polarized by employing a linear polarizer and a quarter wave plate. An objective was used to magnify the transmitted signal and was selectively filtered to measure only the proper spectral regions. Linear imaging was achieved by switching the broadband light source with either a HeNe laser or a Ti-sapphire laser tuned to 800 nm.

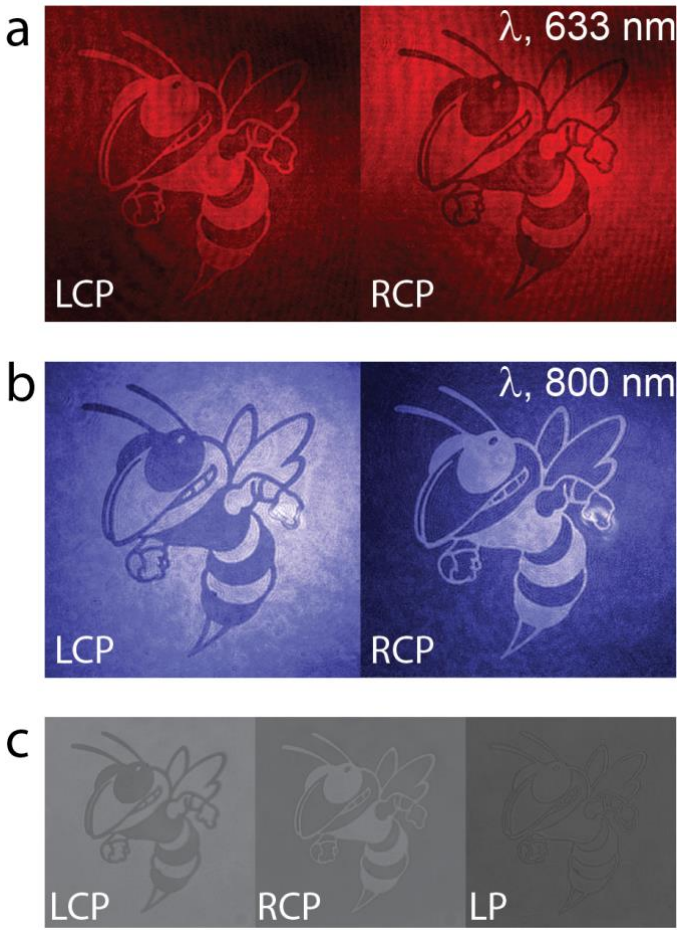

Figure 4.4: Linear transmission images of the GT mascot. a) Laser illuminated transmission image at 633nm for bother circular polarizations. The two colors in each picture are provided by the absorption or transmission of the light passing through one of the two enantiomers that compose the pattern b) Laser illumination with an 800nm source. c) Broadband illumination with a combination of filters around from 715-1000nm.

4.4 Imaging

Transmission images of the metamaterial pattern within their resonance bands of circular dichroism are provided in Figure 4.3. The same pattern of 'Buzz' the Georgia Tech mascot, which is composed of enantiomers A and B according to the pattern in Figure 4.2c, is imaged under different illumination conditions. These images are taken by impinging left or right circularly polarized light onto the patterned metamaterial region. As one of the circular polarization demonstrates low transmission for a specified enantiomer, the contrast produced between the two adjunct enantiomers at a specified resonant wavelength is very distinguishable. The first set of pictures is taken at the lower wavelength resonance of 633 nm and the second set, at the second resonance with λ=800 nm. Finally, three gray scaled graphics of 'Buzz' are shown in Figure 4.4c. The images are taken with a broadband source restricted to the near-infrared regime, 715 to 1000 nm, under three different polarizations, right circular, left circular and linear. The polarity of the images is related to the handedness of the circularly polarized illumination and a featureless gray image is produced under linearly polarized light. Having demonstrated the strength of our metamaterial to produce circularly polarized differentiation through these graphics, we will now proceed to evaluate the chiral-selective nonlinear emission from this hybrid metamaterial system.

4.5 Two photon luminescence

The goal of the QD embedded metamaterial is to characterize the near-field environment of the chiral arc structure with a fixed emission wavelength of 640 nm under varied excitation conditions. By illuminating the structure with a pulsed laser of high peak intensity, the nonlinear excitation of the QD-metamaterial complex leads to TPE of the QDs, which can be selectively enhanced depending on the incident circular polarization. The existence of TPE in semiconductor materials was first demonstrated in 1956,[98] but a recent usurping of the tool occurred when nanocrystalline, semiconducting structures became available. [88, 89, 99]

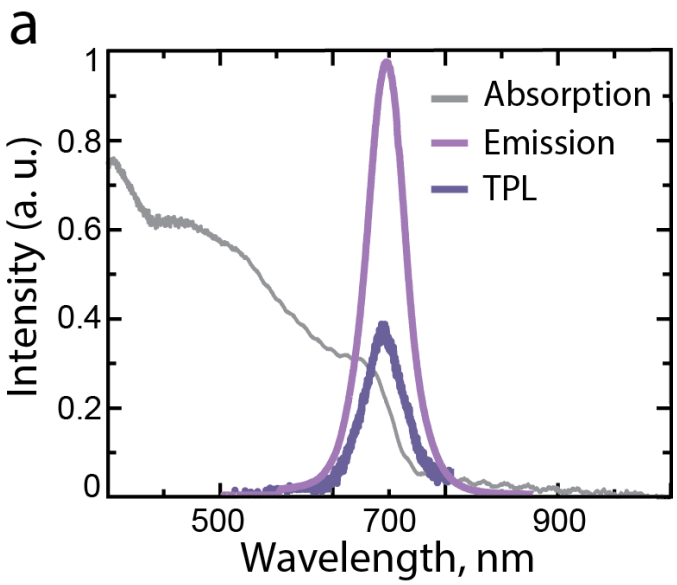

Figure 4.5: Emission profiles and absorption spectra for the embedded QDs. The absorption profile of the QDs demonstrates a characteristic cut off at a wavelength of 640 nm. The emission profile of the two-photon excitation is magnified in this image, as the two-photon excitation emission is orders of magnitude lower than the standard, emission profile under linear excitation.

In Figure 4.5 we show the typical absorption, linear emission and TPL profile of the QD-polymer coating. The two-photon excitation from the QD-polymer coating is scaled by many orders of magnitude in Figure 4.5a. The overlap of the linear and nonlinear emission peaks shows almost no spectral shift. The incident laser source at λ=800 nm was filtered to remove any unexpected light sources below 780 nm, thereby removing the possibility of lower wavelength excitation. The QD was also tested for circular polarization dependency by probing the substrate with left and right circular polarized beams. In this scenario, the QD emitted similar photon counts when probed with both polarizations, thereby removing any possibility of QD-circular polarization dependency. In addition, since quantum dots blink and are known to charge over time, [94, 100] extended exposures and averaging of measurements were conducted.

3.6 Nonlinear Characterization

Two-photon excitation measurements were achieved by impinging circularly polarized light from a tunable pulsed laser onto the sample, using a similar circular polarizing setup. The pulse train has a repetition rate of 80 MHz and a pulse width of 100 fs. Control of the input power and polarization was achieved by two sets of Glan-polarizers complimented with half wave plates. All nonlinear measurements except the intensity dependence of the metamaterial-QD complex were conducted at an input power of 2 mW and the QD substrate was measured at an input power of 10 mW. Power input measurements are explicitly stated in Figure 4.10. The spot size on the sample was roughly 60 μm^2. All measurements were conducted in ambient temperature.

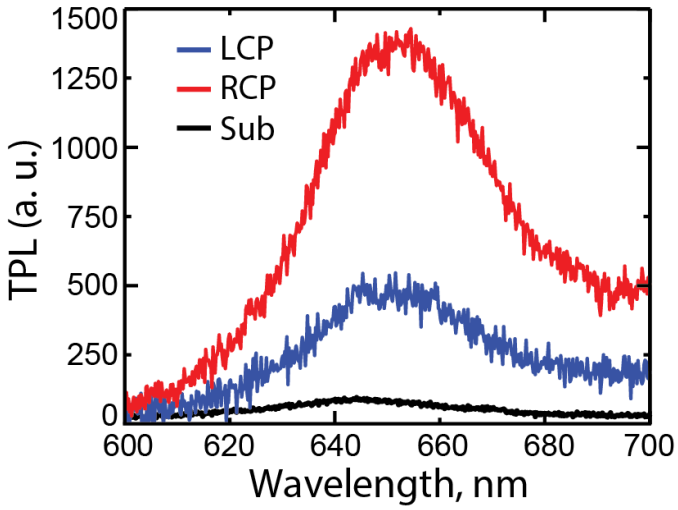

Figure 4.6: The two-photon excitation profile at 800 nm under different input circular polarizations for enantiomer A.

When embedded in the metamaterial, the QDs emit a higher TPL photon count than observed in just the polymer film of the same thickness and QD concentration, as seen in Figure 4.6. This figure displays the TPL enhancement from the metamaterial structure at a probe wavelength of 800 nm; this wavelength responds the most dramatically to the resonant conditions set by the chiral arc structure. The observed enhancement is attributed to the effectively increased absorption cross-sectional area of the QD. In addition, the emission enhancement from the QDs embedded in the metamaterial can be attributed to the resonant condition and confinement volume of the chiral arc pair, thereby intensifying the light energy in the nearby emitters. It should also be noted, that in Figure 4b the two-photon luminescence peak of the QD on the substrate occurs at an expected wavelength of 640 nm, however the two-photon luminescence peak of the QDs embedded in the metamaterial demonstrates a 10 nm red shift to 650 nm. This red shift is likely attributed to the spectrally dependent antenna effect from the metallic nanostructures. In addition, Figure 4.6 also shows an unusual asymmetry compared to the Gaussian shape of the QDs TPL. The increased emission profile seen at longer wavelengths, can be attributed to two-photon luminescence from the

metal of the metamaterial structure.[101, 102] Special care was taken to eliminate any influences from the metal based two-photon luminescence in subsequent integration of these peaks.

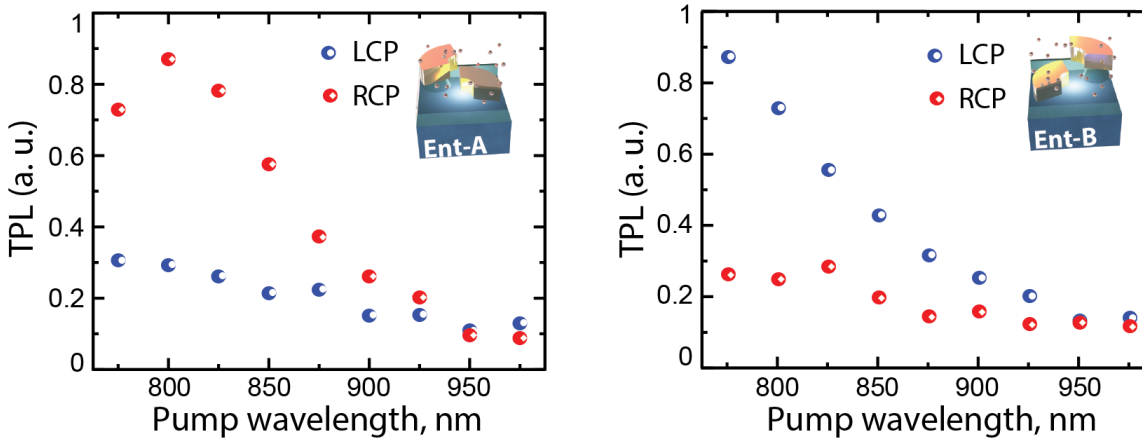

Figure 4.7: Two-photon excitation spectroscopy. The integrated two photon emission profile for enantiomer A for both circular polarizations is shown on the left. Peaks similar to those seen in Figure 4.5 are integrated to resolve this figure. The two-photon excitation spectroscopy of enantiomer B again demonstrates reversed polarity for the two circular polarizations.

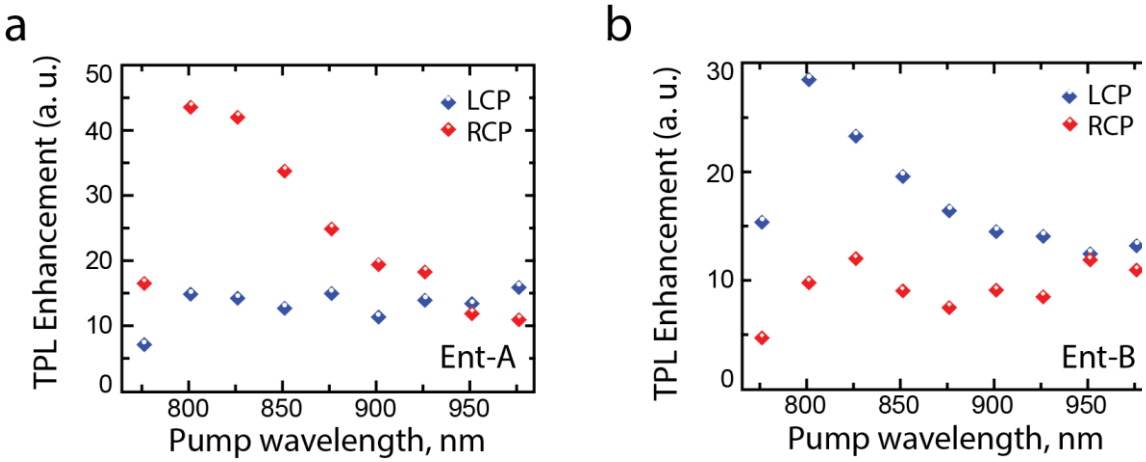

Figure 4.8: Chirally distinct two-photon luminescence. (a) Two-photon luminescence enhancement of enantiomer A under left and right circular polarizations. A large contrast between the two circular polarizations arises at 800 nm, where the linear excitation resonance occurs as seen in Figure 4.2c. The TPL enhancement is calculated by dividing the output luminescence from the QD-metamaterial complex by the luminescence from the QD film. (b) Enantiomer B shows switched magnitudes of TPL enhancement for the two circular polarizations.

In order to relate the near-field interactions of the metamaterial to its linear counterpart and gain a better understanding of the chiral, QD-nanoparticle interaction, a range of near-infrared wavelengths are probed under high peak power beams. Both enantiomers A and B are subjected to left and right circularly polarized light. The set of emission peaks obtained are similar to those shown in Figure 4.6. These peaks were integrated over a range of 80 nm to quantify the TPL intensity as a function of probe wavelength, from 775 to 975 nm, and the result is shown in Figures 4.7a and 4.7b. Enantiomer A demonstrates a significantly higher nonlinear signal for a RCP incident beam, as predicted by the simulation in Figure 4.3c. This signal enhancement is mirrored by Enantiomer B for its respective resonant polarization in the near infrared regime, LCP light. The concept of a resonant polarization can only be discussed in a certain wavelength range, as

outside of this limited range, the resonant polarization may switch. A couple distinct features are immediately noted in Figures 4.7a and 4.7b. For instance, the nonlinear contrast between the LCP and RCP beams drops substantially as the excitation wavelength moves away from the resonance peak around 800 nm. The bandwidth of this region is similar to the bandwidth of the linear circular dichroism region. As the nonlinear probed regime measurement is limited by the wavelength range of our system's setup, the overall circularly dichroic bandwidth of the nonlinear region might be larger. Moreover, these bandwidths occur at roughly the same spectral locations. For this reason, the reduced polarization dependency of the TPL at either end of the bandwidth can most likely be attributed to the resonance effects seen in the linear spectrum of Figure 4.3. Further extrapolating from Figure 4.3a and 4.3b, we note an increased absorption resonance for either right or left circular polarizations at wavelengths approaching 800 nm, for enantiomers A and B respectively. This linear resonance feature describes the relative emission maximum in Figure 4.7a, where the radiated nonlinear source is directly related, to the light confining ability of the metamaterial. In this way, the maximum TPL peak takes on the spectral location of the linear absorption maximum (transmission minimum). This trend is followed throughout the entire probe spectrum, such that at spectral locations where there is minimal

differentiation between the two circular polarizations in the linear regime, the nonlinear regime responds similarly.

The strong enhancement at the excitation wavelength of 800 nm introduces a disparate contrast in TPL between the two incident circular polarizations as seen in Figures 4.8a and 4.8b. Enantiomer A at this spectral location under RCP excitation demonstrates a chiral-TPL enhancement of 40× that of the QD substrate and an enhancement roughly 3× that for the LCP incident light. In mirror like contrast, the LCP excitation of enantiomer B demonstrates a distinction of 30× that of the QD-polymer coating and 3× that for the RCP excitation beam. The reduction of the enhancement for the non-resonant polarization demonstrates that the light confining ability of the structure is significantly reduced when the geometry of the mode is not aligned with that of the structures chiral nature for a given wavelength. The enhancement of the resonant polarization for a given enantiomer is also significantly reduced as the probe wavelength deviates from the resonance peak at 800 nm. The difference in the magnitude of enhancement from these two enantiomers is likely due to the asymmetric placement of the QDs in the metamaterial. Substantiating the enhancement data shown in Figures 4.8a and 4.8b, the series of simulations calculated for the same probe wavelengths that were

supported by our high peak intensity laser source provides similar results, as seen in Figures 4.3c and 4.3d.

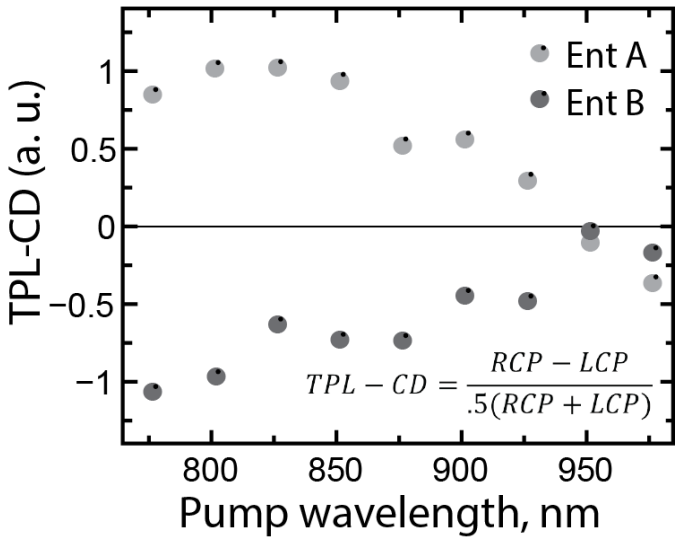

Figure 4.9: Two-photon luminescence - circular dichroism of QD's embedded in enantiomer A and B. TPL-CD is defined as the given equation in the figure and describes the difference in nonlinear output signal from the two circular polarizations. The circular dichroism is enhanced at the linear excitation resonance of the enantiomers.

The contrast of the nonlinear luminescence can be described by a figure of merit similar to linear circular dichroism. Two-photon luminescence-circular dichroism is defined as $TPL - CD = \frac{(RCP - LCP)}{.5(RCP + LCP)}$. This property provides a quick understanding of the contrast that a chiral structure demonstrates based on the

difference in two-photon emission from the two incident circular polarizations. Figure 4.9 demonstrates the contrast experienced from both circular polarizations on enantiomers A and B. The structures exhibit a flipped polarity in terms of TPL-CD which is demonstrated by the mirror symmetry presented across the x-axis of the plot. As chiral enhancement is increased at wavelengths approaching 800 nm, the two enantiomer structures show augmented TPL contrast.

Also shown in Figures 4.8a and 4.8b, the two-photon emission peak near 800 nm seems to be red-shifted from the linear spectrum's resonance dip at roughly 775 nm. However this red-shift may be anticipated as the spectral location of higher-order optical resonances often differs from that of their linear counterpart due to harmonic damping specifically in metals.[103] Based on this shift, it would seem that some damping occurs in the metamaterial as it is coupled into far-field transmission. In order to validate that the emission peak was in fact demonstrated from TPE and not by another linear source term, an analysis of power dependence was performed. Figure 4.10 demonstrates that TPE has a quadratic dependence on the input intensity for both the QDs in the metamaterial and on the substrate. The figure supplies a coefficient K, to describe the exponential dependence such that, $I_{2\omega} \propto I_{\omega}^{K}$, where $I_{2\omega}$ is the intensity of the nonlinear signal and I_{ω} is the input

probe beam intensity. The regression line of the logarithmic plot provides an exponential dependence of 2.0 $\pm$ 0.1 for the data points.

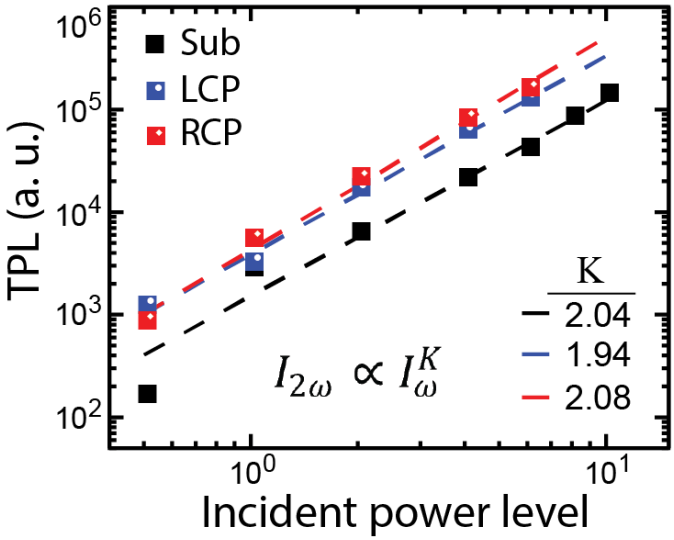

Figure 4.10: Two-photon luminescence as a function of the intensity of the pump light. All input polarizations demonstrate quasi-quadratic power dependence, evidencing two-photon excitation.

4.7 Conclusion

In this chapter, we demonstrate chiral-selective enhancement of two-photon luminescence from QDs embedded in a chiral metamaterial. The giant chiral response in a metamaterial, consisting of coupled nano-arcs, facilitates circular dichroic manipulation of the far-field intensity of locally emitted nonlinear signals.

In addition, the efficiency of the two-photon luminescence from the hybrid meta-system is directly correlated to the chiral resonance in the linear regime. By both, exposing the resonant near field of our chiral structure and inserting semiconductor nanocrystal emitters as indicators of localized chiral hotspots, we demonstrate two-photon enhancement of a chirally modified signal. Due to the light confining ability of the metamaterial under circularly polarized excitation, the two-photon luminescence from the hybrid system is enhanced by over 40 times with respect to a reference case without the metamaterial. The enhancement is chirality-enabled and is therefore sensitive to the handedness of the circularly polarized excitation; the enhancement factor demonstrates a contrast as large as 3 for the two circular polarizations observed in our experiment. Future works might look to reduce metallic particle quenching by introducing thin layered coatings around the metal structures and larger metallic spacing, thereby adding potential for nonlinear optical signal manipulation with reduced optical loss. This work represents a key demonstration in the realm of active chiral metamaterials, where the enhanced chiral fields are purposely exploited to enable chiral-selective light-matter interactions for imaging, sensing, and spectroscopic applications.

CHAPTER V.

INTENSITY-DEPENDENT MODULATION OF OPTICALLY ACTIVE SIGNALS IN A CHIRAL METAMATERIAL

Chiral media exhibit optical phenomena that provide distinctive responses from opposite circular polarizations. The disparity between these responses can be optimized by structurally engineering absorptive materials into chiral nanopatterns to form metamaterials that provide gigantic chiroptical resonances. In order to fully leverage the innate duality of chiral metamaterials for future optical technologies, it is essential to make such chiroptical responses tunable via external means. Here we report an optical metamaterial with tailored chiroptical effects in the nonlinear regime, which exhibits a pronounced shift in its circular dichroism spectrum under a modest level of excitation power. Strong nonlinear optical rotation is observed at key spectral locations, with an intensity-induced change of 14° in the polarization rotation from a metamaterial thickness of less than $\lambda/7$. The modulation of chiroptical responses by manipulation of input powers incident on chiral metamaterials offers potential for active optics such as all-optical switching and light modulation.

5.1 Introduction

Designing nano optic modulation systems is at the forefront of photonic research as the capacity for optical switching opens doors for applications in sensing, data transfer, quantum or photonic computing and so on. Metamaterials, nanoengineered structures composed of metallic building blocks embedded in dielectric media, demonstrate extensive potential for these nano-optical applications due to their highly sensitive plasmonic resonances and subwavelength interactions that create exotic macroscopic optical phenomena. More specifically, chiral metamaterials offer an exclusive route to modulation of these resonances when interacting with circularly polarized light. In general, chiral materials are structured media that possess a subunit whose mirror image cannot be superposed onto itself. The existence of this type of structural asymmetry gives rise to light-matter interactions that are sensitive to the handedness of the circular optical polarization. The difference in absorption between the two circular polarizations is known as circular dichroism and is one of the quantitative measurements of optical activity. The other, optical rotatory dispersion, describes the rotation of a plane of polarization of a linearly polarized beam as it passes through the chiral medium, and can be calculated from the circular dichroism using Kramers-Kronig relations.[104] These same definitions that were used to characterize chirality in

organic media are still used today to characterize artificially structured media with large optically active responses.[37, 50]

In order to design materials with artificially engineered chirality in the optical regime we look to metamaterials. Early forms of chiral optical metamaterials were designed with single layered patterns due to their relative ease of fabrication, but the chiral responses in such planar metallic structures are usually weak and typically require oblique incidence. To obtain pronounced chiroptical responses for transmitted light at normal incidence, we must imbue the mirrored discrepancy of the two circular polarizations in the material. Thus to achieve large chiroptical responses, an enantiomer must twist with the helical pitch of the polarized wave, in terms of rotation and distance travelled in the propagation direction. By integrating materials that have absorptive resonances in the prescribed frequency domain with nanoengineered structures that match the helical features of the incident wave, metamaterials with large circularly dichroic responses can be achieved. Various chiral structures explore this twist in the propagation direction including dual-layer twisted rosettes,[23] split-rings,[40, 105] arcs,[3, 47] gratings,[32] helices,[35] L-shapes,[26, 106] and arrays of twisted nano-rods.[28] In addition, chiral metamaterials typically have a lattice-constant factors smaller than the operating wavelength of interest, in order to instigate plasmonic resonances for

chiral selective absorption. The strength of these chiral metamaterials has been demonstrated in their applications as broadband circular polarizers,[28, 107] chiral mirrors,[108] negative refractive materials[51] and large scale chiroptical patterns.[109] While the height of chiral metamaterial research has taught us how to tailor these optically active effects, applications of nanophotonics demand that we seek out physical means to engineer active modulation into our photonic systems. This pressing need prompts us to explore all-optical control of chiroptical responses in photonic metamaterials.

As early as the 1950s, scientists theorized the opportunities available in anisotropic media when subjected to large beam intensities.[110-112] Higher input powers provided a change in the amount of optical rotation achieved by the anisotropic material.[112-116] The researchers recognized that by introducing large electric fields into the material, it could undergo thermal self-action or fast electronic transitions, one or both of which could induce a net gyrotropic effect in the material.[112] The thermal gradient can induce a change in the refractive index of the material, whereas electronic transitions modify the bandgap of a material. The net effect of these nonlinear interactions influences the electric susceptibility, where the diagonal and non-diagonal terms of the tensor describe the manipulation of the optically induced birefringence and the nonlinear change in rotation angle

respectively.[111] However it wasn't until 1979 that the electronic and thermal effects had been fully separated in crystals with chiroptical responses.[115] Further studies of nonlinear optical activity have been shown in liquid crystals,[117] optically active crystals,[113, 114, 118] chiral solutions[119-121] and a single-layer anisotropic metamaterial at angled incidence.[65] Engaging the noncentrosymmetric components of the susceptibility at high input powers allows the nonlinear generated signal to surpass the linear chiroptical contrast exhibited by the chiral structure.[3, 21, 122-124]

Here, we utilize the off diagonal terms of the electric permittivity tensor to manipulate the transmitted optical beam by function of input intensity. In this article, beams of varied optical power modify the two optically active signals, circular dichroism and optical rotatory dispersion, of a chiral metamaterial. The linear response of the chiral metamaterial is characterized, providing a maximum circular dichroic response of 0.58 and a maximum optical rotation of 2.3×10^{6} ° cm^{-1}. In measuring the nonlinear response, we demonstrate a blue-shift of 10 nm of the spectral resonance at 15 mW intensities and a nonlinear optical rotation coefficient of 1.76×10^{2} ° cm W^{-1}.

5.2 Fabrication

Sample Fabrication. The fabrication of the chiral metamaterial primarily consists of a few runs of aligned electron beam lithography. The metamaterial was fabricated on a 1×1 inch^2 glass substrate. Electron beam lithography (JEOL JBX-9300FS EBL) was carried out to define the lower elliptical layer. The bottom layer of the bilayered structure was formed by electron beam evaporation of 33 nm thick silver and a lift-off process. On the top of this silver structural layer, a transparent dielectric IC1-200 (Futurrex Inc.) was spin coated on. Afterwards, the dielectric was plasma etched to form a flat dielectric platform of 45 nm just above the substrate, for the subsequent patterning of the upper metallic layer. Another run of aligned electron beam lithography was repeated to form the upper elliptical array of the metamaterial. To reach the targeted performance and protect the sample from degradation, additional spin coating of the IC1-200 was performed to form a transparent top cladding of 1 μm in thickness.

The structural composition of the nanoengineered material is depicted in Figure 5.1. The unit cell is composed of two 33 nm silver films that have each been perforated with an ellipse, where the two major axes are askew from each other by an angle of 22.5 °. The first silver film is grown on a glass substrate and is separated from the other film by a 45 nm dielectric material with a refractive index similar

to glass. The exact geometrical parameters are listed in the caption of the figure. The structure is then encapsulated within the dielectric material to prevent any form of oxidation. The encapsulation of the metallic nanostructures within the dielectric ensures that the circular dichroic response remains the same independent of the direction the sample faces when light is incident on it. A secondary unit cell is shown in the lower half of Figure 5.1. This schematic is the mirror image of the upper unit cell and is known as its enantiomer. Chiral enantiomers are known to have mirror optical responses, just like they have mirror structural symmetry. An SEM image of the lower silver film is provided in the middle of Figure 5.1 and a second image of the upper pattern on top of the lower film is shown on the right of Figure 5.1. The orientation and size of the perforated ellipses demonstrate strong throughput in the physical structure. The alignment of the structure is well maintained, such that lateral precision between the upper and lower patterns is within 5 nm. A similar metamaterial design has exhibited large circular dichroic responses, [125, 126] making it an enticing structure to seek modification of its optically active signals in response to input powers.

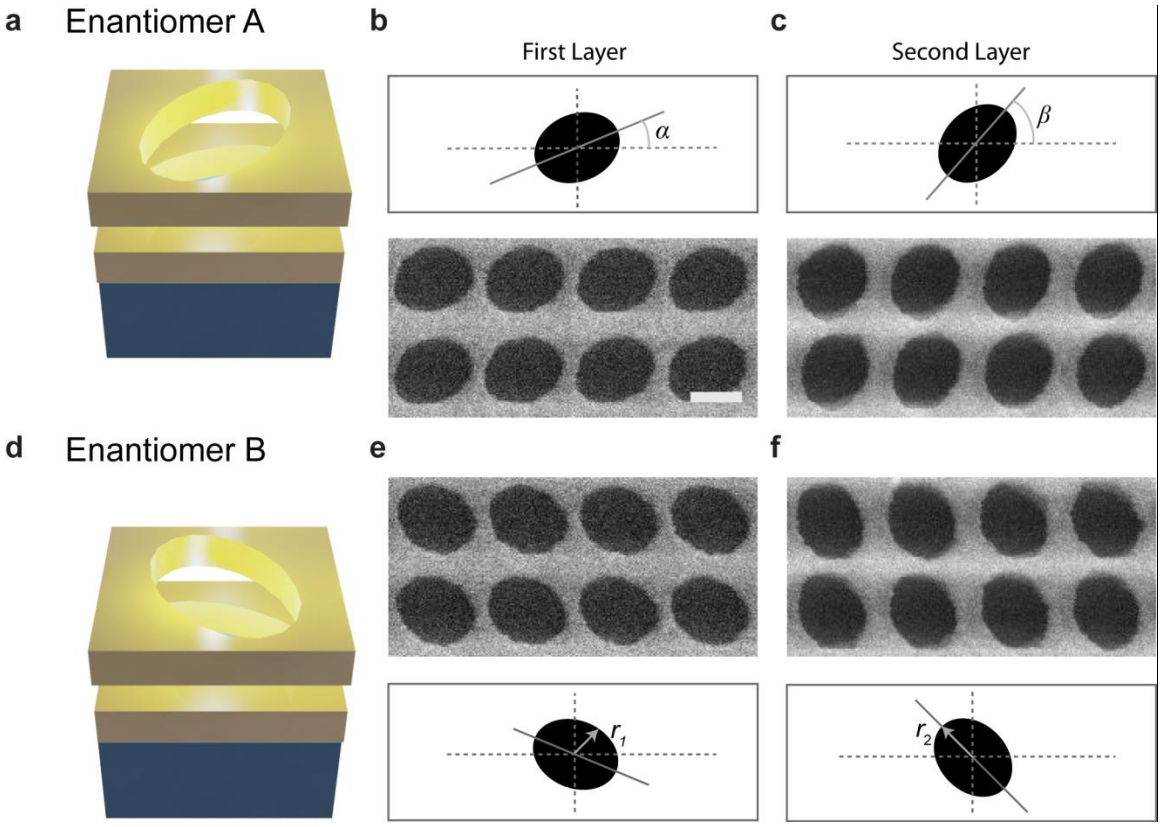

Figure 5.1: Schematic and micrographs of chiral metamaterial enantiomers. (a) A single unit cell of the metamaterial array. The nanoengineered material is composed of two silver films separated by 45 nm of a dielectric spacer (n=1.45) and perforated with two ellipses, where the major axes of the ellipses are skewed by 22.5°. (b) The SEM image depicts the first layer of the structure and is followed by an image of the (c) upper layer placed on top of the first. The scale bar in the image is 200 nm and the overall pitch of the unit cell is 350 nm. The characteristic parameters of these ellipses are r_1=115 nm, r_2= 150 nm and α=22.5°, β=45° from the coordinate axis. The second unit cell on the lower half of the figure is then created by aligning the ellipses such that the unit cells are mirror images of each

other known as enantiomers. (d) Schematics and SEM images of the (e) lower and (f) upper layers of enantiomer B are provided.

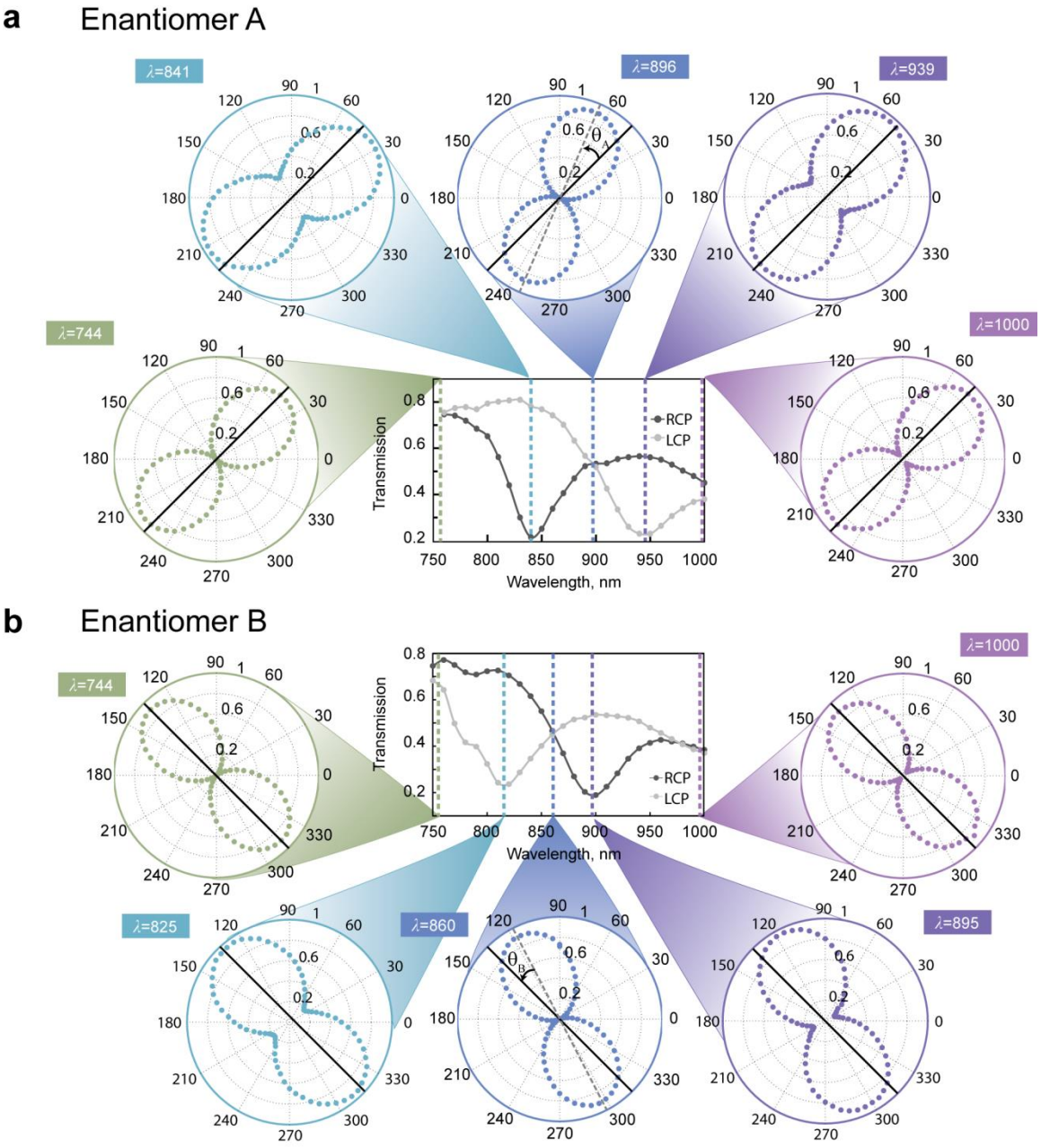

Figure 5.2: Experimental chiroptical responses for the two enantiomers. (a) Transmission spectra for left and right circular polarizations incident on

enantiomer A. The spectra present a maximum circular dichroic response of 0.58, where CD is defined as T_{RCP} - T_{LCP}. Optical rotation measurements were performed with a linear polarization input at 45°, denoted by the black line in the polarization graphics. The diagrams measured at 744 nm and 1 μm show that the linear polarization and orientation is maintained as it passes through the structure. At the spectral location of the resonance dips, 841 and 939 nm, the output polarization becomes elliptical and rotated. At the spectral cross-point in the central graphic, where $T_{\mathrm{RCP}} = T_{\mathrm{LCP}}$ at the wavelength of 896 nm, the transmitted light remains linearly polarized, but rotated by 25° clockwise. (b) Mirror responses are achieved for the transmission and optical rotation data of enantiomer B, when a linear polarization is input at an angle of 135°. Similar to enantiomer A, the linear polarization is maintained at the crosspoint wavelength where $T_{\mathrm{RCP}} = T_{\mathrm{LCP}}$, but the optical rotation is counter clockwise in this case.

4.4 Linear Optical Response

Linear Optical Characterization. Circularly polarized light provided by a tungsten light source modified with a linear polarizer and waveplate was incident on the metamaterial structure to measure its transmission characteristics. The measurement was performed using a homemade spectroscopy system dedicated to the characterization of small sample areas. The light was passed to a spectrometer

and a silicon CCD camera. To obtain the linear optical rotation data a similar setup was utilized. A linear polarization was input on the sample and the data was then collected at an output angle every 5 °.

In order to demonstrate this change in the transition from linear to nonlinear input powers, we first characterize the optically active signals of the metamaterial structure at low power exposures. Figure 5.2 depicts both the circular dichroic and optical rotatory responses for enantiomers A and B. The central two graphs for both enantiomers in Figure 5.2a and 5.2b depict the transmission of left and right circularly polarized waves. Just as the enantiomer structures are mirror images of each other, the linear chiroptical responses as shown in the transmission graphs are also complimentary to one another. The slight differences witnessed between the two spectra can be attributed to minor fabrication deviations between the enantiomeric materials. The largest magnitude of the transmission difference between the two circular polarizations is 0.58 for enantiomer A at 840 nm and 0.50 for enantiomer B at 810 nm. This contrast is defined here as circular dichroism, $CD = T_{\mathrm{RCP}} - T_{\mathrm{LCP}}$. We note that the two enantiomer structures are designed to be optically identical from both sides and thus do not support asymmetric transmission. This circular dichroic contrast is comparable to some of the best

metamaterial structures out there today.[24, 47, 126] The resonance dips occur over a broad spectrum in the near-infrared.

In addition, optical rotation measurements were performed from 740 nm to 1000 nm. The five polarization figures surrounding the transmission graphics represent the state of polarization of the transmitted wave at five selected spectral regions where the chiral metamaterial demonstrates its chiral nature or lack thereof. In each polar diagram, the peanut-shaped pattern describes the measured portion of the intensity along the transmission axis of a rotating polarizer at the output. Polarization diagrams are normalized and averaged over a spectral region of 5 nm, including 30 data points to reduce noise. In order to assess the largest optical rotation of the transmitted light from these structures, a different input polarization angle was necessary for either enantiomer. For enantiomer A, the input polarization is 45 ° and for enantiomer B, the angle is 135 °. This is denoted in the polarization diagrams by a solid black line at the respective angles for the two enantiomers. Intuitively, these locations are ideal for optical rotation as they are the physical locations where the two perforated ellipses intersect most closely, as seen in Figure 5.1. More details on how these input polarization angles were acquired can be found in Figure 5.3 and Figure 5.4.

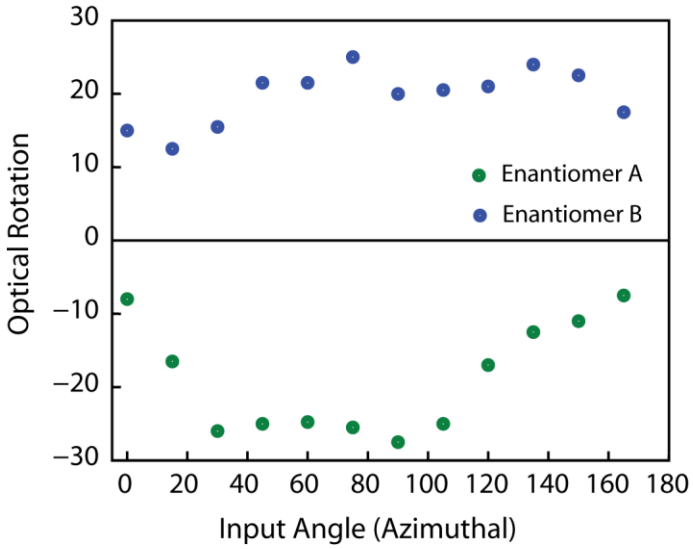

Figure 5.3: Optical rotation as a function of input angle. A linearly polarized beam is incident on the sample at 0° as denoted by Figure 5.4 and rotated. The rotation of the plane wave is recorded from the transmitted light.

Figure 5.3 shows how the metamaterial rotates the plane of polarization when linearly polarized waves are incident at differing input angles. In order to measure this, a linearly polarized wave was incident on the sample at varied input angles and a linear polarizer was rotated to find the location of the minima. The major axis of the polarization then corresponds to ±90 of the minimized rotation angle. It's important to note that the output polarization could vary between linear and elliptical. For this reason, when the output wave was elliptically polarized, the optical rotation corresponds to the major axis of the elliptically polarized wave. Based on these results, we chose to input the linearly polarized beam at 45° for enantiomer A and 135° for enantiomer B. The respective

polarization angle is shown in correspondence to the angle of the structures in Figure 5.4.

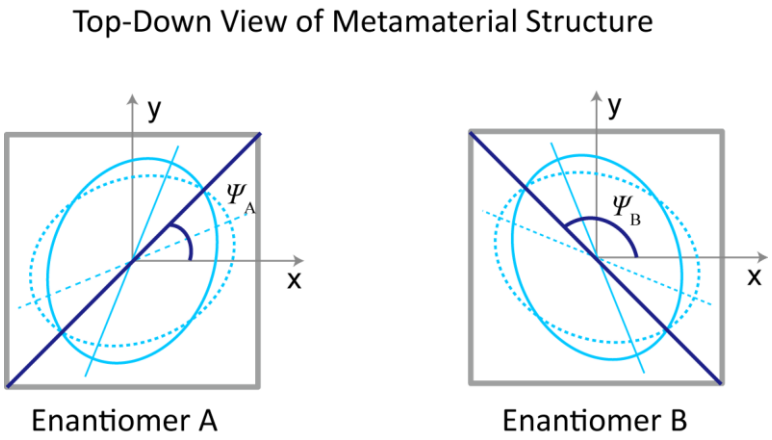

Figure 5.4: Orientation of linearly polarized wave incident on the chiral metamaterial. The dark blue line represents the input polarization chosen for the linear and nonlinear optical rotation results presented in Fig 2, Fig 3 and Fig 5. The angles Ψ_A and Ψ_B represent 45° and 135° respectively.

As in all measurements provided in this paper, the light passes through the glass substrate first. Next, the true optical rotation should be characterized at the cross point of the central graphic of Figure 5.2. At this cross point, left and right circular polarizations are transmitted equally, thereby allowing a linearly polarized beam to pass through without deformation of its polarization. As anticipated, the polarization diagrams for enantiomer A at 896 nm and for enantiomer B at 860 nm have a linearly polarized beam output. More importantly the linear polarization is rotated by 25 ° (clockwise) for enantiomer A and –20° (counter-clockwise) for

enantiomer B. Each of the enantiomeric metamaterials exhibit both a positive and negative cotton effect, switching optical rotation directions at both absorptive resonance as viewed in our supplementary movie in the original text.[5] Given a thickness of 111 nm of the metamaterial structure, we realize an optical rotation of $2.3\times10^{6}\ ^{\circ}\ mm^{-1}$ for enantiomer A and $1.8\times10^{6}\ ^{\circ}\ mm^{-1}$ for enantiomer B. These values are among the strongest optical rotation levels in photonic metamaterials reported to date.

We can now analyze the other 4 polarization graphics provided in Figure 5.2. The polarization diagrams that are collected at 740 and 1000 nm show a linear polarization output at an angle that is equivalent to the input polarization. For instance, enantiomer A shows an output polarization of 45 °, which is the same angle that the input polarization was incident. This congruency between the input and output polarization matches the response exhibited in the transmission spectra at this wavelength. Here both the right and left circularly polarized beams are transmitted equally, demonstrating that the structure cannot distinguish between the two input circular polarizations, and thusly has little chirally resonant-absorptive effects at these wavelengths. Two more polarization angle diagrams are provided at the resonance dips of the transmission spectra. These polarization diagrams demonstrate a loss of linear polarization, which is denoted by the

increased width at the waist of the peanut-shaped intensity profile of the polarization. The manifestation of this elliptically transmitted beam located at the resonance also corresponds to the lack of transmission from one circular polarization but not the other. As a linearly polarized beam can be decomposed into both left and right circular polarizations, this loss of linearity is anticipated. This change in polarization as a function of wavelength is best understood and displayed in the attached video file published online.

The above mentioned experimental results are well matched with the simulation data provided in Figure 5.5. The simulated transmission spectra of circularly polarized lights on enantiomers A and B show perfectly complimentary spectra, with resonance dips at 818 and 885 nm. Figure 5.5 also hosts plots of optical rotation for the two materials. In the simulation, the input angle of the linearly polarized beam is the same as the one provided in the experimental data (45 ° for enantiomer A and 135 ° for enantiomer B). Maximum values of optical rotation are obtained; where the angle of rotation of the linear polarized wave as it passes through the materials is ~30 ° (clockwise) for enantiomer A and ~–30 ° (counter clockwise) for enantiomer B. The angle of rotation indicates the orientation of the major axis of the linear or elliptical beam. In addition, simulations of ellipticity are also provided. The ellipticity describes the shape of

the polarization ellipse of the electric field, where a value of $\eta = +1$ corresponds to a right circular polarization, $\eta = -1$ a left circular polarization and a value of $\eta = 0$ implies a linearly polarized wave. The equation of ellipticity in this work is defined by the ratio of the major axis to the minor axis of the electric field or the square root of the intensity. As evident in the experimental data, the responses of the optical rotation and ellipticity data are again mirror symmetric for the two enantiomers. The graphic of the ellipticity shows a maximum and minimum, where the sign of the cotton effect changes and the direction of the optical rotation changes. As denoted by the relation of circular dichroism to the optical rotatory dispersion by the Kramers-Kronig relations, we anticipate these closely related responses.

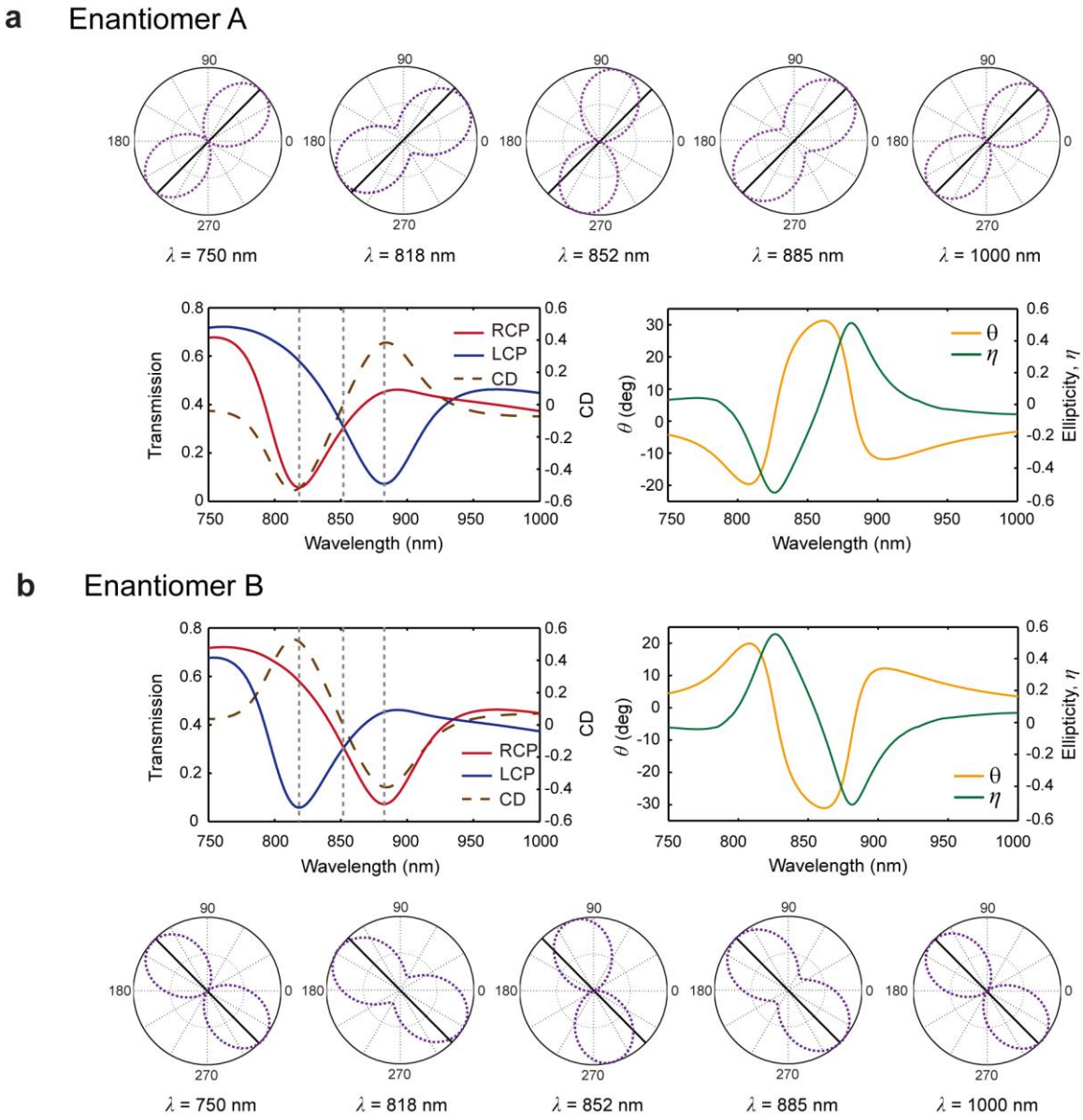

Figure 5.5: Simulations of circular dichroism and optical rotatory dispersion. (a) & (b) Simulated transmission spectra of circularly polarized lights on enantiomers A and B. Plots of optical rotation and ellipticity are provided. The input angle of the linearly polarized beam is the same as provided in the experimental data, 45° for enantiomer A and 135° for enantiomer B. A maximum of ~30° (clockwise) is obtained for the rotation of a linearly polarized beam as it passes through

enantiomer A and ~ –30° (counter clockwise) as it passes through enantiomer B. The angle of rotation indicates the orientation of the major axis of the linear or elliptical beam. The ellipticity describes the shape of the polarization of the electric field, where a value of $\eta = 0$ implies a linearly polarized beam and $\eta = +1$ corresponds to a right circular polarization and -1 to a left circular polarization. The responses of the optical rotation and ellipticity data are mirror symmetric for the two enantiomers.

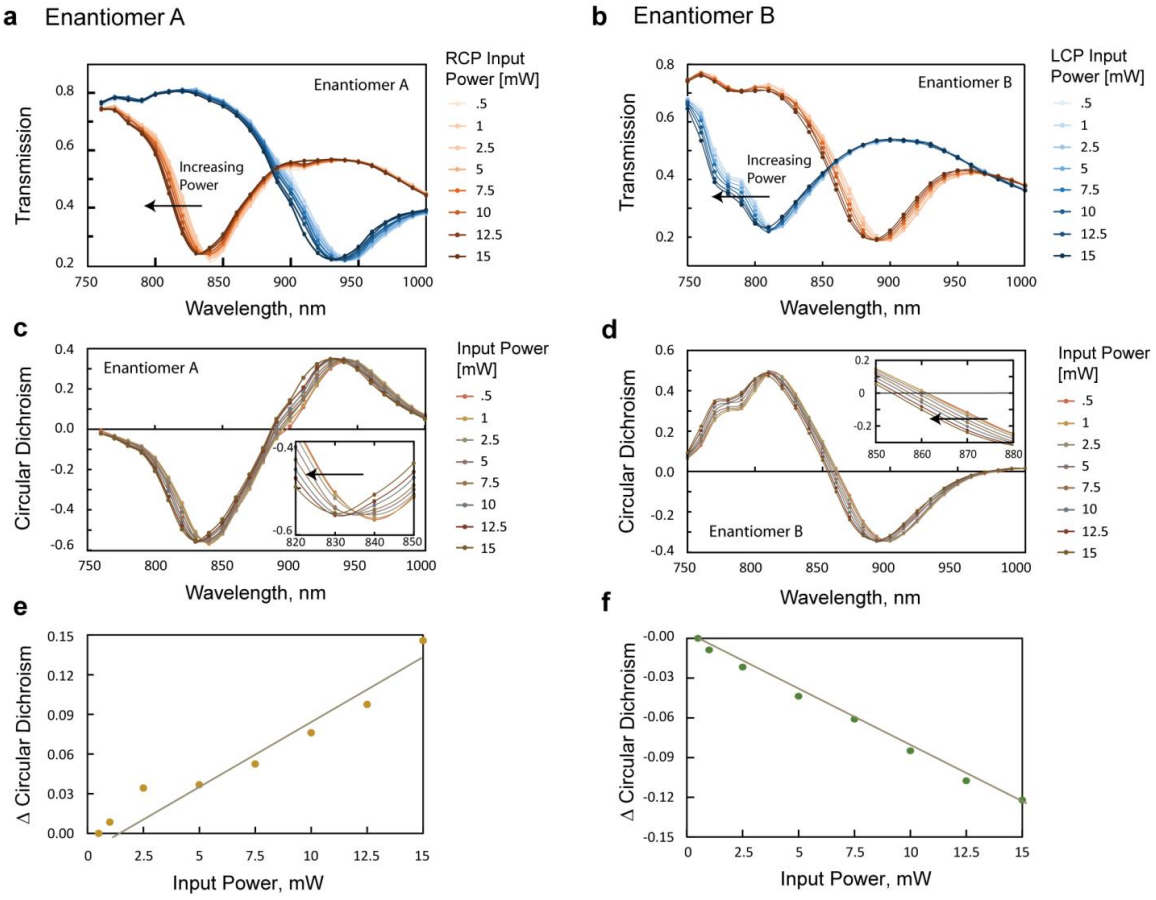

Figure 5.6: Intensity-dependent circular dichroism. (a) & (b) Transmission spectra of enantiomers A & B when subjected to varied intensities of right and left

circularly polarized light. As incident intensities are increased, the spectra of the resonances are blue shifted. This follows that the cross points and resonance dips are also shifted, implying that the corresponding optical rotation at higher intensities will also be effected. (c) & (d) Circular dichroic response of enantiomers A & B as a function of input intensity. The spectral shift for the resonance is approximately 10 nm for the two enantiomers as shown in the inset of (c) and (d), where the arrows show an increase in power. (e) & (f) Change in circular dichroism as a function of input power for the two enantiomers. The solid line acts as a guide for the eye. A change in circular dichroism of ~0.14 is demonstrated for a difference in power of 14.5 mW. Average excitation power of 1 mW corresponds to a peak intensity of 6×10^{7} W cm^{-2}.

5.4 Nonlinear Circular Dichroic Response

Nonlinear Optical Characterization. The excitation source for this experiment was a Ti-sapphire ultrafast oscillator (Spectra-Physics, Mai Tai HP) with a pulse duration of 100 fs, a repetition rate of 80 MHz. This laser was tuned from 740 to 1000 nm every 10 nm to acquire the data for the nonlinear measurements above. To measure the circular dichroic response, left and right circularly polarized waves were incident on the material. The incident beam had a diameter of roughly 15.8 μm. The power impinging on the sample was controlled by a waveplate and Glan-

polarizer to allow continuous modification of the optical power from 0.5 to 15 mW. The nonlinear optical rotation measurements were produced at three power levels by inputting a linear polarization at a specified input angle according to Figure 5.2, and analyzing the output polarization with a linear polarizer every 5 °. The exact values of the maximum optical rotation were achieved by fitting cos2 functions to the data, where the fits achieved coefficients of determination greater than 0.995. Average excitation power of 1 mW corresponds to a peak intensity of 6×107 W cm-2.

With the characterization of the linear response achieved, we can now move to study the nonlinear optical responses. Rather than investigate wave mixing signals that are generated from the chiral metamaterial as previously demonstrated, [3, 53, 124, 127] we can look at the transmission property of the material as input intensities are increased. Figures 5.6a and 5.6b provide the transmission spectra of enantiomers A and B when subjected to varied intensities of right and left circularly polarized light. As intensities are increased from 0.5 mW to 15 mW a shift in the spectral resonance of the metamaterial towards shorter wavelength is observed. As the spectral location of cross points and resonance dips are also shifted, we must later look at these new locations for nonlinear optical rotation effects. It's important to note that there is almost no threshold or

definitive transition as the optical response changes from the material's linear to nonlinear response. Rather, a gradual transition is achieved as power is increased. This leads us to ascribe this phenomenon to thermal modulation despite the fact that pulsed waves were input.[116] Figure 5.6c and 5.6d depict the circular dichroic response of enantiomers A & B as a function of input intensity. The spectral shift for the resonance is approximately 10 nm for the two enantiomers as shown in the inset of 4c and 4d. This shift occurs over a change in input power of 0.5 mW to 15 mW. Finally, Figs. 4e and 4f illustrate the change in circular dichroism as a function of input power for the two enantiomers. The solid line acts as a guide for the eye. The change in circular dichroism of ~0.14 is demonstrated for a difference in power of 14.5 mW, which corresponds to approximately a 1 % rate of change. Additional measurements were performed to see that the shift is not resulting from permanent damage of the metamaterial. These measurements provided in Figure 5.7, show that after input intensities were maximized to 20 mW, the power could be lowered and similar results could be achieved. As the structures are illuminated with an input power of 20 mW and subsequently tested at lower powers, it is evident that the change in transmission is not caused by permanent damage of the nanoengineered material.

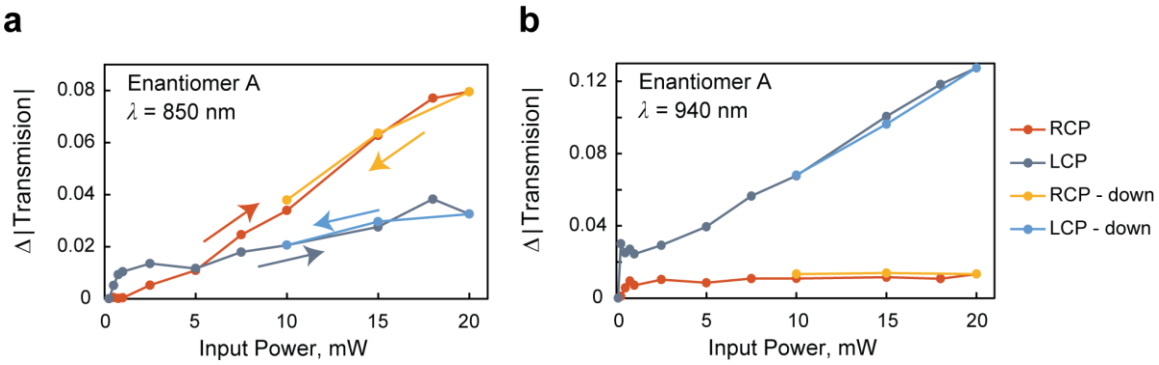

Figure 5.7: Powder dependent transmission at a single wavelength. Change in transmission as a function of input power for enantiomer A at the (a) first and (b) second resonance locations, 850 nm and 940 nm respectively.

5.5 Nonlinear Optical Rotation

Nonlinear optical rotation was studied by passing linearly polarized light at varied input intensities onto the sample. The polarization of light was input at the same angles as displayed in Figure 5.2, 45 ° for enantiomer A and 135 ° for enantiomer B. The nonlinear optical rotation was studied at three spectral locations – the two resonance dips and the wavelength where the two transmission curves cross, giving rise to a $CD = 0$. Figure 5.8 showcases the optical rotation for three input intensities when incident on the two samples at their resonant wavelengths. First, we will discuss how the optical rotation of the outgoing polarization is affected with higher input powers. This rotation is defined by the

long axis of the polarization ellipse. For enantiomer A at the first resonance, $\lambda =$ 841 nm, the polarization angle of the transmitted wave, is rotated from 31 ° at 1 mW to 37 ° for 7.5 mW and 45 ° at 15 mW and at the second resonance the rotation changes from 50 ° to 48 ° to 46 ° for the respective power increments. In this scenario, the outgoing rotation of the polarization returns towards the input polarization of 45 ° for enantiomer A. As for enantiomer B, the rotation of the polarization goes from 130 ° to 127 ° to 123 ° at the first resonant wavelength of 825 nm and 116 ° to 119 ° to 121 ° for the second resonance with a wavelength of 895 nm. The largest nonlinear optical rotation of the two enantiomers provides us with a nonlinear optical coefficient of 1.76×10^{2} ° cm W^{-1}. The ellipticity of the transmitted wave varies in correspondence with the input nonlinear power. As the resonance location of the metamaterial shifts with increasing beam power, the ellipticity will change in correspondence with the new resonant location at this higher input power. The changes in the waist of the peanut shape in the plots of Fig. 5 present this shift in the spectral resonance.

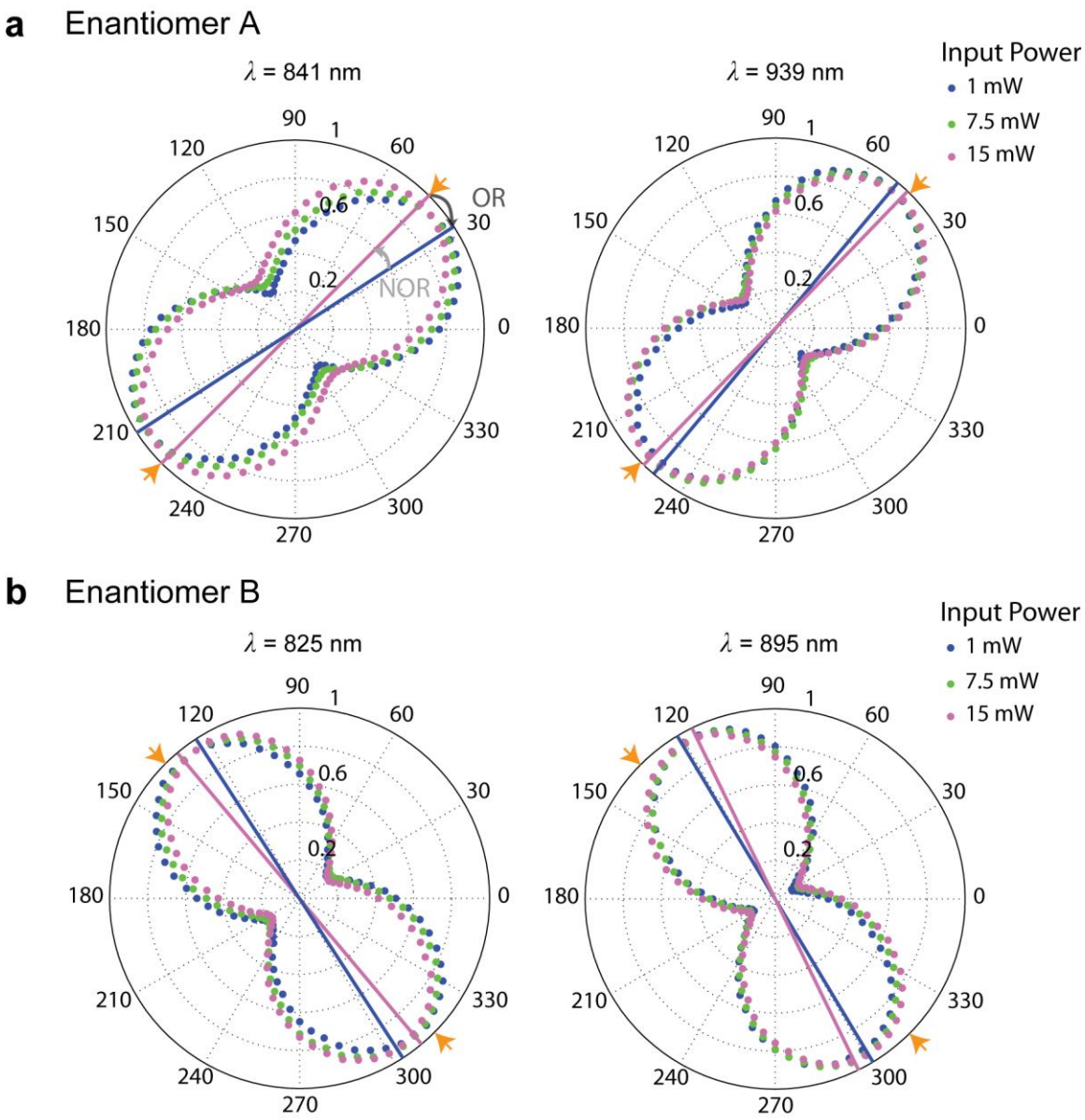

Figure 5.8: Intensity-dependent optical rotation. (a) Polarization diagrams of transmitted light at varied intensities from enantiomer A. Measurements of the shape of the polarization were obtained at the two resonance locations, $\lambda = 841$ nm and $\lambda = 939$ nm. As the power of the incident light is increased, the elliptical polarizations are rotated. The orange arrowheads indicate the input angle at which the linear polarization was incident on the sample. The blue and purple lines

indicate the orientation of the long axis of the elliptical polarization at 1 and 15 mW respectively. (b) Polarization diagrams of the output wave from enantiomer B. The diagrams were measured at wavelengths of 825 nm and 895 nm, corresponding to the resonance dips of the second enantiomer.

Measurements of optical rotation were also achieved at the cross-point of the transmission curves, where the circular dichroism is equal to zero as shown in Figure 5.9. The response here is relatively weak in comparison to the response at the resonance locations. At the cross point, the net change in transmission is zero for the two circular polarizations. As a linear polarization is a superposition of left and right circular polarizations, there is little tendency for the linearly polarized wave to rotate towards either resonance at higher powers. In the past, anisotropic measurements of nonlinear optical activity have been taken at convenient spectral locations where high laser powers are available. However, in our measurements we purposely focused on evaluating the optical rotation at the spectral locations where our metamaterial displays its strongest chiral optical activity. In doing so, we provide an in-depth nonlinear-spectral analysis of this chiral metamaterial with dual resonances.

In addition, to the nonlinear optical rotation data that was provided in the main text, measurements where the circular dichroism of the metamaterial was

equal to zero were also presented. At this spectral location, the linear polarization is maintained and the orientation is rotated. However, it is important to note that this inflection point in the circular dichroic spectra shifts with varied beam powers as demonstrated in Figure 5.9 (a) and (b). For enantiomer A, at low powers the circular dichroism is zero at 897 nm while at 15mw it is zero at 887 nm. For enantiomer B at low powers the CD=0 at 861 nm, while at 15 mW it is zero at a spectral location of 853 nm. For this reason, measurements of optical rotation for varied input powers were performed at both locations as seen in Figure 5.9 (c)-(f). The figures show that at the blue shifted wavelengths the waist of the linear polarization at lower intensities is larger than at higher intensities as expected. A slight rotation is observed for enantiomers A and B as beam power is increased at the blue-shifted locations; this is shown by the slight degree shift in the polarization data for higher powers. In general, the nonlinear optical rotation here is relatively weak in comparison to the response at the resonant locations. At the cross point, the difference in transmission is zero for the two circular polarizations. As a linear polarization is a superposition of left and right circular polarizations, there is little tendency for the linearly polarized wave to rotate towards either resonance at higher powers.

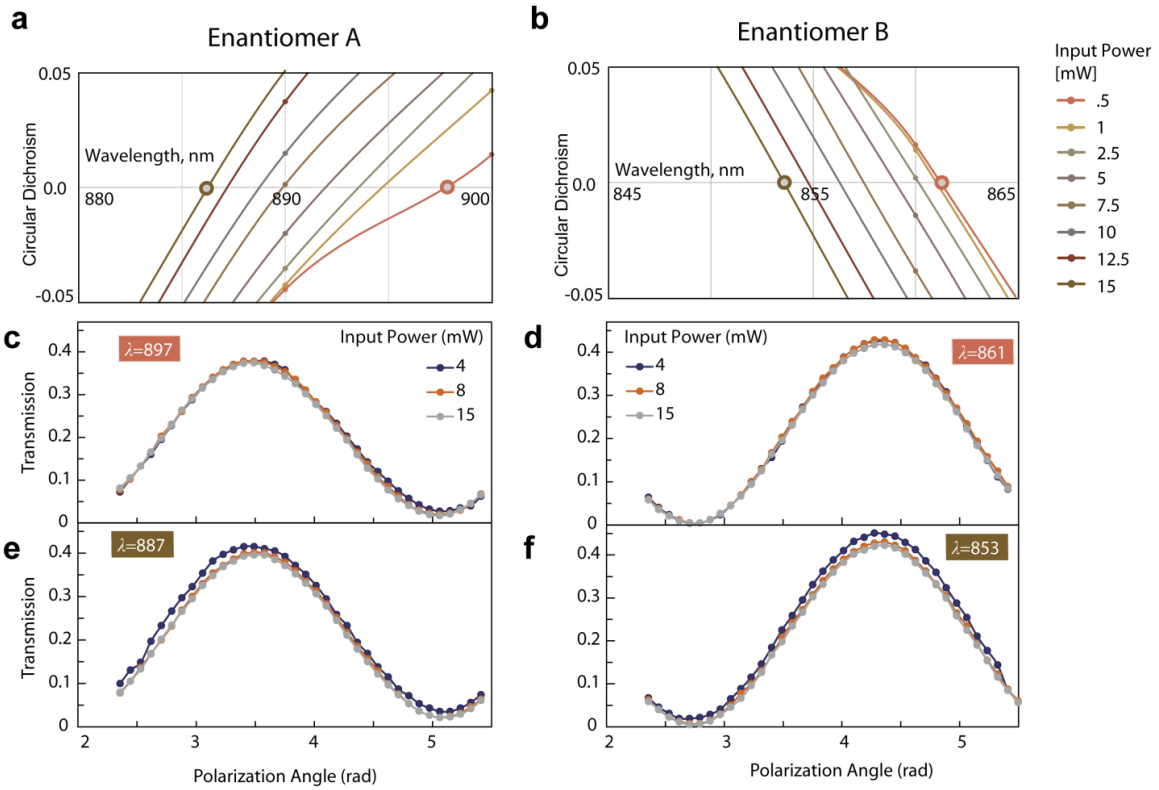

Figure 5.9: Intensity-dependent chiral optical rotation when CD=0. (a) & (b) Spectral locations where the circular dichroic response is zero, for input intensities between 0.5 mW and 15 mW for the two enantiomers. (c) Intensity-dependent optical rotation at the spectral location of 897 nm for enantiomer A, where the linear response achieves a CD=0. The response shows a small polarization waist with a transmission close to zero at roughly 5 radians. (e) Intensity varied optical rotation at 887 nm for enantiomer B. At 15 mW, the circular dichroic response is zero at 887 nm for enantiomer A. At this spectral location, the data taken at the input intensity of 4 mW exhibits a larger polarization waist compared to that of that at 15 mW intensity. (d) & (f) Similar intensity-dependent optical rotation measurements of enantiomer B at 851 and 861

nm. The polarization waist of the 4 mW input never reaches zero, whereas the data taken at a higher intensity shows a narrower polarization waist at these blue shifted wavelengths.

4.6 Conclusion

We have presented a chiral metamaterial that exhibits strong chiroptical responses in both the linear and nonlinear regimes. The metamaterial bares a circular dichroic response of 0.58 and a maximum optical rotation of 2.3×10^{6} ° cm^{-1}. In the nonlinear regime, we show a spectral blue-shift of 10 nm over the entire resonance spectrum of our chiral metamaterial in response to a power change of 15 mW. This phenomenon is most likely attributed to thermal self-action of the metamaterial. To better understand these effects, a detailed theoretical analysis that is beyond the scope of this work would be desired. A change in optical rotation of 1.76×10^{2} ° cm W^{-1} is achieved when the incident power is increased from 1 mW to 15 mW. To the best of our knowledge, no other material has demonstrated such a strong nonlinear chiroptical effect. Other materials in the literature and their polarization rotation per unit of optical intensity: $LiIO_3$ 10^{-11} ° cm W^{-1};[115] α-pinene $\leq10^{-11}$ ° cm W^{-1};[121] sucrose 2×10^{-11} ° cm W^{-1};[118, 121] an anisotropic metamaterial 3×10^{-4} ° cm W^{-1}.[65] To this extent, we believe that nonlinear optical activity can be useful in the development of optical modulation with chiral structures for applications in nanophotonic devices for optical switching and communications.

4.7 Recommendation

There is potential to see whether the aforementioned results might be due to thermal or electronic characteristics at high beam irradiance. In this respect, temporal measurements under circular polarizations using a femtosecond pulsed laser at a low repetition rate of 1000 kHz could elucidate these mechanisms. The low repetition rate would effectively reduce the temperature mechanisms. The above mentioned transitions can most likely be described by the optical Kerr effect which induces an effective change in the refractive index at high intensities of the metallic structures. In order to test this possibility, terms within the third rank tensor of the electric susceptibility could be detected using beam deflection.

Additionally, a Maker fringe set-up could be used to extract out χ^2 terms of the chiral metamaterial, thus quantifying the second order terms that give rise to the structure's second order chirality.

Finally, ceramic plasmonic structures offer the potential to test materials under much higher irradiance than silver nanomaterials. With this in mind, similar metamaterial structures fabricated from ceramic plasmonic materials such as TiN would be interesting to see if such a spectral-shift under large irradiance is present and what mechanisms might give rise to this phenomenon.

CHAPTER VI.

Preserving Spin States upon Reflection: Linear and Nonlinear Responses of a Chiral Meta-Mirror

As presented throughout the earlier parts of this thesis, circular dichroism evaluates the difference in absorption of left and right circularly polarized waves as it passes through a material. In the previous chapters of this work, the scattering light experienced by these planar metamaterial structures was minimal in comparison to the light absorbed or reflected. The lack of scattering allowed us to equate the transmission to the absorptive qualities of the material. In this chapter, we design a metamaterial that demonstrates a chiral asymmetry in a reflective manner and deem the material a chiral meta-mirror.

In this situation, the structure is in fact absorptive to one circular polarization and reflective to the other. More specifically, this meta-mirror is particularly different from conventional mirrors. In conventional mirrors, the handedness of the incident polarization is flipped upon reflection. However in this meta-mirror, the handedness of the incident polarization is maintained. This is

schematically demonstrated in Figure 6.1, for both handed, or enantiomeric, versions of the metamaterial. For example, when a left circularly polarized wave is incident on the enantiomer A, the light is absorbed, whereas when a right circularly polarized wave is incident, the light is reflected, but with the same handedness. The opposite can be said for the other enantiomeric material.

Chirality is most commonly identified with linear optical characterization techniques, however opposing circularly polarized waves can also display the same parity as a property of higher order optics. Here, a chiral metamaterial is presented that produces both distinguishable linear and nonlinear resonant features when probed with left and right circularly polarized incident beams in the visible to near-infrared regime. The material demonstrates a linear transmission contrast of 0.5 between left and right circular polarizations and a 20× contrast between second harmonic responses from the two incident polarizations. Nonlinear and linear response images probed with circularly polarized lights show strongly defined contrast.

In terms of symmetry, chirality is identified as an omnipresent property in both the inorganic and organic world. The determination of matter's chiral characteristics provides information about microscopic symmetry, such as the secondary structure of large biological molecules, and is crucial in molecular

identification and analysis[128]. When two objects have identical scalar physical properties, but opposite chiroptical responses, the structures are known as enantiomers. These types of materials have electric susceptibilities that respond differently to the handedness of the incident light, as the helical form of a circular polarized beam is in itself asymmetric. The twist in the polarization of the light is caused by the dynamic rotation of the electric and magnetic fields also known as the spin angular momentum of light. The direction of the optical torque carried by the light is denoted by the spin state as a positive or negative value for left and right circular polarized waves respectively. When the helical wave interacts with the chiral material, the polarization of the light can be controlled, based on chiroptical effects known as optical activity and circular dichroism (CD). However, conventional chiroptical devices are hindered by the extremely weak chiral response of natural materials. The desire to more efficiently use and control the interaction between circular polarizations and chiral media has inspired great interest in exploring artificial chiral structures. The modern study of artificial chirality can trace its roots back to the 1890s, when Bose's twisted jute rotated the plane of polarization for millimeter waves[129]. Harnessing plasmonic resonances that give rise to dramatically enhanced light-matter interaction, the recently emerging field of chiral metamaterials opens new opportunities for creating enormous chiroptical

responses. By applying an intrinsic design principle, to form resonant architectures non-superposable on their own mirror image, researchers have realized a variety of chiral metamaterials consisting of two- and three-dimensional meta-atoms, which have brought large chiral responses to the nanoscale [28, 35, 40, 41, 105, 130-140]. In particular, the remarkably strong chiroptical effects observed in chiral metamaterials have been reported to achieve ultra-compact photonic devices, such as circular polarizers [28, 35, 40, 132-135], for far-field polarization control of light. Owing to their circular-polarization-dependent field concentration, chiral metamaterials have also been employed to elicit increased chiral-selective nonlinearity [136-140]. Furthermore, by leveraging plasmonic enhanced optical chirality in the near-field, chiral nano-architectures have been used as ultrasensitive biosensing platforms for CD spectroscopic analysis [10, 141-145].

Although chiroptical properties are conventionally defined and characterized via transmission measurements, reflective chiroptical responses are also found in nature. For instance, the *Chrysina gloriosa*, a type of jeweled beetle, reflects circularly polarized light of the opposite handedness in a different fashion due to their structure of extracellular chitin in their exoskeleton[146]. Reflective chiroptical responses also can be found in artificial chiral media. For example, Zhang, *et al*, have studied the reflection behavior of chiral sculptured-thin-film

mirrors consisting of an array of helical nanowires and observed the circularly polarized emission from colloidal nanocrystal quantum dots confined in the corresponding micro-cavities[147]. More recently, by providing a proof-of-concept demonstration at microwave frequencies, Plum and Zheludev have elucidated the intriguing behaviors of metamaterial based chiral mirrors (abbreviated hereafter as meta-mirrors)[148]. In stark contrast to conventional mirrors that flip the spin state of incident light upon reflection at normal incidence, chiral meta-mirrors reflect light of one spin state while strongly absorbing the other. By presenting a theoretical analysis, Wang, *et al.*, has revealed that the necessary condition to achieve such a meta-mirror is to simultaneously break the n-fold rotational ($n > 2$) and mirror symmetry at the unit cell level[149]. The handedness-preserved reflection and chiral-selective absorption of meta-mirrors allow for the achievement of huge polarization contrast offering potential for applications in polarization manipulation and plasmonic enhanced chiroptical analysis. By leveraging chiral metamaterials in conjunction with hot-electron physics, unique devices can be created like that of the recently reported photodetector selectively sensitive to circularly polarized light [150].

In this paper, we demonstrate a chiral meta-mirror that only requires a single layer of electron-beam lithography patterning. Under reflection spectroscopy,

the material is designed to demonstrate a sharp resonance for a single circular polarization at 880 nm using numerical methods. The experimental measurement of the device at this wavelength yields a maximum circular dichroic contrast of 0.5. To demonstrate the unique features of the chiral meta-mirror, the two enantiomer structures are patterned into the shape of a hand and imaged. The images present the unique features of the meta-mirror, both strong absorption and the preservation of the incident circularly polarized wave. The meta-mirror also demonstrates chiral-selective behavior in the nonlinear regime. Producing second harmonic signals at varied intensities relative to the linear absorption spectra. With this in mind, imaging of the chiral pattern is achieved at the second harmonic wavelength under a pump excitation of 880 nm.

6.1 Designing a Spin Maintaining Material

The unit cell of the metamaterial is shown in Figure 6.1a,b for both enantiomers. The material consists of a lower back plane of silver, covered by a thin dielectric spacer, and further covered by a patterned gold film. The pattern in the unit cell is formed by the superposition of two rectangles offset by a few nanometers in opposite directions. The back plane of the silver material is optically thick ensuring null transmissivity. The structure provides a spin-state selective

resonant cavity. Scanning electron microscope (SEM) images of the fabricated structures are shown in Figure 6.1c,d for both enantiomers. This structure breaks symmetry conditions of the material, while only having a single patterned layer. The structure thus results in dramatically less fabrication, while being able to provide similar circular dichroic responses.

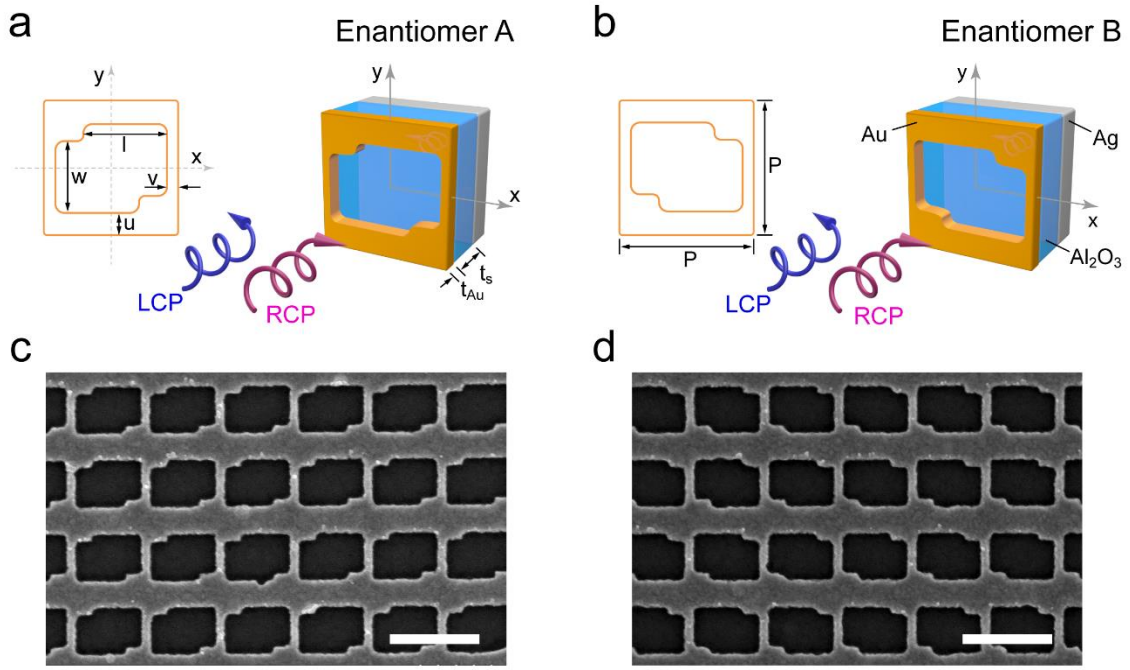

Figure 6.1: Schematics and SEM images of the metamaterial based chiral mirror for both enantiomers. (a) & (b) Schematic of the enantiomeric unit cells that consist of a patterned gold film, which is separated from an optically thick silver back plane by a thin Al_2O_3 spacer. The unit cell of the patterned layer is formed from the union of two intersecting rectangles. Geometrical parameters: $P = 400$ nm, $l = 260$ nm, $w = 210$ nm, $v = 25$ nm, $u = 75$ nm, $t_{\mathrm{Au}} = 50$ nm and $t_{\mathrm{s}} = 145$

nm. (c) & (d) SEM images of enantiomers A and B of the chiral meta-mirrors. Scale bar represents 500 nm.

The responses of the chiral metamaterial were provided using the commercial finite integration package CST Microwave Studio. In Figure 6.3a, a polarization sensitive reflection band at 850 nm is observed. For enantiomer A specifically, left circularly polarized (LCP) light will be absorbed and right circularly polarized (RCP) light will be reflected. The material reaches a value of up to ~0.8 in terms of a circular dichroic response. The opposite for enantiomer B can be seen under LCP and RCP waves, in Figure 6.3c; note that simulations are perfectly inverted. To evaluate the polarization behavior of the reflected light, an analysis must be done on the light reflected. Figure 6.3b & d demonstrate the decomposition of the reflected waves. The power reflection coefficient R_{LR} (R_{LL}) is defined as the RCP (LCP) portion of the reflected power from the metamaterial when LCP light is incident. The other two reflection coefficients follow the same naming methodology. The symmetry of the unit cell provides us with the same reflection spectra for both R_{LR} and R_{RL}. [151].

As expected, most chiral structures demonstrate a phenomena known as the magneto cotton effect. This is recognized when the incident LCP and RCP waves

cross. This point is often where the largest optical rotation is observed, though it was not evaluated in this experiment. Below this point, another absorption dip is recognized at 750 nm. Here the light which is absorbed is opposite that from the light that is reflected at the 880 nm absorption dip.

.

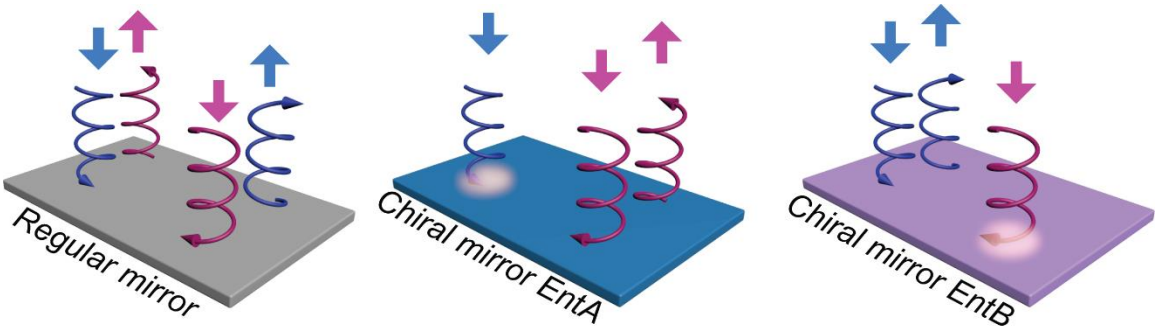

Figure 6.2: Schematics of the reflection behavior of the meta-mirror and a regular mirror. A meta-mirror composed of enantiomer A (B) reflects RCP (LCP) incident light and absorbs the entire LCP (RCP) component. The reflected light from the meta-mirror will preserve its initial state of circular polarization. For a regular mirror, the circularly polarized light will flip its circular polarization upon reflection at normal incidence.

We emphasize that, in addition to the chiral-selective absorption, there is a fundamental difference between our meta-mirror and a regular metallic mirror. It is known that, for ordinary reflective surfaces, including metallic mirrors, the

circularly polarized light will flip its spin state upon reflection (Figure 6.2e). In this case, the reflected light from a regular mirror contains no component of the input polarization and only contains light of the opposite spin, *i.e.*, $R_{\mathrm{LR}} = R_{\mathrm{RL}} = 100\%$ and $R_{\mathrm{RR}} = R_{\mathrm{LL}} = 0\%$. In sharp contrast, the reflected light from the meta-mirror will preserve its initial state of circular polarization. This reflection behavior can be attributed to the tailored light-matter interaction between the circular polarization states and the meta-mirror. This is made evident from the distribution of the electric field cut in a plane 50 nm beneath the patterned Au layer of both enantiomers, as shown in Figure 6.2f-i. Corresponding to the resonance dip identified in Figure 6.2a,c, pronounced circular-polarization-dependent field enhancement is seen at 852 nm in enantiomer A and B for incidence of LCP and RCP waves, respectively, which foreshadows the resonance enhanced chiral-selective optical nonlinearity as will be presented and discussed later.

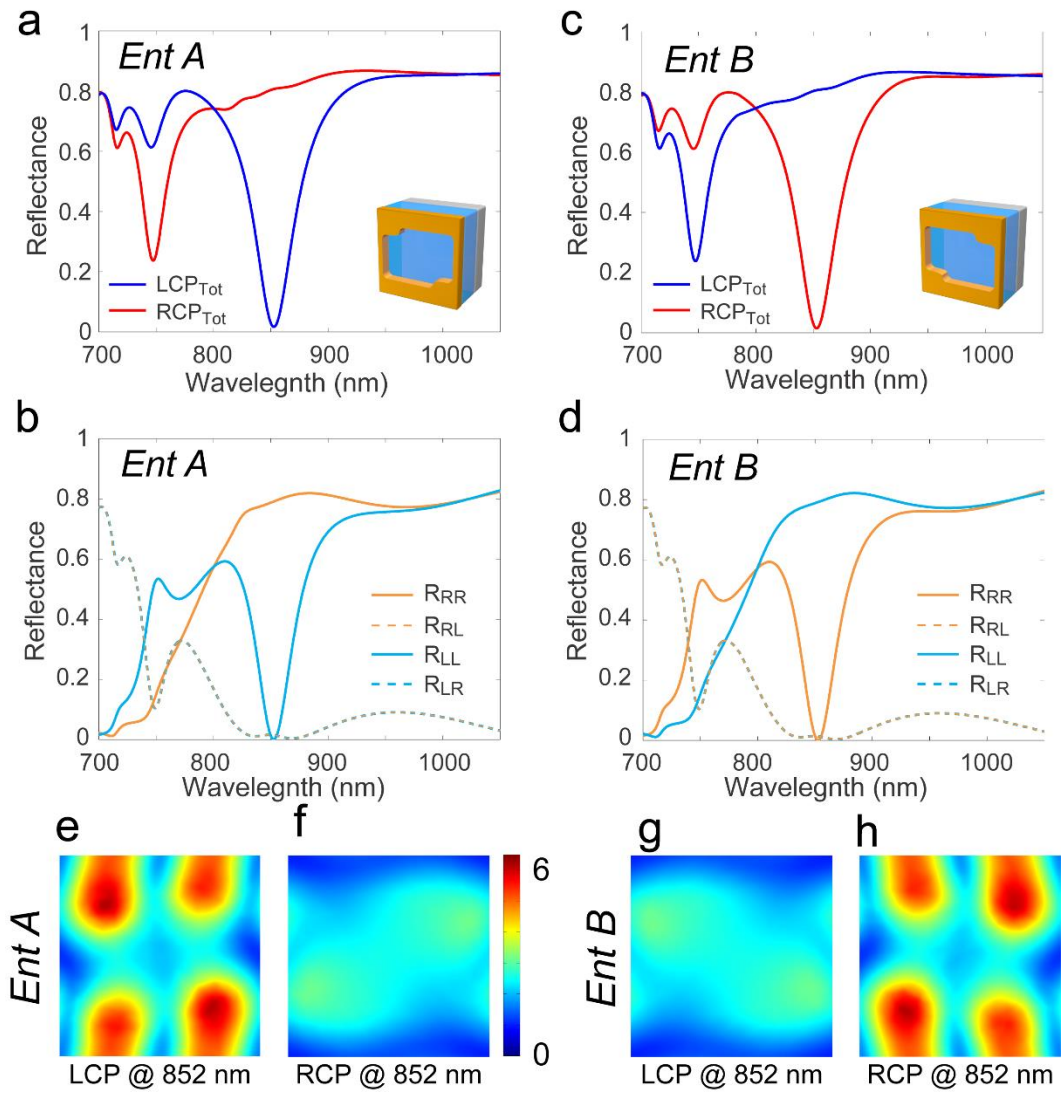

Figure 6.3: Simulated linear chiroptical responses of both enantiomers. (a) Total reflection spectra of enantiomer A under LCP and RCP illumination, respectively. (b) The corresponding reflection spectra of the co- and cross-polarization components. (c) & (d) Graphics of the counterparts for enantiomer B. A chiral selective reflection band around 850 nm can be identified. (e)& **(f)** The electric field distributions cut from a plane 50 nm beneath the Au layer of enantiomer A at the resonance

wavelength of 852 nm. (**g**) & (**h**) The electric field distributions of enantiomer B at 852 nm.

6.2 Analysis of Spin States from a Chiral Meta-mirror

To obtain reflection coefficients from the meta-mirror, we illuminated the sample with circularly polarized waves and analyzed the reflected light from the fabricated samples of both enantiomers. The measured results are shown in Figure 6.3 and all spectra were normalized to that of an unpatterned substrate. As illustrated in Figure 6.3a, a sharp reflection dip is observed at a wavelength around 880 nm for a LCP wave impinging upon enantiomer A, in comparison to the high reflectivity seen at the same band for RCP illumination. An additional pronounced but flipped circular dichroic contrast is seen in the wavelength range between 750 nm and 830 nm. When a circular polarized wave is incident on the sample, it is of interest to know whether the reflected beam maintains the input spin state or is flipped. The analysis of this is shown in Figure 6.3b. Analogously to the simulation, the metamaterial selectively absorbs one circular polarization and preserves spin state of the other. Furthermore, enantiomer B exhibits complementary chiral reflective behaviors, as indicated in Figure 6.3c and Figure 6.3d. The measured

data are in good agreement with the simulations shown in Figure 6.2, and the slight discrepancies most likely arise from fabrication imperfections.

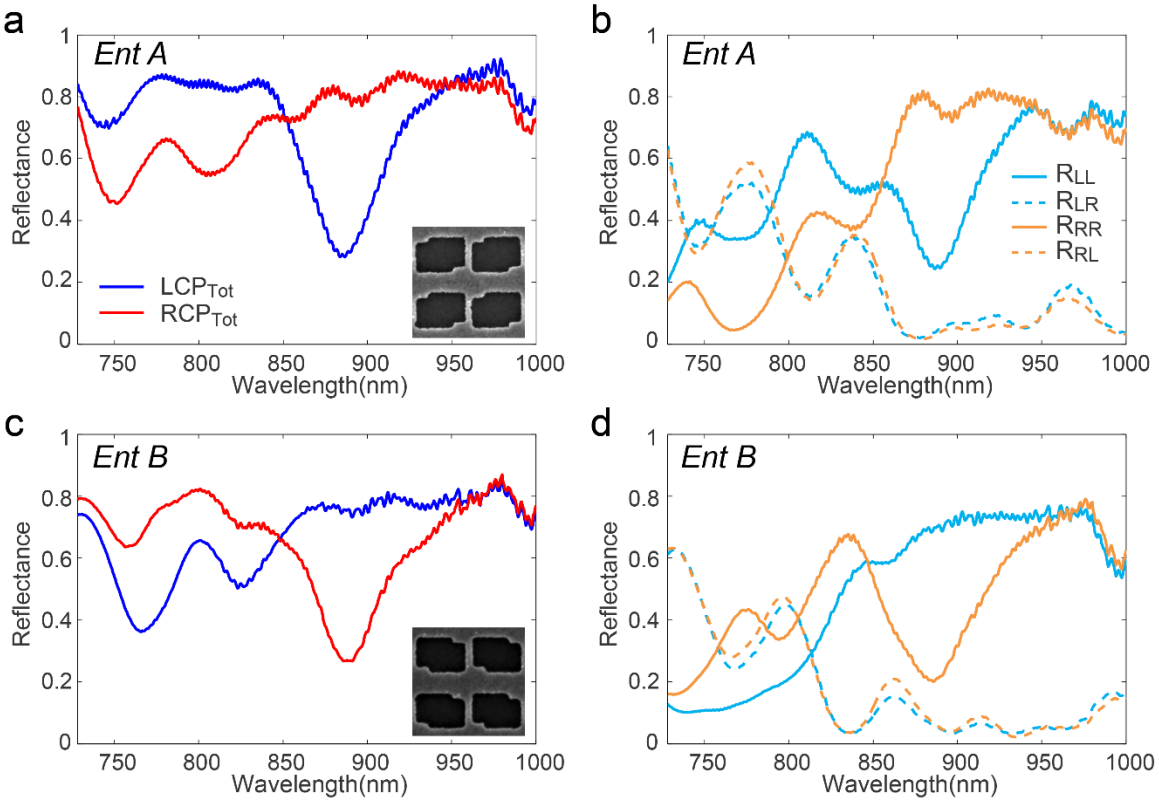

Figure 6.4: Measured linear chiroptical responses of both enantiomers. (a) Reflection spectra of enantiomer A under LCP and RCP illumination. (b) The corresponding reflection spectra of the co- and cross-polarized components. (c) Reflection spectra of enantiomer B under LCP and RCP illumination, respectively. (d) The corresponding reflection spectra of the co- and cross-polarization components for enantiomer B. Representative images of the corresponding samples are shown in the insets.

To better visualize the chiral selective absorption and the preserved circular polarization in our meta-mirrors, we created a pattern of a human hand using the enantiomeric unit cells and observe the images under select polarizations. Figure 6.4a depicts the configuration of the fabricated sample, in which enantiomer A and B were employed to form the exterior and interior regions of the hand. On the exterior of the pattern, a gold layer was left unpatterned to serve as a regular mirror in the background. According to the measured linear spectra (Figure 6.3), the wavelengths of incident light were selected to be in the range from 850 to 910 nm to optimize the image contrast. The hand pattern was then illuminated by LCP, linearly polarized, and RCP light, then collected with an objective and illustrated in Figure 4b-d, respectively. As evidenced by the figure, the hand pattern is only visible under circularly polarized illumination. In particular, a bright (dark) hand stands out from a dark (bright) background under LCP (RCP) incidence, which is due to the complementary reflection characteristics of enantiomer A and B under circularly polarized illumination as shown in Figure 6.3 from 850 to 910 nm. Essentially, the images presented in Figure 4b-d embody the reflection behavior discussed in Figure 6.3a,c, *i.e.*, the chiral-selective reflection of both enantiomers. Additionally, it should be noted that switching the spin state of the incident light reverses the contrast of the images. On the contrary, as shown

in Figure 6.4c, linearly or randomly polarized incidence is unable to distinguish the enantiomeric characteristics of the pattern and cannot produce recognizable images of the sample, because such input contains equal amounts of the two circular polarization components.

6.3 Visualizing Spin-Selective Preservation and Absorption

As we have stressed earlier, a regular mirror will flip the incident circular polarization to the opposite handedness, while a chiral meta-mirror preserves the circular state of polarization upon reflection. This drastic contrast can be visualized when we collect the images of the entire meta-pattern, including the unpatterned metallic surface in the surrounding area, after a circular polarization analyzer (Figs. 6.4e - 6.4g). The images serve as a visual presentation of the circular polarization preservation characteristic of the meta-mirror upon reflection that is observed in Figure 6.3b,d, after circular polarization analysis. As demonstrated in Figure 6.4e,f, for LCP incident light, a bright hand against a dark surrounding area can be seen with a LCP analyzer, while, the entire metamaterial pattern becomes dark when a RCP analyzer is applied. The contrast between the two enantiomers is even stronger when analyzed by circular polarization. Furthermore, the imaging behavior completely inverts when a RCP wave impinges upon the sample, *i.e.*, a

dark hand stands out with a bright background with a RCP analyzer implemented (Figure 6.4g), while an image identical to Figure 6.4f will be produced with a LCP analyzer inserted (not shown). These results comprehensively visualize the chiral-selective absorption and the circular polarization preservation properties of our meta-mirrors. It is even more intriguing to compare these behaviors with the imaging property of a regular mirror, here seen as the unpatterned area around the meta-mirror pattern. It can be seen that, the regular mirror will be dark (bright) when the incident light has the same (opposite) spin state as the circular analyzer (Figure 6.4e-g). In comparison, in the absence of the analyzers, the regular mirror is always bright (Figure 6.4b-d). This is consistent with the discussion above: an ordinary mirror flips the incoming circular polarization into the opposite one, while chiral meta-mirrors reflect and preserve the incoming polarization for a given spin state.

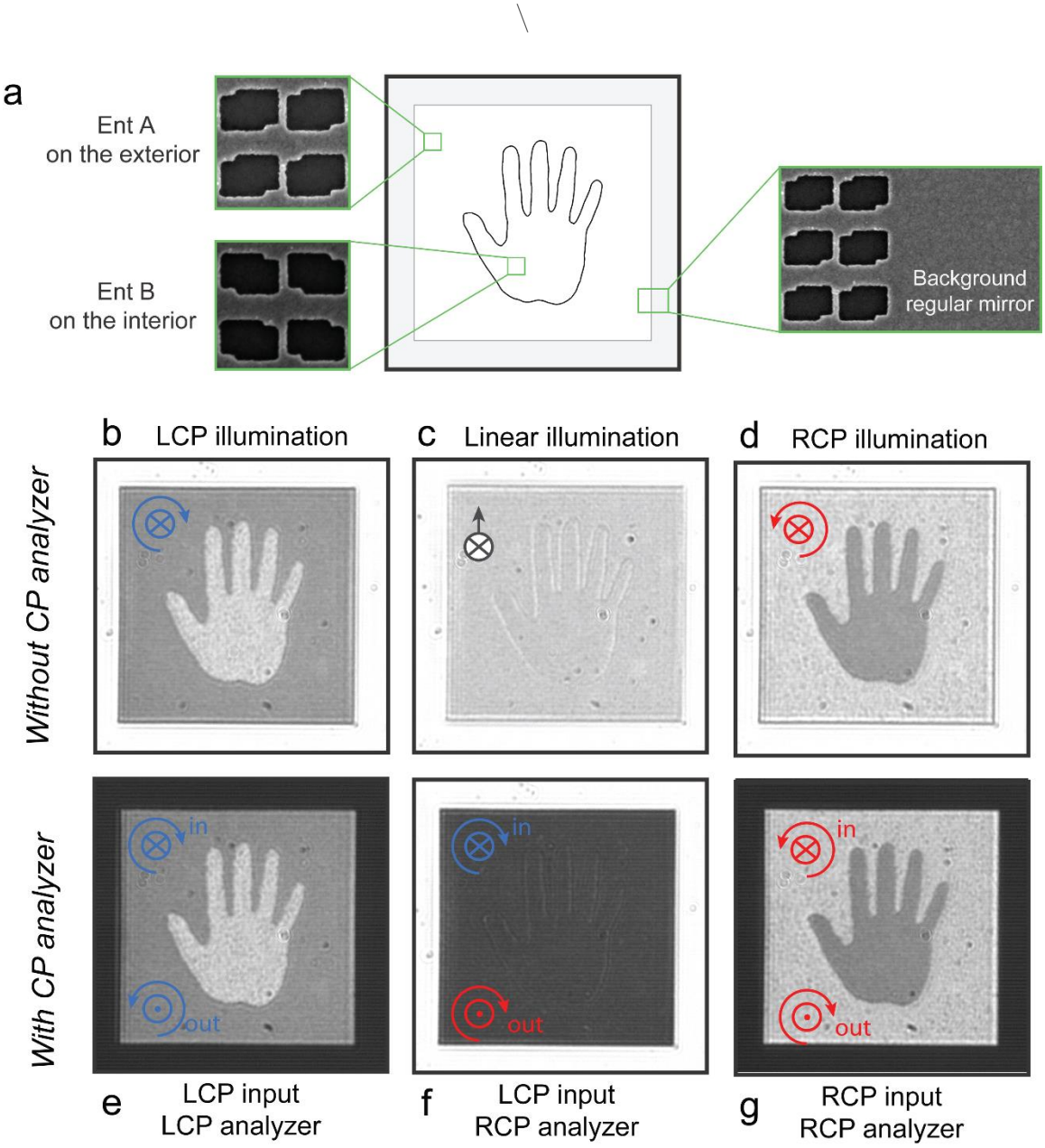

Figure 6.5: Visualization of the chiral selective absorption and the circular polarization preservation of the meta-mirrors. (a) Schematic of the created hand pattern. The exterior and interior regions of the hand are formed by enantiomer A and B, respectively. The metamaterial pattern is surrounded by unpatented metal,

serving as a regular mirror in the background. (b-d) Microscopic images of the fabricated metamaterials illuminated by LCP, linear/random polarized and RCP waves, respectively. (e-g) Corresponding images taken with a circular polarization analyzer, when the pattern is illuminated by both circular polarizations. In the case of RCP illumination with the LCP analyzer, an image identical to Figure 6.4(f) is produced.

6.4 Generating chiral-responsive nonlinear signals

Beyond the chiroptical response in the linear regime, the strong resonances including the handedness-sensitive field concentration observed in the meta-mirror is expected to significantly increase chiral-selective optical nonlinearity. Therefore, we have conducted nonlinear chiroptical measurements. In the experiment, we excite the meta-mirror samples of both enantiomers with a circularly polarized ultrafast laser and collect the generated nonlinear optical signals in the reflection direction. The corresponding nonlinear spectra when the metamaterial is pumped at a series of excitation wavelengths with a constant intensity are shown in Figure 6.5a,b. For most excitation wavelengths, a sharp peak can be identified in the generated nonlinear spectrum at the frequency-doubled wavelength. More importantly, this second harmonic generation (SHG) signal is closely dependent on

the spin state of the pump light and the enantiomeric properties of the meta-mirror. Furthermore, for excitation at shorter wavelengths (*e.g.* 740 nm), the SHG peak is accompanied by a broadband nonlinear spectrum that can be attributed to multi-photon luminescence[152].

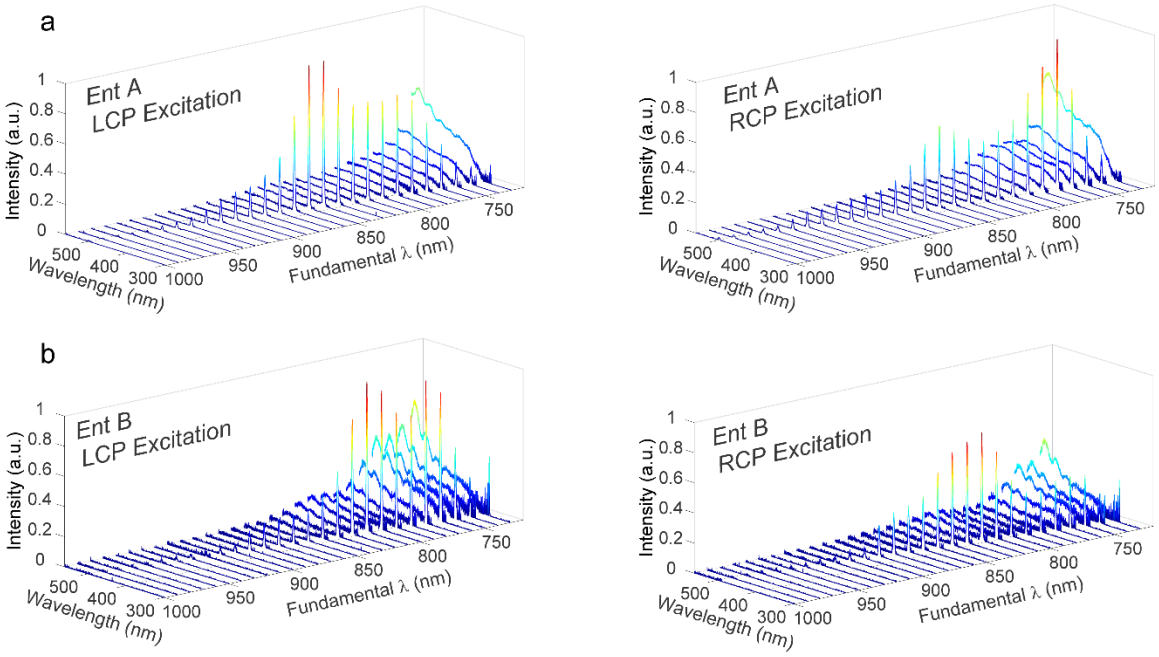

Figure 6.6: Chiral-selective nonlinear responses from both enantiomers. (a) Nonlinear spectra of enantiomer A under LCP and RCP excitations, respectively, at a series of excitation wavelengths of constant intensity. (b) Depictions of the counterparts for enantiomer B.

By integrating the signal in the frequency-doubled peaks of Figure 6.5a,b, we obtain the SHG excitation spectrum of both enantiomers pumped by circular

polarized waves, as shown in Figure 6.5c,d. The resonance behavior of the SHG efficiency in the meta-mirror is evident, recalling the linear chiroptical response shown in Figure 6.3. For instance, the SHG excitation spectrum of enantiomer A under LCP and RCP excitation peaks at a fundamental wavelength (λ_ω) around 770 nm and 850 nm, respectively, which is correlated to the linear reflection behavior shown in Figure 6.3a. Moreover, a SHG efficiency contrast larger than 3× (4×) is observed at λ_ω ~760 nm between RCP (LCP) and LCP (RCP) beams incident on enantiomer A (B). To better elucidate the chiral-selective nonlinearity of the meta-mirror, second harmonic generation circular dichroism (SHG-CD) is utilized to quantify the harmonic optical activity. Here SHG-CD is defined as $2(I_{2\omega}^{RCP} - I_{2\omega}^{LCP})/(I_{2\omega}^{RCP} + I_{2\omega}^{LCP})$, is plotted in Figure 6.5e for both enantiomers. A remarkably large harmonic optical activity is observed at the two resonances. In particular, a near unity SHG-CD value of enantiomer A is found at λ_ω around 770 nm, at where enantiomer B experiences a SHG-CD value of approximately –1, while, at λ_ω around 850 nm, enantiomer A and B have a SHG-CD value of roughly –0.5 and 1, respectively. These results reveal that second harmonic excitation can boost the contrast of nonlinear images[136], as seen in later experiments.

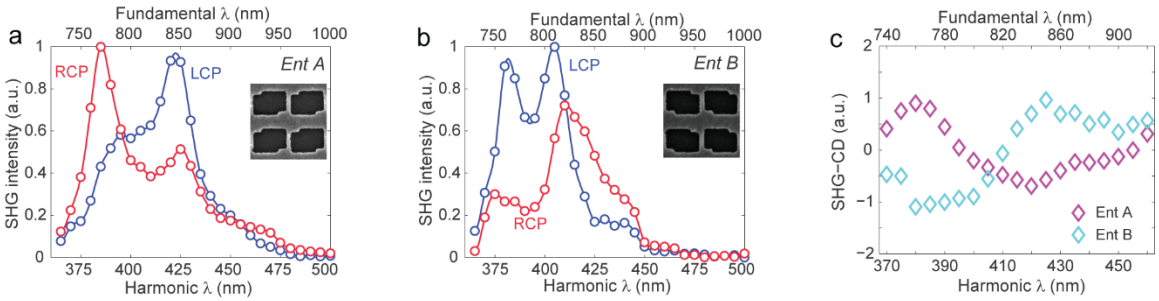

Figure 6.7: SHG excitation spectra for enantiomer (a) A and (b) B. The empty circles represent the measured results, and the solid curves serve to guide the eye. (c) Second-harmonic circular dichroism ($\mathrm{SHG-CD} = 2(I_{2\omega}^{\mathrm{RCP}} - I_{2\omega}^{\mathrm{LCP}})/(I_{2\omega}^{\mathrm{RCP}} + I_{2\omega}^{\mathrm{LCP}})$) of both enantiomers.

To investigate the potential of the meta-mirror for nonlinear imaging, we pump the patterned hand with a circularly polarized ultrafast wave at two fundamental wavelengths, *i.e.*, 770 nm and 850 nm, where the SHG-CD signal peaks and acquire the nonlinear images formed by the generated nonlinear signals. As illustrated in Figure 6.6a, a bright hand in a dark background is clearly observed in the second-harmonic image of the sample under a LCP excitation at $\lambda_\omega = 770$ nm, while Figure 6.6b indicates that the image brightness of the interior and exterior area of the hand reverses when the handedness of the excitation is switched to RCP. This observation is in accord with the chiral-selective SHG efficiency of the two enantiomers illustrated in Figure 6.5c,d. Importantly, compared with the linear images shown in Figure 6.4, a dramatically improved contrast is identified

from these SHG images. Moreover, the unpatterned section surrounding the metamaterial area is invariably dark due to the much lower SHG efficiency of the flat surface. By implementing a point-by-point calculation of the SHG-CD with photon counts recovered from both Figure 6.6a and Figure 6.6b, we obtain the corresponding SHG-CD image of the metamaterial pattern, as shown in Figure 6.6c. It can be seen that, owing to the enantioselectivity of the SHG signal generated from the metamaterial pattern, the SHG-CD image provides significantly improved contrast compared to those seen in Figure 6a,b. In addition, the SHG images of the sample pumped by a circularly polarized wave at $\lambda_\omega = 850$ nm are depicted in Figure 6.6d,e. A dark (bright) hand can be recognized from the bright (dark) background when excited by LCP (RCP) laser light, although the overall moderate contrast of the two images is constrained by the SHG efficiency at $\lambda_\omega =$ 850 nm. Nevertheless, the corresponding SHG-CD image shown in Figure 6.6f presents well-resolved details of the metamaterial pattern, which again clearly demonstrates the ability provided by the SHG-CD equation in visualizing the chirality of the metamaterial nanostructures. We notice that a round-shaped dark area is observed in Figure 6.6c. This is attributed to the signal of the fundamental beam reflected by the regular mirror area that was not completely eliminated by the short-pass filter implemented. Nevertheless, possessing a value of SHG-CD

close to zero, it has less influence on the visibility and contrast of the pattern's SHG-CD image. No such round dark area is found in Figure 6f, because of the much lower transmission rate of the filter at $\lambda_\omega = 850$ nm.

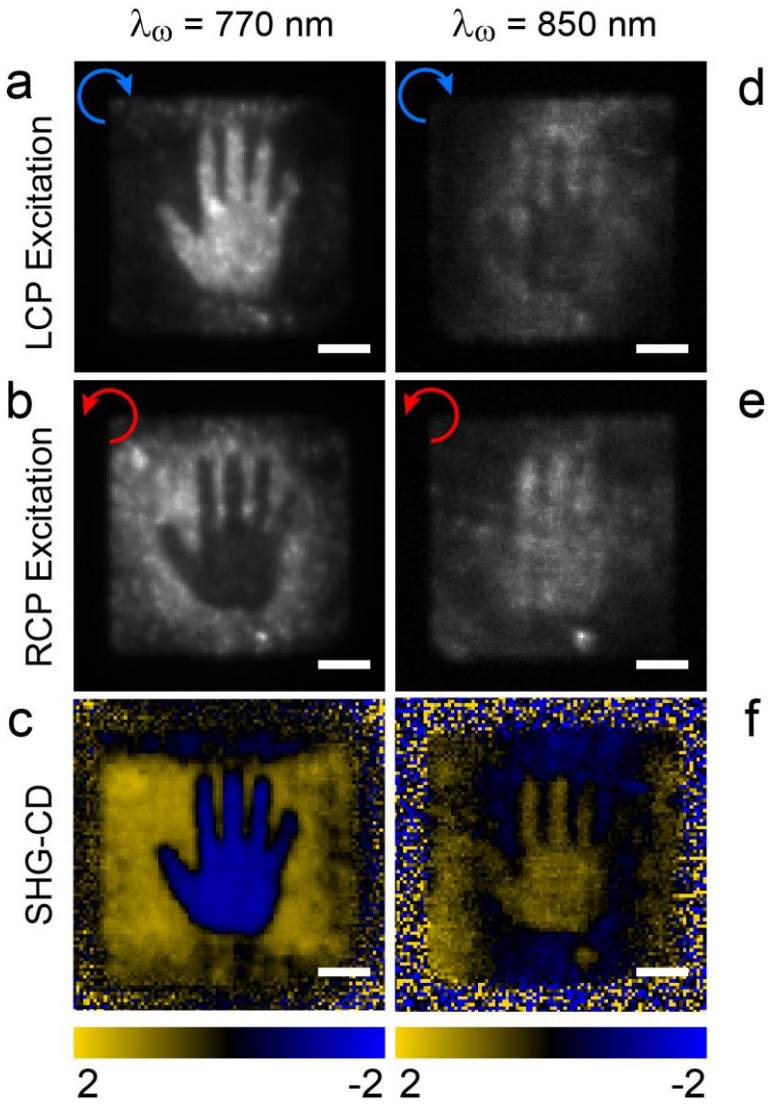

Figure 6.8: Nonlinear imaging of the chiral meta-mirror. (a) & (b) Nonlinear images of the hand pattern under LCP and RCP excitation, respectively, at a fundamental wavelength of 770 nm. (c) SHG-CD image obtained from Figure

6.6a,b. (d) & (e) Nonlinear images of the pattern under circularly polarized excitation at 850 nm. (f) The corresponding SHG-CD image is obtained from Figure 6.6(d) and (e). The scale bars represent 20 µm.

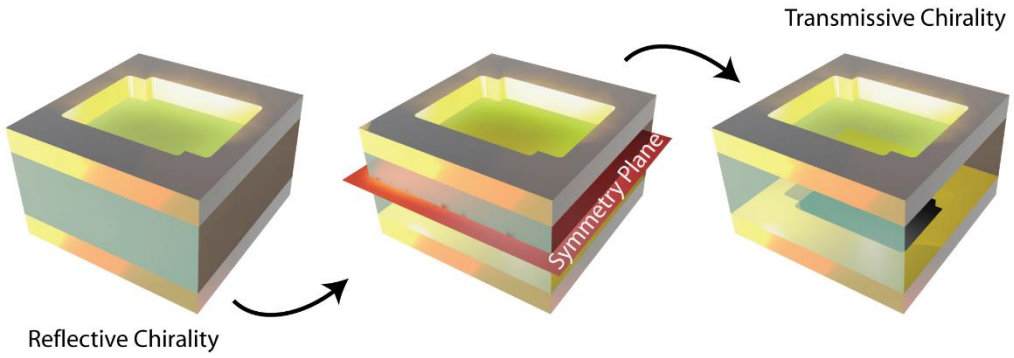

Figure 6.9: Creating a chiral mirror from a 3D chiral metamaterial.

The design of the chiral meta-mirror does not deviate much from the original chiral structures presented in earlier chapters. As seen in Figure 6.9, our highly chiral, transmissive metamaterial utilize two layers to achieve a high degree of chirality. If we then divide the structure by two and replace the lower layer with a reflective surface, we have utilized a single patterned layer to sculpt the electric field as though it were passing through a 3D structure.

In conclusion, we have designed and fabricated a metamaterial-based chiral mirror with giant chiroptical responses in both the linear and nonlinear regimes. Compared with regular (*e.g.* metallic) mirrors, there are two prominent features of the meta-mirror that have been identified, namely the strong chiral-selective

absorption and the handedness-preserved reflection from the surface. In addition, chiral resonance tailored nonlinear generation and second harmonic signal based imaging are observed in the meta-mirror under circularly polarized ultrafast excitations. Only requiring a single patterned layer, our design is more fabrication-friendly as compared with many of the most efficient chiral metamaterials that require genuinely three-dimensional building blocks. Moreover, the unpatterned back plane may allow for easier integration of various constituent materials as the core of the three-layer metamaterial, which, along with the topologically continuous structures of the design, may enable chiroptical responses that can be purposely tuned by external stimuli, such as an electric field.

CHAPTER VII.

Conclusions and Outlook

Chiral structures architected on the nano-scale are the basis for the handedness-dependent optical phenomena derived in this thesis. Specifically the structures presented here are both asymmetric and three-dimensional. The lack of centrosymmetry present within these structures presented opportunities to instigate both wave mixing and self-focusing processes. The majority of the nonlinear, chiral responsive optical phenomena witnessed in this thesis took a spectroscopic form similar to that of the chiroptical responses witnessed in the linear regime. Nonlinear chiral responses offer the unique ability to take the existing contrast recognized in the linear domain and are able to enhance it significantly. Continued research may show that the nonlinear signals may offer contrast that exceeds those presented in the preceding chapters. These engineered chiral materials may offer potential applications for molecular sensing, realizing unique chiral enabled properties like negative refraction, enhanced self-limiting processes, or non-reciprocal interactions. The following sections will briefly highlight the themes presented in each of the preceding chapters.

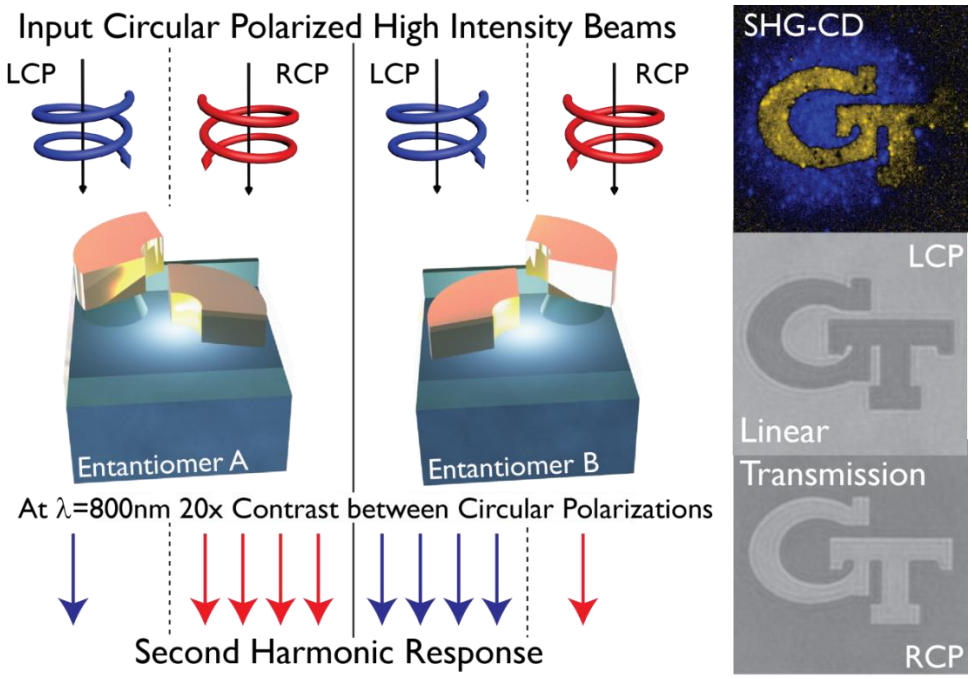

Figure 7.1: An overview detailing the enhanced contrast from nonlinear responses of a pair of chiral nanoarc metamaterials. When right circularly polarized (RCP) light is incident on the metamaterial a second harmonic response is generated that is 20x that of the LCP. Complementarily, enantiomer B produces a strong response for the opposite circular polarization. The same two enantiomers make up an array of a metamaterial structure, where the GT is filled with enantiomer B and the exterior enantiomer A. SHG-CD is the normalized circular dichroic contrast generated by the second harmonic signal.

Chapter 3 sought to increase the circular dichroic contrast of two circular polarizations in the visible regime and further explore the nonlinear responses that arose from these structures. A brief overview of what was achieved in chapter 3 is presented in Figure 7.1. The second harmonic signal produced immense contrast

between the two circular polarizations at the metamaterials resonant wavelength of 800 nm. This enormous contrast, roughly 20x, can be seen in the imaging demonstration, where the light emitted from one enantiomer under RCP illumination is nearly zero compared to the brightness of the other enantiomer. As we move away from the resonant wavelength the contrast fades off. At times, the nonlinear response incurs a slight broadening and shift compared to that of the linear transmittance. This effect can be witnessed in the second harmonic response as dampening of the incident light in the metamaterial structure can occur, thereby shifting the frequency when the signal transitions to its second harmonic.[103]

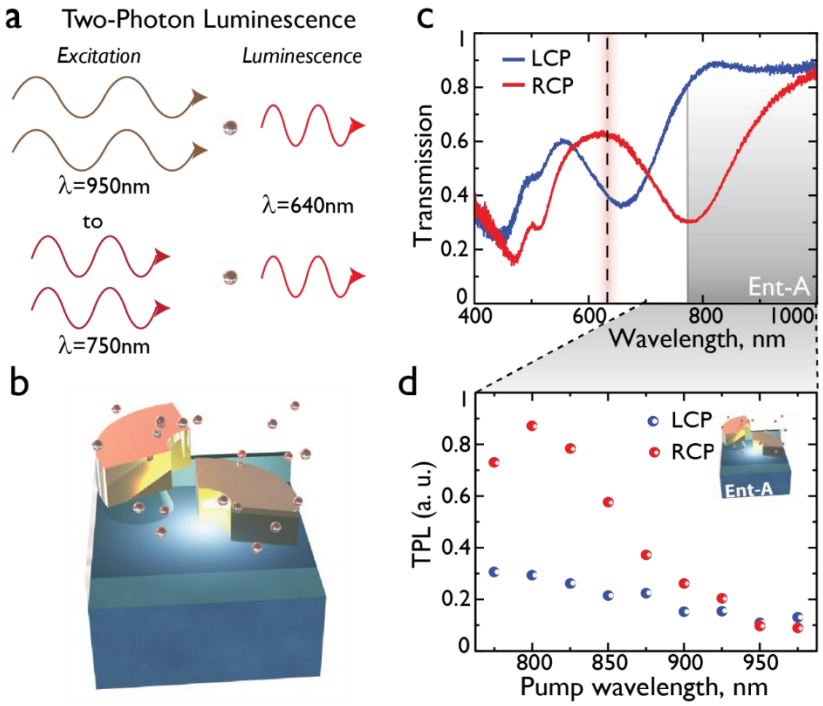

Figure 7.2: Scheme for extracting circular dichroic response via a luminescent signal. (a) Wavelengths distributed between 750 and 950 nm are incident on a set of quantum dots. The high intensity beam causes the QD's to absorb two photons at this long wavelength and luminesce at its emission wavelength of 640 nm. This is a well-known process known as two-photon luminescence. (b) The QDs are injected into the chiral hot spots of the chiral nanoarcs. (c) The chiral metamaterial has a large circular dichroic response at 640 nm, where CD is the difference between transmission of left and right circularly polarized beams. (d) The enhanced signal contrast generated from the quantum dots embedded in the chiral metamaterial structure.

Chapter 4 sought to access the chiral hotspots of our twisted arc metamaterial to produce enhanced, nonlinear responses from an achiral emitter. A brief overview of what was achieved in chapter 4 is presented in Figure 7.2. In the linear regime, the contrast between the circular polarizations is roughly 3x. Then, when exciting the quantum dots with a femtosecond pulsed laser we were able to instigate a nonlinear wave mixing process known as two-photon luminescence (TPL). When comparing the TPL from the chiral arcs compared to that of the TPL from the quantum dots on a bare substrate, the TPL signal was enhanced up to 44x at the resonant wavelength of the chiral arcs. Moreover, the chiral-selective behavior witnessed in the linear regime was carried over to that of the nonlinear regime. This experiment demonstrated that the overall chiral-selective behavior of a chiral metamaterial could be recovered from the emission of an achiral-emitter

placed in the vicinity of the hot spots of the structure. This further emphasizes that chiral metamaterials have a strong veracity for applications in the sensing field. We hope that this work pushes forward this realization of using chiral metamaterials for sensing purposes. However, these materials also hold potential for applications in optical signaling or detection devices for communications, characterization techniques, and optical components as well.

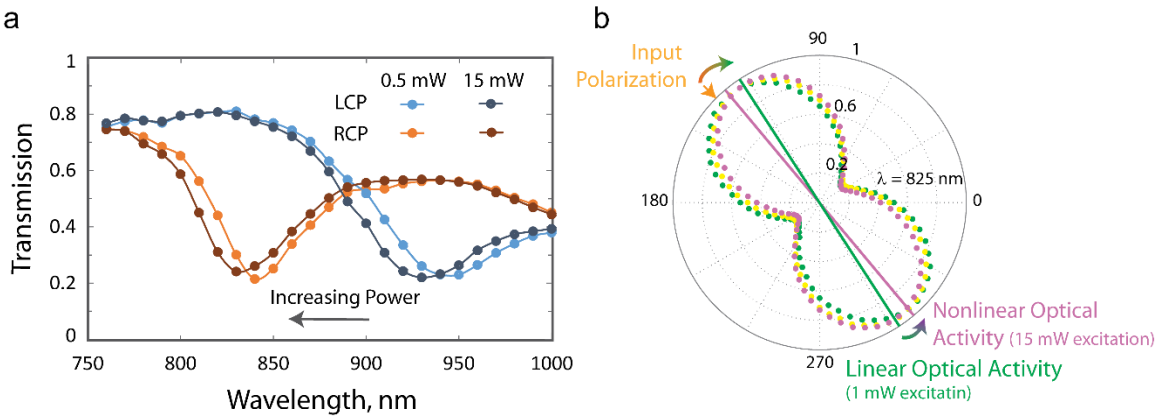

Figure 7.3: Overview of nonlinear optical activity. (a) Change in transmission through the chiral metamaterial as power is increased from 0.5 mW to 15 mW. (b) Depiction of nonlinear optical activity. The input polarization is at 135°. The light rotates 13° clockwise upon transmission through the metamaterial. Upon excitation with a 15 mW average power, femtosecond pulsed laser source the transmitted optical wave experiences a rotation of 12° counter-clockwise towards the input polarization.

Chapter 5 presented a second form of a chiral metamaterial that exhibits strong chiroptical responses in both the linear and nonlinear regimes. A brief overview of what was achieved in chapter 5 is presented in Figure 7.3. The metamaterial bares a circular dichroic response of 0.58 and a maximum optical rotation of 2.3×10^{6} ° cm^{-1}. In the nonlinear regime, we show a spectral blue-shift of 10 nm over the entire resonance spectrum of our chiral metamaterial in response to a power change of 15 mW. This phenomenon is most likely attributed to thermal self-action of the metamaterial. To better understand these effects, a detailed theoretical analysis that is beyond the scope of this work would be desired. A change in optical rotation of 1.76×10^{2} ° cm W^{-1} is achieved when the incident power is increased from 1 mW to 15 mW. To the best of our knowledge, no other material has demonstrated such a strong nonlinear chiroptical effect. Other materials in the literature and their polarization rotation per unit of optical intensity: $LiIO_3$ 10^{-11} ° cm W^{-1};[115] α-pinene $\leq10^{-11}$ ° cm W^{-1};[121] sucrose 2×10^{-11} ° cm W^{-1};[118, 121] an anisotropic metamaterial 3×10^{-4} ° cm W^{-1}.[65] To this extent, we believe that nonlinear optical activity can be useful in the development of optical modulation with chiral structures for applications in nanophotonic devices for optical switching and communications.

There is potential to see whether the aforementioned results might be due to thermal or electronic characteristics at high beam irradiance. In this respect, temporal measurements under circular polarizations using a femtosecond pulsed laser at a low repetition rate of 1000 kHz could elucidate these mechanisms. The

low repetition rate would effectively reduce the temperature mechanisms. The above mentioned transitions may have potential to be induced by the optical Kerr effect which prompts an effective change in the refractive index at high intensities of the metallic structures. In order to test this possibility, terms within the third rank tensor of the electric susceptibility could be detected using beam deflection. Additionally, a Maker fringe set-up could be used to extract out $\chi^{(2)}$ terms of the chiral metamaterial, thus quantifying the second order terms that give rise to the structure's second order chirality. Finally, ceramic plasmonic structures offer the potential to test materials under much higher irradiance than silver nanomaterials. With this in mind, similar metamaterial structures fabricated from ceramic plasmonic materials such as TiN would be interesting to see if such a spectral-shift under large irradiance is present and what mechanisms might give rise to this phenomenon.

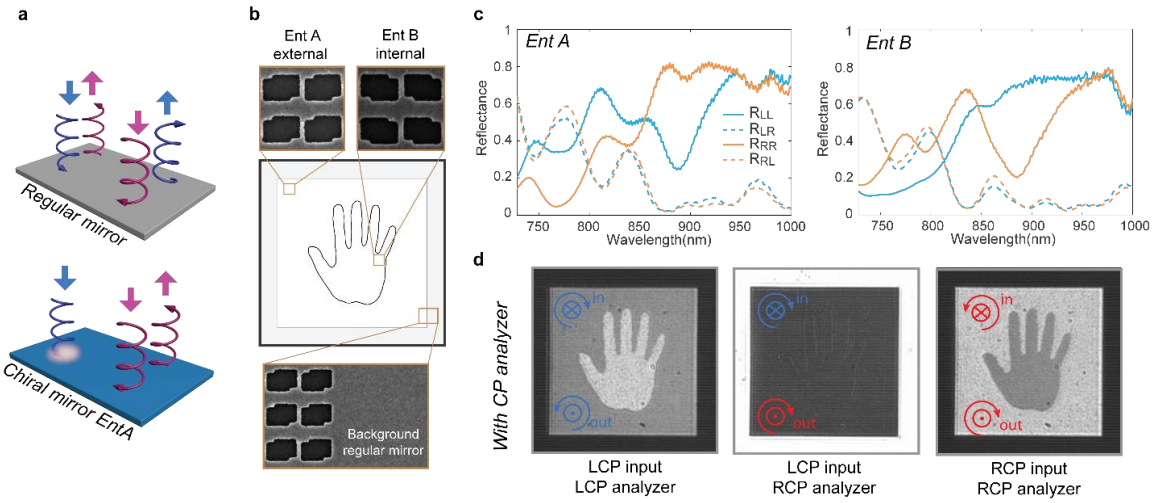

Figure 7.4: Chiral meta-mirror. (a) Schematic of how a conventional mirror interacts with circularly polarized light in comparison to the envision chiral meta-mirror. (b) Scanning-electron micrographs of the fabricated chiral mirror. Both enantiomer structures are utilized to pattern the shape of a hand, which is its geometrically chiral. (c) Decomposition of the reflected light from both stereoisomers of the meta-mirror. (d) Imaging of the patterned chiral meta-mirrors under circularly polarized illumination and circularly polarized analysis.

Chapter 6 demonstrated the design and fabrication of a metamaterial-based chiral mirror with giant chiroptical responses in both the linear and nonlinear regimes. A brief overview of what was achieved in chapter 6 is presented in Figure 7.4. Compared with regular (*e.g.* metallic) mirrors, there are two prominent features of the meta-mirror that have been identified, namely the strong chiral-selective absorption and the handedness-preserved reflection from the surface. In addition, chiral resonance tailored nonlinear generation and second harmonic signal based imaging are observed in the meta-mirror under circularly polarized ultrafast excitations. As this metamaterial only requires a single layer to be patterned, the design is more fabrication-friendly compared with most efficient chiral metamaterials that require three-dimensional building blocks. Moreover, the unpatterned back plane may allow for easier integration of various constituent materials as the core of the three-layer metamaterial, which, along with the

topologically continuous structures of the design, may enable chiroptical responses that can be purposely tuned by external stimuli, such as an electric field.

While this thesis was being developed, an enormous of breakthroughs were being achieved in the realms of big data (data science), machine learning, and augmented and virtual reality. As such, in order to advance the field of materials, the Air Force Research Labs was interested in pursuing data science applied research in the field of optical metamaterials. As such, I have worked on several projects related to data science applications in chiral metamaterials, and the simulation of an Ising model using both a generative adversarial network (GAN) and a deep convolutional network.[153]

Alternative Chiroptical Measurements

The future of this research will look to utilize secondary methods to measure chirality through well-established topics such as Rayleigh optical activity, which utilizes the scattered light to measure chirality. With this technique susceptibility tensor components can be measured. Other techniques that might be useful in extracting chiral information include circularly polarized luminescence (CPL) and fluorescence detected spectroscopy (FDCD). While CPL describes chirality as experienced in the excited state, FDCD describes chirality as experienced in the ground state.[154] The technique is useful in the description of chirality as it provides a secondary method of extracting information. These techniques provide similar information to circular dichroism and optical rotation but provide a

different method to extract the information, which could be crucial to unlocking future applications of hybrid metamaterials.

Handedness-selective directionality

To a similar effect, the field of chiral quantum optics has been growing over the past several years. On a simplistic level, as described by Lodahl et. al., chirality offers a non-reciprocal opportunity to control the emission of light from quantum emitters. The systems described by Lodahl are non-reciprocal in that, "forward- and backward-propagating photons interact differently with the emitter," to an extreme case in that the emission and or absorption is unidirectional.[155] In these systems, the coupling of light is dependent on the polarization of the input light and the polarization-dependent transition of the dipole moment of the emitter. Similar spin-selective effects have been recognized in thin films of TMD's.[156, 157]

Diverging slightly from this field of study we could look to Thomas Zentgraf at the University of Paderborn, Shuang Zhang's research at the University of Birmingham, and Xianzhong Chen at Heriot-Watt University, where chiral metasurfaces are used to produce holographic images that transmit different images.[158, 159] This is known as polarization resolved-multiplexing. These materials have similar polarization-dependent coupling interactions that have also been used for optical memory systems in the early 1970's. If we look to the Faraon group at the California Institute of Technology, they have produced similar effects using angle-resolved multiplexing.[160]

Active & Switchable Metamaterials

Chirality by nature is Boolean and causes an instinctive desire to try and create a single metamaterial structure that could provide bother enantiomeric responses. In this case, using only a single circular polarization as incidence, but creating a different response based on the material properties. However, optical activity tends to stem from the configurational structure of that material. For this reason, in order to generate an optically active signal from a structure, the structure should be engineered such that it has a mirror image that cannot be superposed onto itself. To this end, the structure must be reconfigurable or utilize a property that would disengage the resonance of the structure. To achieve this there exist opportunities to utilize semiconductor materials that provide active gain and thereby modify their refractive index.[161-163] Other opportunities could actively modulate the refractive index via hot-electron dynamics, with practical applications in ultra-fast dynamics.[164]

Active or switchable metamaterials can also be achieved by tuning the optical response through a nonlinear optical process. The literature since the early 1960's has found methods to induce second-harmonic generation via a four wave mixing process known as Electric-Field Induced Second Harmonic Generation (EFISH).[165] Since this demonstration, metamaterials have offered a novel route to provide this EFISH signal by providing electrical connections to these nano-composites.[166-169] In addition, these structures provide an opportune location to apply an enormous capacitance across dielectric gaps only 10's of nanometers in

thickness. However, EFISH is not the only opportunity to realize nonlinear optical processes that allow for the optoelectronic functionality. Other processes known as photon-dragging,[125] and the plasmoelectric potential effect,[170] and optical rectification[166] have been demonstrated in metamaterial devices.

All-Dielectric Metasurfaces

All-dielectric metamaterials have demonstrated the potential to create resonant responses without the need of noble metals and therefore plasmonic coupling. While some chiral metamaterials like the chiral nanoarcs presented previously, heavily rely on a magnetic resonance in order to produce a dip in the transmission spectra, the opportunity still exists in alternative dielectric materials to utilize these and other methods to induce these handedness-dependent responses. All dielectric metamaterials have been utilized for three dimensional topological insulators,[171] metasurfaces for polarization control,[172] and ultrafast all-optical tuning.[173] The internal mechanism in the majority of these devices is based on Mie scattering, in comparison to metamaterials composed of noble metals with large free electron deposits. Employing the Mie scatting of artificial dielectric metamaterials, both electronic and magnetic chiral dipole moments may be employed to instigate both linear and nonlinear optical phenomena in chiral metamaterials.

REFERENCES

[1] W. Cai, V. Shalaev, *Optical Metamaterials Fundamentals and Applications*, Springer Science Business Media LLC, New York, NY 2010.

[2] N. I. Zheludev, "The road ahead for metamaterials," *Science*, 328, 582-583 (2010).

[3] S. P. Rodrigues, S. Lan, L. Kang, Y. Cui, W. Cai, "Nonlinear imaging and spectroscopy of chiral metamaterials," *Adv. Mater*, 26, 6157-6162 (2014).

[4] S. P. Rodrigues, Y. Cui, S. Lan, L. Kang, W. Cai, "Metamaterials enable chiral-selective enhancement of two-photon luminescence from quantum emitters," *Adv. Mater*, 27, 1124-1130 (2015).

[5] S. P. Rodrigues, S. Lan, L. Kang, Y. Cui, P. W. Panuski, S. Wang, A. M. Urbas, W. Cai, "Intensity-dependent modulation of optically active signals in a chiral metamaterial," *Nat. Commun.*, 8, 14602 (2017).

[6] L. Kang, S. P. Rodrigues, M. Taghinejad, S. Lan, K. T. Lee, Y. M. Liu, D. H. Werner, A. Urbas, W. Cai, "Preserving spin states upon reflection: linear and nonlinear responses of a chiral meta-mirror," *Nano Lett.*, 17, 7102-7109 (2017).

[7] L. Barron, *Molecular Light Scattering and Optical Activity*, 2nd ed, Cambridge, 2004.

[8] K. P. C. Vollhardt, N. E. Schore, *Organic Chemistry : Structure and Function*, W.H. Freeman & Company, New York, N.Y. 2014.

[9] N. Berova, K. O. Nakanishi, R. Woody, *Circular Dichroism: Principles and Applications*, Wiley-VCH, New York 2000.

[10] E. Hendry, T. Carpy, J. Johnston, M. Popland, R. V. Mikhaylovskiy, A. J. Lapthorn, S. M. Kelly, L. D. Barron, N. Gadegaard, M. Kadodwala, "Ultrasensitive detection and characterization of biomolecules using superchiral fields," *Nat. Nanotechnol.*, 5, 783-787 (2010).

[11] S. Sioncke, T. Verbiest, A. Persoons, "Second-order nonlinear optical properties of chiral materials," *Mat. Sci. Eng. R*, 42, 115-155 (2003).

[12] J. C. Sutherland, in *Comprehensive Chiroptical Spectroscopy*, 2012.

[13] D. H. Goldstein, "Polarization properties of Scarabaeidae," *Appl Optics*, 45, 7944-7950 (2006).

[14] E. Libby, D. E. Azofeifa, M. Hernandez-Jimenez, C. Barboza-Aguilar, A. Solis, I. Garcia-Aguilar, L. Arce-Marenco, A. Hernandez, W. E. Vargas, "Light reflection by the cuticle of C. aurigans scarabs: a biological broadband reflector of left handed circularly polarized light," *J. Optics-UK*, 16, (2014).

[15] V. Sharma, M. Crne, J. O. Park, M. Srinivasarao, "Structural origin of circularly polarized iridescence in jeweled beetles," *Science*, 325, 449-451 (2009).

[16] H. Lee, M. J. Huttunen, K. J. Hsu, M. Partanen, G. Y. Zhuo, M. Kauranen, S. W. Chu, "Chiral imaging of collagen by second-harmonic generation circular dichroism," *Biomed. Opt. Express*, 4, 909-916 (2013).

[17] T. Verbiest, M. Kauranen, A. Persoons, M. Ikonen, J. Kurkela, H. Lemmetyinen, "Nonlinear-optical activity and biomolecular chirality," *J. Am. Chem. Soc.*, 116, 9203-9205 (1994).

[18] P. J. Campagnola, M. D. Wei, A. Lewis, L. M. Loew, "High-resolution nonlinear optical imaging of live cells by second harmonic generation," *Biophys. J.*, 77, 3341-3349 (1999).

[19] M. A. Belkin, Y. R. Shen, "Non-linear optical spectroscopy as a novel probe for molecular chirality," *Int. Rev. Phys. Chem.*, 24, 257-299 (2005).

[20] T. Petrallimallow, T. M. Wong, J. D. Byers, H. I. Yee, J. M. Hicks, "Circular-dichroism spectroscopy at interfaces - a surface 2nd harmonic-generation study," *J. Phys. Chem-US*, 97, 1383-1388 (1993).

[21] J. D. Byers, H. I. Yee, T. Petrallimallow, J. M. Hicks, "2nd-Harmonic generation circular-dichroism spectroscopy from chiral monolayers," *Phys. Rev. B*, 49, 14643-14647 (1994).

[22] P. Fischer, F. Hache, "Nonlinear optical spectroscopy of chiral molecules," *Chirality*, 17, 421-437 (2005).

[23] E. Plum, V. A. Fedotov, A. S. Schwanecke, N. I. Zheludev, Y. Chen, "Giant optical gyrotropy due to electromagnetic coupling," *Appl. Phys. Lett.*, 90, 223113 (2007).

[24] X. Yin, M. Schaferling, B. Metzger, H. Giessen, "Interpreting chiral nanophotonic spectra: the plasmonic born-kuhn model," *Nano Lett.*, 13, 6238-6243 (2013).

[25] M. Hentschel, M. Schaferling, T. Weiss, N. Liu, H. Giessen, "Three-dimensional chiral plasmonic oligomers," *Nano Lett.*, 12, 2542-2547 (2012).

[26] C. Helgert, E. Pshenay-Severin, M. Falkner, C. Menzel, C. Rockstuhl, E. B. Kley, A. Tunnermann, F. Lederer, T. Pertsch, "Chiral metamaterial composed of three-dimensional plasmonic nanostructures," *Nano Lett.*, 11, 4400-4404 (2011).

[27] M. Decker, S. Linden, M. Wegener, "Coupling effects in low-symmetry planar split-ring resonator arrays," *Opt. Lett.*, 34, 1579-1581 (2009).

[28] Y. Zhao, M. A. Belkin, A. Alu, "Twisted optical metamaterials for planarized ultrathin broadband circular polarizers," *Nat. Commun.*, 3, 870 (2012).

[29] V. K. Valev, J. J. Baumberg, C. Sibilia, T. Verbiest, "Chirality and chiroptical effects in plasmonic nanostructures: fundamentals, recent progress, and outlook," *Adv. Mater.*, 25, 2517-2534 (2013).

[30] C. M. Soukoulis, M. Wegener, "Past achievements and future challenges in the development of three-dimensional photonic metamaterials," *Nat. Photonics*, 5, 523-530 (2011).

[31] Z. Li, M. Gokkavas, E. Ozbay, "Manipulation of asymmetric transmission in planar chiral nanostructures by anisotropic loss," *Adv. Opt. Mater.*, 1, 608-608 (2013).

[32] W. S. Gao, H. M. Leung, Y. H. Li, H. Chen, W. Y. Tam, "Circular dichroism in double-layer metallic crossed-gratings," *J. Optics-UK*, 13, (2011).

[33] J. B. Pendry, "A chiral route to negative refraction," *Science*, 306, 1353-1355 (2004).

[34] S. Zhang, Y. S. Park, J. S. Li, X. C. Lu, W. L. Zhang, X. Zhang, "Negative refractive index in chiral metamaterials," *Phys. Rev. Lett.*, 102, 023901 (2009).

[35] J. K. Gansel, M. Thiel, M. S. Rill, M. Decker, K. Bade, V. Saile, G. von Freymann, S. Linden, M. Wegener, "Gold helix photonic metamaterial as broadband circular polarizer," *Science*, 325, 1513-1515 (2009).

[36] M. D. Turner, M. Saba, Q. M. Zhang, B. P. Cumming, G. E. Schroder-Turk, M. Gu, "Miniature chiral beamsplitter based on gyroid photonic crystals," *Nat. Photonics*, 7, 801-805 (2013).

[37] B. Wang, J. Zhou, T. Koschny, M. Kafesaki, C. M. Soukoulis, "Chiral metamaterials: simulations and experiments," *J. Opt. A-Pure Appl. Op.*, 11, (2009).

[38] S. Zhang, J. Zhou, Y. S. Park, J. Rho, R. Singh, S. Nam, A. K. Azad, H. T. Chen, X. B. Yin, A. J. Taylor, X. Zhang, "Photoinduced handedness switching in terahertz chiral metamolecules," *Nat. Commun.*, 3, 942 (2012).

[39] Y. Z. He, G. K. Larsen, W. Ingram, Y. P. Zhao, "Tunable three-dimensional helically stacked plasmonic layers on nanosphere monolayers," *Nano Lett.*, 14, 1976-1981 (2014).

[40] M. Decker, R. Zhao, C. M. Soukoulis, S. Linden, M. Wegener, "Twisted split-ring-resonator photonic metamaterial with huge optical activity," *Opt. Lett.*, 35, 1593-1595 (2010).

[41] M. Decker, M. Ruther, C. E. Kriegler, J. Zhou, C. M. Soukoulis, S. Linden, M. Wegener, "Strong optical activity from twisted-cross photonic metamaterials," *Opt. Lett.*, 34, 2501-2503 (2009).

[42] S. Vignolini, N. A. Yufa, P. S. Cunha, S. Guldin, I. Rushkin, M. Stefik, K. Hur, U. Wiesner, J. J. Baumberg, U. Steiner, "A 3D optical metamaterial made by self-assembly," *Adv. Mater.*, 24, 23-27 (2012).

[43] E. Plum, V. A. Fedotov, N. I. Zheludev, "Optical activity in extrinsically chiral metamaterial," *Appl. Phys. Lett.*, 93, 191911 (2008).

[44] V. A. Fedotov, P. L. Mladyonov, S. L. Prosvirnin, A. V. Rogacheva, Y. Chen, N. I. Zheludev, "Asymmetric propagation of electromagnetic waves through a planar chiral structure," *Phys. Rev. Lett.*, 97, 167401 (2006).

[45] S. V. Zhukovsky, C. Kremers, D. N. Chigrin, "Plasmonic rod dimers as elementary planar chiral meta-atoms," *Opt. Lett*, 36, 2278-2280 (2011).

[46] M. J. Huttunen, G. Bautista, M. Decker, S. Linden, M. Wegener, M. Kauranen, "Nonlinear chiral imaging of subwavelength-sized twisted-cross gold nanodimers [Invited]," *Opt. Mater. Express*, 1, 46-56 (2011).

[47] Y. Cui, L. Kang, S. Lan, S. P. Rodrigues, W. Cai, "Giant chiral optical response from a twisted-arc metamaterial," *Nano Lett.*, 14, 1021-1025 (2014).

[48] A. V. Rogacheva, V. A. Fedotov, A. S. Schwanecke, N. I. Zheludev, "Giant gyrotropy due to electromagnetic-field coupling in a bilayered chiral structure," *Phys. Rev. Lett.*, 97, 177401 (2006).

[49] R. A. Shelby, D. R. Smith, S. Schultz, "Experimental verification of a negative index of refraction," *Science*, 292, 77-79 (2001).

[50] M. Decker, M. W. Klein, M. Wegener, S. Linden, "Circular dichroism of planar chiral magnetic metamaterials," *Opt. Lett.*, 32, 856-858 (2007).

[51] J. F. Zhou, J. F. Dong, B. N. Wang, T. Koschny, M. Kafesaki, C. M. Soukoulis, "Negative refractive index due to chirality," *Phys. Rev. B*, 79, 121104 (2009).

[52] S. Lan, S. P. Rodrigues, L. Kang, W. Cai, "Visualizing Optical Phase Anisotropy in Black Phosphorus," *ACS Photonics*, 3, 1176-1181 (2016).

[53] V. K. Valev, X. Zheng, C. G. Biris, A. V. Silhanek, V. Volskiy, B. De Clercq, O. A. Aktsipetrov, M. Ameloot, N. C. Panoiu, G. A. E. Vandenbosch, V. V. Moshchalkov, "The origin of second harmonic generation hotspots in chiral optical metamaterials [Invited]," *Opt. Mater. Express*, 1, 36-45 (2011).

[54] M. Schaferling, X. H. Yin, H. Giessen, "Formation of chiral fields in a symmetric environment," *Opt. Express*, 20, 26326-26336 (2012).

[55] V. K. Valev, N. Smisdom, A. V. Silhanek, B. De Clercq, W. Gillijns, M. Ameloot, V. V. Moshchalkov, T. Verbiest, "Plasmonic ratchet wheels: wwitching circular dichroism by arranging chiral nanostructures," *Nano Lett.*, 9, 3945-3948 (2009).

[56] J. Dong, J. Zhou, T. Koschny, C. Soukoulis, "Bi-layer cross chiral structure with strong optical activity and negative refractive index," *Opt. Express*, 17, 14172-14179 (2009).

[57] G. K. Larsen, Y. Z. He, J. Wang, Y. P. Zhao, "Scalable fabrication of composite Ti/Ag plasmonic helices: controlling morphology and optical activity by tailoring material properties," *Adv. Opt. Mater.*, 2, 245-249 (2014).

[58] R. Schreiber, N. Luong, Z. Y. Fan, A. Kuzyk, P. C. Nickels, T. Zhang, D. M. Smith, B. Yurke, W. Kuang, A. O. Govorov, T. Liedl, "Chiral plasmonic DNA nanostructures with switchable circular dichroism," *Nat. Commun.*, 4, 2948 (2013).

[59] M. H. Li, L. Y. Guo, J. F. Dong, H. L. Yang, "An ultra-thin chiral metamaterial absorber with high selectivity for LCP and RCP waves," *J. Phys. D. Appl. Phys.*, 47, 185102 (2014).

[60] N. Y. Ha, Y. Ohtsuka, S. M. Jeong, S. Nishimura, G. Suzaki, Y. Takanishi, K. Ishikawa, H. Takezoe, "Fabrication of a simultaneous red-green-blue reflector using single-pitched cholesteric liquid crystals," *Nat. Mater.*, 7, 43-47 (2008).

[61] Y. Tang, A. E. Cohen, "Enhanced enantioselectivity in excitation of chiral molecules by superchiral light," *Science*, 332, 333-336 (2011).

[62] F. Neubrech, A. Pucci, T. W. Cornelius, S. Karim, A. Garcia-Etxarri, J. Aizpurua, "Resonant plasmonic and vibrational coupling in a tailored nanoantenna for infrared detection," *Phys. Rev. Lett.*, 101, 157403 (2008).

[63] I. Ament, J. Prasad, A. Henkel, S. Schmachtel, C. Sonnichsen, "Single unlabeled protein detection on individual plasmonic nanoparticles," *Nano Lett.*, 12, 1092-1095 (2012).

[64] V. G. Kravets, F. Schedin, R. Jalil, L. Britnell, R. V. Gorbachev, D. Ansell, B. Thackray, K. S. Novoselov, A. K. Geim, A. V. Kabashin, A. N. Grigorenko, "Singular phase nano-optics in plasmonic metamaterials for label-free single-molecule detection," *Nat. Mater.*, 12, 304-309 (2013).

[65] M. X. Ren, E. Plum, J. J. Xu, N. I. Zheludev, "Giant nonlinear optical activity in a plasmonic metamaterial," *Nat. Commun.*, 3, 833 (2012).

[66] B. E. A. Saleh, M. C. Teich, *Fundamentals of Photonics*, Wiley, Hoboken, N.J. 2007.

[67] R. W. Boyd, "Nonlinear Optics, 3rd Edition," *Nonlinear Optics, 3rd Edition*, 1-613 (2008).

[68] E. Efrati, W. T. M. Irvine, "Orientation-dependent handedness and chiral design," *Phys. Rev. X*, 4, 011003 (2014).

[69] V. K. Valev, A. V. Silhanek, N. Smisdom, B. De Clercq, W. Gillijns, O. A. Aktsipetrov, M. Ameloot, V. V. Moshchalkov, T. Verbiest, "Linearly polarized second harmonic generation microscopy reveals chirality," *Opt. Express*, 19, 9242-9244 (2011).

[70] E. A. Mamonov, T. V. Murzina, I. A. Kolmychek, A. I. Maydykovsky, V. K. Valev, A. V. Silhanek, T. Verbiest, V. V. Moshchalkov, O. A. Aktsipetrov, "Chirality in nonlinear-optical response of planar G-shaped nanostructures," *Opt. Express*, 20, 8518-8523 (2012).

[71] M. Kauranen, A. V. Zayats, "Nonlinear plasmonics," *Nat. Photonics*, 6, 737-748 (2012).

[72] G. A. Wurtz, R. Pollard, W. Hendren, G. P. Wiederrecht, D. J. Gosztola, V. A. Podolskiy, A. V. Zayats, "Designed ultrafast optical nonlinearity in a plasmonic nanorod metamaterial enhanced by nonlocality," *Nat. Nanotechnol.*, 6, 106-110 (2011).

[73] M. W. Klein, C. Enkrich, M. Wegener, S. Linden, "Second-harmonic generation from magnetic metamaterials," *Science*, 313, 502-504 (2006).

[74] S. Linden, F. B. P. Niesler, J. Forstner, Y. Grynko, T. Meier, M. Wegener, "Collective effects in second-harmonic generation from split-ring-resonator arrays," *Phys. Rev. Lett.*, 109, 015502 (2012).

[75] P. Fischer, A. D. Buckingham, A. C. Albrecht, "Isotropic second-order nonlinear optical susceptibilities," *Phys. Rev. A*, 64, 053816 (2001).

[76] P. Fischer, K. Beckwitt, F. W. Wise, A. C. Albrecht, "The chiral specificity of sum-frequency generation in solutions," *Chem. Phys. Lett.*, 352, 463-468 (2002).

[77] L. D. Barron, *Molecular light scattering and optical activity*, Cambridge University Press, Cambridge, UK ; New York 2004.

[78] L. M. Haupert, G. J. Simpson, "Chirality in nonlinear optics," *Annu. Rev. Phys. Chem.*, 60, 345-365 (2009).

[79] N. Ji, V. Ostroverkhov, M. Belkin, Y. J. Shiu, Y. R. Shen, "Toward chiral sum-frequency spectroscopy," *J. Am. Chem. Soc.*, 128, 8845-8848 (2006).

[80] X. Ma, C. Huang, M. Pu, C. Hu, Q. Feng, X. Luo, "Multi-band circular polarizer using planar spiral metamaterial structure," *Opt. Express*, 20, 16050-16058 (2012).

[81] A. K. Sarychev, V. M. Shalaev, "Electromagnetic field fluctuations and optical nonlinearities in metal-dielectric composites," *Phys. Rep.*, 335, 276-371 (2000).

[82] X. S. Xie, R. C. Dunn, "Probing single-molecule dynamics," *Science*, 265, 361-364 (1994).

[83] R. R. Chance, A. Prock, R. Silbey, in *Adv. Chem. Phys.*, Vol. 37, John Wiley & Sons, Inc., 2007, 1-65.

[84] C. Hoppener, Z. J. Lapin, P. Bharadwaj, L. Novotny, "Self-similar gold-nanoparticle antennas for a cascaded enhancement of the optical field," *Phys. Rev. Lett.*, 109, 017402 (2012).

[85] A. O. Govorov, Z. Y. Fan, P. Hernandez, J. M. Slocik, R. R. Naik, "Theory of circular dichroism of nanomaterials comprising chiral molecules and nanocrystals: plasmon enhancement, dipole interactions, and dielectric effects," *Nano Lett.*, 10, 1374-1382 (2010).

[86] T. Nakashima, Y. Kobayashi, T. Kawai, "Optical activity and chiral memory of thiol-capped cdte nanocrystals," *J. Am. Chem. Soc.*, 131, 10342-11343 (2009).

[87] S. D. Elliott, M. P. Moloney, Y. K. Gun'ko, "Chiral shells and achiral cores in CdS quantum dots," *Nano Lett.*, 8, 2452-2457 (2008).

[88] S. C. Pu, M. J. Yang, C. C. Hsu, C. W. Lai, C. C. Hsieh, S. H. Lin, Y. M. Cheng, P. T. Chou, "The empirical correlation between size and two-photon absorption cross section of CdSe and CdTe quantum dots," *Small*, 2, 1308-1313 (2006).

[89] G. S. He, K. T. Yong, Q. D. Zheng, Y. Sahoo, A. Baev, A. I. Ryasnyanskiy, P. N. Prasad, "Multi-photon excitation properties of CdSe quantum dots solutions and optical limiting behavior in infrared range," *Opt. Express*, 15, 12818-12833 (2007).

[90] Y. Tang, L. Sun, A. E. Cohen, "Chiroptical hot spots in twisted nanowire plasmonic oscillators," *Appl. Phys. Lett.*, 102, 043103 (2013).

[91] N. Meinzer, E. Hendry, W. L. Barnes, "Probing the chiral nature of electromagnetic fields surrounding plasmonic nanostructures," *Phys. Rev. B*, 88, 041407 (2013).

[92] D. E. Chang, A. S. Sorensen, P. R. Hemmer, M. D. Lukin, "Strong coupling of single emitters to surface plasmons," *Phys. Rev. B*, 76, 035420 (2007).

[93] K. T. Shimizu, W. K. Woo, B. R. Fisher, H. J. Eisler, M. G. Bawendi, "Surface-enhanced emission from single semiconductor nanocrystals," *Phys. Rev. Lett.*, 89, 117401 (2002).

[94] S. Kuhn, U. Hakanson, L. Rogobete, V. Sandoghdar, "Enhancement of single-molecule fluorescence using a gold nanoparticle as an optical nanoantenna," *Phys. Rev. Lett.*, 97, 017402 (2006).

[95] L. Novotny, B. Hecht, *Principles of nano-optics*, Cambridge University Press, Cambridge 2012.

[96] J. N. Farahani, D. W. Pohl, H. J. Eisler, B. Hecht, "Single quantum dot coupled to a scanning optical antenna: A tunable superemitter," *Phys. Rev. Lett.*, 95, 017402 (2005).

[97] W. Kaiser, C. G. B. Garrett, "2-Photon excitation in $CaF_2 : Eu^{2+}$," *Phys. Rev. Lett.*, 7, 229-231 (1961).

[98] D. R. Larson, W. R. Zipfel, R. M. Williams, S. W. Clark, M. P. Bruchez, F. W. Wise, W. W. Webb, "Water-soluble quantum dots for multiphoton fluorescence imaging in vivo," *Science*, 300, 1434-1436 (2003).

[99] P. Bharadwaj, L. Novotny, "Robustness of quantum dot power-law blinking," *Nano Lett.*, 11, 2137-2141 (2011).

[100] G. T. Boyd, Z. H. Yu, Y. R. Shen, "Photoinduced luminescence from the noble metals and its enhancement on roughened surfaces," *Phys. Rev. B*, 33, 7923-7936 (1986).

[101] V. P. Drachev, E. N. Khaliullin, W. Kim, F. Alzoubi, S. G. Rautian, V. P. Safonov, R. L. Armstrong, V. M. Shalaev, "Quantum size effect in two-photon excited luminescence from silver nanoparticles," *Phys Rev B*, 69, 035318, (2004).

[102] J. Zuloaga, P. Nordlander, "On the energy shift between near-field and far-field peak intensities in localized plasmon systems," *Nano Lett.*, 11, 1280-1283 (2011).

[103] C. A. Emeis, L. J. Oosterhoff, G. Devries, "Numerical evaluation of kramers-kronig relations," *Proc. R. Soc. Lon. Ser.-A*, 297, 54-65 (1967).

[104] N. Liu, H. Liu, S. N. Zhu, H. Giessen, "Stereometamaterials," *Nat. Photonics*, 3, 157-162 (2009).

[105] K. Dietrich, D. Lehr, C. Helgert, A. Tunnermann, E. B. Kley, "Circular dichroism from chiral nanomaterial fabricated by on-edge lithography," *Adv. Mater.*, 24, 321-325 (2012).

[106] M. Thiel, J. Ott, A. Radke, J. Kaschke, M. Wegener, "Dip-in depletion optical lithography of three-dimensional chiral polarizers," *Opt. Lett.*, 38, 4252-4255 (2013).

[107] E. Plum, N. I. Zheludev, "Chiral mirrors," *Appl. Phys. Lett.*, 106, 221901 (2015).

[108] Y. Z. He, K. Lawrence, W. Ingram, Y. P. Zhao, "Strong local chiroptical response in racemic patchy silver films: enabling a large-area chiroptical device," *ACS Photonics*, 2, 1246-1252 (2015).

[109] S. I. Vavilov, "The microstructure of light (In Russian)," *USSR Academy of Sciences* (1950).

[110] S. Kielich, "Laser-induced nonlinear effects in optically active media," *IEEE J. Quantum Elect.*, Qe 4, 75-87 (1968).

[111] S. A. Akhmanov, V. I. Zharikov, "Nonlinear optics of gyrotropic media," *JETP Lett.-USSR*, 6, 137 (1967).

[112] D. V. Vlasov, V. P. Zaitsev, "Experimental observation of nonlinear optical activity," *JETP Lett.-USSR*, 14, 112 (1971).

[113] V. V. Borshch, M. P. Lisitsa, P. E. Mozol, I. V. Fekeshgazi, "Self-induced rotation of light polarization-plane in crystals of 422 symmetry class," *Kvantovaya Elektron*, 5, 672-675 (1978).

[114] S. A. Akhamanov, B. V. Zhdanov, N. I. Zheludev, N. I. Kovrigin, V. I. Kuznetsov, "Non-linear optical-activity in crystals," *JETP Lett.*, 29, 264-268 (1979).

[115] N. I. Zheludev, I. S. Ruddock, R. Illingworth, "Intensity dependence of thermal nonlinear optical-activity in crystals," *Appl. Phys. B-Photo*, 49, 65-67 (1989).

[116] I. C. Khoo, S. L. Zhuang, S. Shepard, "Self-focusing of a low-power cw laser-beam via optically induced birefringence in a nematic liquid-crystal film," *Appl. Phys. Lett.*, 39, 937-940 (1981).

[117] R. Cameron, G. C. Tabisz, "Observation of two-photon optical rotation by molecules," *Mol. Phys.*, 90, 159-164 (1997).

[118] H. Mesnil, F. Hache, "Experimental evidence of third-order nonlinear dichroism in a liquid of chiral molecules," *Phys. Rev. Lett.*, 85, 4257-4260 (2000).

[119] H. Mesnil, M. C. Schanne-Klein, F. Hache, M. Alexandre, G. Lemercier, C. Andraud, "Experimental observation of nonlinear circular dichroism in a pump-probe experiment," *Chem. Phys. Lett.*, 338, 269-276 (2001).

[120] P. P. Markowicz, M. Samoc, J. Cerne, P. N. Prasad, A. Pucci, G. Ruggeri, "Modified Z-scan techniques for investigations of nonlinear chiroptical effects," *Opt. Express*, 12, 5209-5214 (2004).

[121] X. Y. Chen, C. Raggio, P. J. Campagnola, "Second-harmonic generation circular dichroism studies of osteogenesis imperfecta," *Opt. Lett.*, 37, 3837-3839 (2012).

[122] A. Belardini, A. Benedetti, M. Centini, G. Leahu, F. Mura, S. Sennato, C. Sibilia, V. Robbiano, M. C. Giordano, C. Martella, D. Comoretto, F. B. de Mongeot, "Second harmonic generation circular dichroism from self-ordered hybrid plasmonic-photonic nanosurfaces," *Adv. Opt. Mater.*, 2, 208-213 (2014).

[123] V. K. Valev, J. J. Baumberg, B. De Clercq, N. Braz, X. Zheng, E. J. Osley, S. Vandendriessche, M. Hojeij, C. Blejean, J. Mertens, C. G. Biris, V. Volskiy, M. Ameloot, Y. Ekinci, G. A. E. Vandenbosch, P. A. Warburton, V. V. Moshchalkov, N. C. Panoiu, T. Verbiest, "Nonlinear superchiral meta-surfaces: tuning chirality and disentangling non-reciprocity at the nanoscale," *Adv. Mater.*, 26, 4074-4081 (2014).

[124] L. Kang, S. Lan, Y. Cui, S. P. Rodrigues, Y. Liu, D. H. Werner, W. Cai, "An active metamaterial platform for chiral responsive optoelectronics," *Adv. Mater.*, 27, 4377-4383 (2015).

[125] W. Li, Z. J. Coppens, L. V. Besteiro, W. Wang, A. O. Govorov, J. Valentine, "Circularly polarized light detection with hot electrons in chiral plasmonic metamaterials," *Nat. Commun.*, 6, 8379 (2015).

[126] A. Rose, D. A. Powell, I. V. Shadrivov, D. R. Smith, Y. S. Kivshar, "Circular dichroism of four-wave mixing in nonlinear metamaterials," *Phys. Rev. B*, 88, (2013).

[127] N. Berova, K. Nakanishi, R. W. Woody, *Circular Dichroism: Principles and Applications*, Wiley-VCH, New York 2000.

[128] J. C. Bose, "On the rotation of plane of polarization of electric waves by a twisted structure," *Proc. R. Soc. Lond.*, 63, 146-152 (1898).

[129] E. Plum, V. A. Fedotov, A. S. Schwanecke, N. I. Zheludev, Y. Chen, "Giant optical gyrotropy due to electromagnetic coupling," *Appl. Phys. Lett.*, 90, 223113 (2007).

[130] S. Zhang, Y. S. Park, J. S. Li, X. C. Lu, W. L. Zhang, X. Zhang, "Negative refractive index in chiral metamaterials," *Phys. Rev. Lett.*, 102, 023901 (2009).

[131] M. Hentschel, M. Schaferling, B. Metzger, H. Giessen, "Plasmonic diastereomers: adding up chiral centers," *Nano Lett.*, 13, 600-606 (2013).

[132] B. Frank, X. H. Yin, M. Schaferling, J. Zhao, S. M. Hein, P. V. Braun, H. Giessen, "Large-area 3D Chiral Plasmonic structures," *ACS Nano*, 7, 6321-6329 (2013).

[133] Z. Wang, F. Cheng, T. Winsor, Y. Liu, "Optical chiral metamaterials: a review of the fundamentals, fabrication methods and applications," *Nanotechnology*, 27, 412001 (2016).

[134] S. P. Rodrigues, Lan, S., Kang, L., Cui, Y., Panuski, P. W., Wang, S., Urbas, A. M., Cai, W., "Intensity-dependent modulation of optically active signals in a chiral metamaterial," *Nat. Commun.*, 8, 14602 (2017).

[135] M. Schäferling, Dregely, D., Hentschel, M., Giessen., H., "Tailoring enhanced optical chirality: design principles for chiral plasmonic nanostructures," *Phys. Rev. X*, 2, 031010 (2012).

[136] M. Schäferling, Yin, X., Engheta, N., Giessen, H., "Helical plasmonic nanostructures as prototypical chiral near-field sources," *ACS Photonics*, 1, 8 (2014).

[137] M. L. Nesterov, Yin, X., Schäferling, M., Giessen, H., Weiss, T., "The role of plasmon-generated near fields for enhanced circular dichroism spectroscopy," *ACS Photonics*, 3, 6 (2016).

[138] Y. Zhao, Askarpour, A. N.,Sun, L.,Shi, J.,Li, X., Alù, A., "Chirality detection of enantiomers using twisted optical metamaterials," *Nat. Commun.*, 8, 14180 (2017).

[139] L. Kang, Ren, Q., Werner, D. H., "Leveraging superchiral light for manipulation of optical chirality in the near-field of plasmonic metamaterials," *ACS Photonics*, 4, 8 (2017).

[140] F. Zhang, Xu, J., Lakhtakia, A., Pursel, S. M., Horn, M. W., Wang, A. , "Circularly polarized emission from colloidal nanocrystal quantum dots confined in microcavities formed by chiral mirrors " *Appl. Phys. Lett.*, 91, 023102 (2007).

[141] E. Plum, N. I. Zheludev, "Chiral mirrors," *Appl. Phys. Lett.*, 106, 221901 (2015).

[142] Z. Wang, Jia, H., Yao, K., Cai, W., Chen, H., Liu, Y., "Circular dichroism metamirrors with near-perfect extinction," *ACS Photonics*, 3, 6 (2016).

[143] C. Menzel, Helgert, C., Rockstuhl, C., Kley, E.-B., Tünnermann, A., Pertsch, T., Lederer. F., "Asymmetric transmission of linearly polarized light at optical metamaterials," *Phys. Rev. Lett.*, 104, 253902 (2010).

[144] Z. Liu, S. P. Rodrigues, W. Cai, "Simulating the Ising Model with a Deep Convolutional Generative Adversarial Network," *arXiv preprint arXiv:1710.04987*, (2017).

[145] E. Castiglioni, S. Abbate, F. Lebon, G. Longhi, "Chiroptical spectroscopic techniques based on fluorescence," *Methods Appl. Fluores.*, 2, (2014).

[146] P. Lodahl, S. Mahmoodian, S. Stobbe, A. Rauschenbeutel, P. Schneeweiss, J. Volz, H. Pichler, P. Zoller, "Chiral quantum optics," *Nature*, 541, 473-480 (2017).

[147] K. L. Seyler, J. R. Schaibley, P. Gong, P. Rivera, A. M. Jones, S. F. Wu, J. Q. Yan, D. G. Mandrus, W. Yao, X. D. Xu, "Electrical control of second-harmonic generation in a WSe2 monolayer transistor," *Nat. Nanotechnol.*, 10, 407-411 (2015).

[148] S. P. Rodrigues, W. Cai, "Nonlinear Optics: Tuning harmonics with excitons," *Nat. Nanotechnol.*, 10, 387-388 (2015).

[149] D. Wen, F. Yue, G. Li, G. Zheng, K. Chan, S. Chen, M. Chen, K. F. Li, P. W. H. Wong, K. W. Cheah, E. Y. B. Pun, S. Zhang, X. Chen, "Helicity

multiplexed broadband metasurface holograms," *Nat. Commun.*, 6, 8241 (2015).

[150] W. M. Ye, F. Zeuner, X. Li, B. Reineke, S. He, C. W. Qiu, J. Liu, Y. T. Wang, S. Zhang, T. Zentgraf, "Spin and wavelength multiplexed nonlinear metasurface holography," *Nat. Commun.*, 7, 11930 (2016).

[151] S. M. Kamali, E. Arbabi, A. Arbabi, Y. Horie, M. Faraji-Dana, A. Faraon, "Angle-multiplexed metasurfaces: encoding independent wavefronts in a single metasurface under different illumination angles," *Phys. Rev. X*, 7, 041056 (2017).

[152] O. Hess, J. B. Pendry, S. A. Maier, R. F. Oulton, J. M. Hamm, K. L. Tsakmakidis, "Active nanoplasmonic metamaterials," *Nat. Mater.*, 11, 573-584 (2012).

[153] A. A. Govyadinov, V. A. Podolskiy, M. A. Noginov, "Active metamaterials: Sign of refractive index and gain-assisted dispersion management," *Appl. Phys. Lett.*, 91, 191103 (2007).

[154] N. Zhang, W. Z. Sun, S. P. Rodrigues, K. Y. Wang, Z. Y. Gu, S. Wang, W. S. Cai, S. M. Xiao, Q. H. Song, "Highly reproducible organometallic halide perovskite microdevices based on top-down lithography," *Adv. Mater.*, 29, 1606205 (2017).

[155] M. Taghinejad, H. Taghinejad, Z. H. Xu, Y. W. Liu, S. P. Rodrigues, K. T. Lee, T. Q. Lian, A. Adibi, W. S. Cai, "Hot-electron-assisted femtosecond all-optical modulation in plasmonics," *Adv. Mater.*, 30, 1704915 (2018).

[156] R. W. Terhune, P. D. Maker, C. M. Savage, "Optical harmonic generation in calcite," *Phys. Rev. Lett.*, 8, 404-406 (1962).

[157] L. Kang, Y. Cui, S. Lan, S. P. Rodrigues, M. L. Brongersma, W. Cai, "Electrifying photonic metamaterials for tunable nonlinear optics," *Nat. Commun.*, 5, 4680 (2014).

[158] W. S. Cai, A. P. Vasudev, M. L. Brongersma, "Electrically controlled nonlinear generation of light with plasmonics," *Science*, 333, 1720-1723 (2011).

[159] S. Lan, L. Kang, D. T. Schoen, S. P. Rodrigues, Y. Cui, M. L. Brongersma, W. Cai, "Backward phase-matching for nonlinear optical generation in negative-index materials," *Nat. Mater.*, 14, 807-811 (2015).

[160] S. F. Lan, S. Rodrigues, Y. H. Ciu, L. Kang, W. S. Cai, "Electrically tunable harmonic generation of light from plasmonic structures in electrolytes," *Nano Lett.*, 16, 5074-5079 (2016).

[161] S. F. Lan, S. P. Rodrigues, M. Taghinejad, W. S. Cai, "Dark plasmonic modes in diatomic gratings for plasmoelectronics," *Laser Photonics Rev.*, 11, 1600312 (2017).

[162] A. Slobozhanyuk, S. H. Mousavi, X. Ni, D. Smirnova, Y. S. Kivshar, A. B. Khanikaev, "Three-dimensional all-dielectric photonic topological insulator," *Nat. Photonics*, 11, 130-136 (2017).

[163] S. Kruk, B. Hopkins, I. I. Kravchenko, A. Miroshnichenko, D. N. Neshev, Y. S. Kivshar, "Invited article: broadband highly efficient dielectric metadevices for polarization control," *Apl. Photonics*, 1, 030801 (2016).

[164] M. R. Shcherbakov, S. Liu, V. V. Zubyuk, A. Vaskin, P. P. Vabishchevich, G. Keeler, T. Pertsch, T. V. Dolgova, I. Staude, I. Brener, A. A. Fedyanin, "Ultrafast all-optical tuning of direct-gap semiconductor metasurfaces," *Nat. Commun.*, 8, 17 (2017).